Size Distribution Measurements of Wildfire Smoke-Influenced Aerosol at Yosemite National Park

by

Gavin R. McMeeking

Department of Atmospheric Science
Colorado State University
Fort Collins, Colorado

Fall 2004

Colorado State University

Department of Atmospheric Science

Paper No. 768

SIZE DISTRIBUTION MEASUREMENTS OF WILDFIRE SMOKE-INFLUENCED

AEROSOL AT YOSEMITE NATIONAL PARK

Submitted by

Gavin R. McMeeking

Department of Atmospheric Science

Colorado State University

Fort Collins, Colorado

Fall 2004

ABSTRACT

SIZE DISTRIBUTION MEASUREMENTS OF WILDFIRE SMOKE-INFLUENCED

AEROSOL AT YOSEMITE NATIONAL PARK

This work presents size distribution measurements made during the Yosemite

Aerosol Characterization Study (YACS) that took place from July to September 2002.

The main aim of the study was to determine chemical, optical and physical characteristics

of aerosol particles responsible for visibility degradation in Yosemite National Park. The

park, located in the central Sierra Nevada range in eastern California, was impacted by

smoke from wildfire activity in the western United States. Determining the contribution

made by smoke to visibility degradation is important in order to adequately understand

the impacts of anthropogenic emissions and regulate them accordingly to meet

Environmental Protection Agency requirements.

Measurements of dry aerosol size distributions were made with a differential

mobility analyzer (DMA) and an optical particle counter (OPC). The DMA sizes

spherical aerosol particles by their electrical mobility diameter, close to the true diameter,

while the OPC sizes particles by their optical diameter, a function of the particle

refractive index. An iterative alignment method assuming a range of refractive indices

was applied to OPC size distributions to match them to DMA size distributions, returning

the real refractive index that yielded the best fit. Best-fit OPC and DMA size distributions were then merged to give a complete size distribution for $0.038 < D_p < 2.1$ μm.

Concentrations of commonly used wood smoke tracers and backward trajectory analyses were used to determine periods of smoke influence at the park. Volume geometric mean diameters ranged from ~0.2 μm during non-smoke periods to ~0.4 μm during periods of highest fine aerosol mass concentrations associated with smoke-impacted times. $PM_{2.5}$ composition was determined to be dominated by organic carbon for most of the study period. Composition data and volume-weighted mixing rules were used to calculate aerosol refractive index, both real (1.570 ± 0.006) and imaginary (–$0.015i \pm 0.003i$) components, and bulk density (1.58 ± 0.09 g cm^{-3}). Calculated refractive index and densities were most sensitive to the values assumed for organic carbon refractive index and density, since this species dominated the composition.

The average retrieved refractive index was 1.577 ± 0.008, in relatively good agreement with calculated values. Imaginary (absorbing) components of the complex refractive index, calculated from aerosol composition, were within the range seen for aged biomass burning smoke in previous studies. Dry aerosol scattering coefficients, b_{sca}, were calculated from Mie theory using the retrieved refractive index and the calculated imaginary component for each 15-minute sample interval, at a wavelength of 530 nm and assuming homogeneous spherical particles. Scattering coefficients were roughly 50 Mm^{-1} on average, though values over 200 Mm^{-1} were calculated during the heaviest smoke-impacted times and agreed with measured values.

Dry mass scattering efficiencies were derived from calculated scattering coefficients and mass concentrations estimated from integrated volume distributions. For

an assumed dry particle density of 1.5 g m^{-3}, the calculated dry mass scattering efficiencies ranged from as low as 2.5 m^2 g^{-1} during the cleanest periods, to as high as 6 m^2 g^{-1}. On average, mass scattering efficiency was 4.3 ± 0.8 m^2 g^{-1}, near the nominal value used by the IMPROVE program for organic carbon.

Gavin Robert McMeeking
Atmospheric Science Department
Colorado State University
Fort Collins, CO 80523
Fall 2004

ACKNOWLEDGEMENTS

For Mom and Dad

TABLE OF CONTENTS

LIST OF TABLES

LIST OF FIGURES

CHAPTER 1. INTRODUCTION

This work presents findings from the 2002 Yosemite Aerosol Characterization Study (YACS) that was conducted from 15 July through 5 September 2002 in Yosemite National Park (YNP), California. The park is situated in the central Sierra Nevada range that runs north-south over much of eastern California. The chief goal of the study was to determine the influence of smoke from controlled burns and wildfires, both local and distant, on the physical, chemical and optical properties of aerosol sampled in the park. This work focuses on measurements of aerosol size distributions and their relationship to other observations of aerosol chemical composition and light scattering properties.

1.1 ORGANIC AEROSOL

A brief review of organic aerosol is provided as organic carbon dominated the fine aerosol mass (PM$_{2.5}$, particulate matter smaller than 2.5 μm aerodynamic diameter) during the study. Carbonaceous particles are emitted to the atmosphere by a large number of natural and anthropogenic sources. Sources that emit particles directly to the atmosphere are known as primary sources while sources that emit gas phase species that eventually convert to the aerosol phase are referred to as secondary sources. Carbonaceous particles are divided into two distinct chemical fractions. Elemental carbon (EC), often referred to as black carbon (BC), is emitted to the atmosphere directly by combustion. Major sources of EC in the United States are coal burning and diesel engines [*Seinfeld and Pandis*, 1998]. Global emissions of EC were estimated to be 12.6 to 24 Tg

1

(C) yr^{-1} and 0.4 to 1.1 Tg yr^{-1} for the United States [*Liousse et al.*, 1996; *Penner et al.*, 1993]. Organic carbon (OC) is a complex mixture of organic compounds and can be emitted directly to the atmosphere (primary OC) or formed *in situ* by the condensation of low-volatility products of the photooxidation of hydrocarbons (secondary OC). Wood fuel and coal burning and wildfires are the principal sources of primary OC in the United States, though plant leaves can contribute a significant amount of leaf wax as primary OC [*Seinfeld and Pandis*, 1998]. Secondary OC can be formed from hydrocarbons released from anthropogenic sources, such as gasoline powered vehicles, and natural sources, i.e. terpenes emitted by a number of tree species [*Griffin et al.*, 1999]. Global emissions of OC from biomass burning, fossil fuel and natural sources were estimated to total 81 Tg (C) yr^{-1} [*Liousse et al.*, 1996].

1.2 VISIBILITY

Visibility is affected by the scattering and absorption of light by atmospheric particles and gas molecules of natural and biogenic origin [*Seinfeld and Pandis*, 1998]. Scattering of light by atmospheric particles is the dominant factor affecting visibility in the United States. The amount of light a particle scatters is a function of the size of the particle, its index of refraction and the wavelength of the incident light. It is possible to theoretically determine total light scattering by atmospheric particles if these properties are known and if the particles are spherical and homogeneous. The functional dependence of scattering on these parameters is described by Mie theory, which shows that for atmospheric chemical species the most active scattering particles lie between 0.1 and 1.0 µm in diameter. A number of compounds commonly found in atmospheric

particles are highly hygroscopic, including acids and salts of sulfate (SO_4^{2-}) and nitrate (NO_3^-). If particles containing such compounds take up water, which can occur at relatively low humidity ($\sim$ 60% RH, lower for acidic species), their scattering properties are altered because of changes in their optical properties and size. Calculations of light scattering based on measurements of aerosol composition and mass must account for this hygroscopic growth in order to accurately determine overall light scattering coefficients.

In 2001 the United States Environmental Protection Agency (EPA) established a Regional Haze Rule (RHR) that mandates increasing emission controls to return national parks and wilderness areas to 'natural visibility conditions' by 2064. In a recent review Watson (2002) states that the RHR, "is possibly the most ambitious, most stringent, air quality goal ever promulgated." For the last 16 years the Interagency Monitoring of Protected Visual Environments (IMPROVE) program has made measurements of visibility-reducing particles to determine the major factors affecting visibility in national parks, wilderness areas and other regions. These measurements show that for the western U.S., home to a large number of national parks and wilderness areas, carbonaceous particles are the most abundant type of aerosol particle and are estimated to account for a significant fraction of the total light extinction [*Malm et al.*, 1994]. The sources of these particles are difficult to determine with sufficient confidence necessary for the formulation of emission control policies. This dilemma is caused by the large variety of organic chemical species present in atmospheric particles and the poor understanding of the optical properties of these particles in the atmosphere [*Watson*, 2002]. A considerable amount of analytical effort is necessary for detailed characterization of these particles' organic fractions. Even intense measurements of carbon-containing compounds typically

3

identify only 5-20% of the organic mass [*Rogge et al.*, 1993]. Considerable uncertainty is attached to values used to estimate scattering from measurements of organic carbon concentrations for this reason.

To meet EPA regulations, regional air quality administrators must be able to differentiate between manmade and natural visibility degradation that results from manmade and natural emissions of particles. The presence of both natural and anthropogenic sources of carbonaceous aerosol in the United States combined with the difficulty of easily distinguishing between the two with the measurement techniques employed by the IMPROVE program makes determining the 'natural visibility conditions' difficult, particularly in regions where carbonaceous particles are a significant fraction of the total aerosol. The EPA suggests default values for natural EC concentrations of 0.02 μg m^{-3} and 0.47 μg m^{-3} for natural OC in the western United States. *Park et al.* [2003] used an emissions inventory to model EC and OC concentrations at several IMPROVE measurement sites. A simulation with climatological monthly mean fire emissions and a best estimate of biogenic OC source was performed to estimate natural concentrations of carbonaceous aerosols in the United States. They estimated that natural EC and OC concentrations were 2-3 times higher than the recommended EPA default values for application to the Regional Haze Rule in most locations. This increase in background concentration translates to a decreased natural visibility on the order of 20% relative to EPA estimates [*Park et al.*, 2003]. It is not unreasonable to expect large fires to affect air quality in distant locations, making them regional—not local—sources of particles and trace gases. *Wotawa and Trainer* [2000] found that fires in western Canada influenced air quality in the southeast United States

during a field study in 1995. Other studies observed long range transport of fire smoke to the United States from Quebec and Central America [*Colarco et al.*, 2004; *Iziomon and Lohmann*, 2003]. Fire suppression policies during the 20th century have led to increased fuel loads in many forested regions and, when combined with drought in recent years, possibly an increase in severe fires. The influence of wildfires on air quality in the western United States is expected to remain high.

1.3 PREVIOUS STUDIES OF BIOMASS BURNING AEROSOL

Interest in the effect of biomass burning on atmospheric chemistry has increased since the pioneering papers on the subject in the 1970s and 1980s, significantly so since it was suggested that biomass burning emissions could rival those from fossil fuels during the 1980s [*Andreae and Merlet*, 2001]. The principal motivation for this work has been to understand the impact biomass burning aerosols have on climate change through direct radiative effects and indirectly through their impact on cloud properties [*Andreae and Crutzen*, 1997]. Previous studies of the properties of aerosol particles emitted through biomass burning have usually focused on tropical regions because approximately 80% of biomass burning emissions are in the tropics [*Hao and Liu*, 1994]. The Smoke, Clouds, and Radiation-Brazil (SCAR-B) field project emphasized measurements of surface biomass, fires, smoke aerosol and trace gases, clouds, and radiation, their climatic effects, and remote sensing from aircraft and satellites over the Amazon [*Kaufman et al.*, 1998]. The Southern Africa Regional Science Initiative (SAFARI) field campaign made similar measurements of biomass burning smoke aerosol and regional haze from savannah fires in Africa [*Haywood et al.*, 2003]. Numerous smaller field studies have also examined the

5

properties of particle emissions from tropical biomass burning in Asia as well as Africa and Central and Southern America [*Abel et al.*, 2003; *Ogunjobi et al.*, 2004; *Roberts et al.*, 2003]. The body of work on emissions by fires in non-tropical locations is somewhat smaller. *Conny and Slater* [2002] and *Hinzman et al.* [2003] examined fire emissions in the boreal region of Canada, while *Radke et al.* [1991] and *Martins et al.* [1996] investigated particle properties from biomass burning in the Pacific Northwest region of the United States. *Colarco et al.* [2004] and *Iziomon and Lohmann* [2003] examined properties of aged smoke plumes reaching different locations in the United States. In general, the studies listed above were primarily concerned with the climatic effects of the aerosol particles produced by the fires although estimates of optical properties needed for calculation of aerosol direct forcing are also relevant to visibility applications. Results from these previous studies are compared to YACS results in a later chapter. It should be noted that numerous studies have been conducted to determine properties of biomass combustion emissions for fuels commonly used in residential heating [*Fine et al.*, 2001; *Fine et al.*, 2002a; *Fine et al.*, 2002b; *Fine et al.*, 2004; *McDonald et al.*, 2000; *Rogge et al.*, 1998]. It is difficult to compare YACS results to the findings from these studies, however, due to the vastly different combustion conditions, chemical processing and age of the smoke produced by these laboratory studies.

Chapter 2 presents measurement techniques used during YACS to determine particle size distributions and composition during the study. Chapter 3 will provide an overview of the 2002 fire season in the western United States and detail methods used to determine smoke-impacted periods at YNP. Chapters 4 and 5 describe results from the physical sizing measurements and calculated light scattering properties of the aerosol.

Chapter 6 presents a discussion of the results and comparisons to previous studies while

Chapter 7 provides a summary and several future research topics.

CHAPTER 2. EXPERIMENTAL

Measurements of aerosol physical, chemical and optical properties were made at Turtleback Dome on the south rim of Yosemite Valley in Yosemite National Park (119.70 W; Lat 37.71 N; Elevation 1615 m). The park is located in California's central Sierra Nevada range, approximately 200 km east of San Francisco (Figure 2.1). The measurement campaign took place between 1 July 2002 and 5 September 2002. This chapter describes the physical sizing measurements made at Turtleback Dome in considerable detail and provides a brief description of additional measurements of aerosol chemical and optical properties that will be used for comparison purposes throughout this work.

2.1 AEROSOL INSTRUMENTATION

A large variety of instrumentation was used during YACS to measure chemical and optical properties of aerosol at the site. The instrumentation used for measurement of aerosol size distributions is described in the following section. A continuous carbon analyzer (Rupprecht and Pataschnick Series 5400, Albany, New York) measured total carbon (TC) using a thermal technique. A dual-wavelength aethalometer (Magee Scientific Aethalometer, Berkeley, California) measured black carbon (BC) using an optical absorption technique. BC is defined as the fraction of carbonaceous aerosol that absorbs light. These two instruments are described in greater detail in *McMeeking et al.* [in progress]. A Hygroscopic Tandem Differential Mobility Analyzer (H-TDMA) system

8

measured the hygroscopic properties of sampled aerosol particles during specific time periods of the study [*Carrico et al.,* submitted to *Atmospheric Environment*]. A Particle in Liquid System (PILS) operated in conjunction with an ion chromatography (IC) analytical system to obtain high-resolution (~ 15 minute) concentrations of water soluble Na^+, SO_4^{2-}, K^+, NH_4^+, Cl^- and NO_3^- [*Lee et al.,* in progress]. A Multiple Orifice Uniform Deposit Impactor (MOUDI) operated for 12-, 24- and 48-hour sampling periods at various times during the study to collect size differentiated particle samples for IC analysis. Particles were collected on different filter mediums for varying lengths of time to obtain $PM_{2.5}$ mass, chemical speciation and EC/OC concentrations [*Lee et al.,* 2004]. IMPROVE samplers also operated during the study according to the regular IMPROVE sampling protocol [*Malm et al.,* 1994]. Integrating nephelometers (Radiance Research, Seattle, Washington) operated during the study to obtain dry and ambient relative humidity $PM_{2.5}$ light scattering coefficients [*Day,* in progress].

2.2 AEROSOL SIZING INSTRUMENTATION

The primary measurement objective of the aerosol physical sizing instrumentation was determination of the optically active size spectrum, as this information is necessary to characterize light scattering. The physical sizing instrumentation was designed to measure the number size distribution from approximately 40 nm to 2 μm. Two different measurement techniques were utilized to cover this wide size range, which will be discussed in further detail below. The sampling setup used for aerosol physical sizing measurements was similar to the method used for the Big Bend Regional Observational Study (BRAVO) [*Hand et al.,* 2002] and is shown in Figure 2.2. An aerodynamic particle

sizer (APS) that measures particles in the size range 0.5 μm < D_p < 20 μm (D_p defined as particle diameter) operated during the study, but has not yet been included in this analysis.

The experimental setup was designed to maximize particle counting statistics by minimizing particle losses through the transport system. The sampling time of each instrument was selected to balance the need for reasonably high time resolution and improved counting statistics. In addition to the measurement of ambient aerosol, measurements of dried aerosol samples were also made to reduce uncertainties in particle sizing due to variations in the relative humidity (RH) of ambient and sample air. Drying of aerosol samples was achieved by passing the sample through a Perma Pure dryer (Perma Pure Inc., Toms River, NJ). Sensors were used to monitor sample line temperature and RH in several locations of the sampling system. The following sections will describe each instrument used to size particles as well as its associated sample transport and drying (if applicable) systems.

2.2.1 TSI 3081 DIFFERENTIAL MOBILITY ANALYZER (dry)

The TSI Differential Mobility Analyzer (DMA) (TSI, Minneapolis, MN) selects a range of known sizes of sub-micrometer aerosols using the theory of electrophoresis. The electrostatic force on a particle with n elementary charges, e, in an electric field E is given by equation (2.1)

$$F_e = neE \qquad (2.1)$$

In 1851 Stokes determined an expression for the drag exerted on a particle moving through a fluid for the case when inertial forces are negligible compared to viscous forces

(low Reynolds number). In his derivation, Stokes assumed spherical particles and no movement of fluid at the particle surface (or 'slip'). In practice, these conditions are rarely met by particles in the atmosphere and Stokes' law must be modified by two parameters: χ, the dynamic shape factor, which accounts for departures from sphericity, and the Cunningham Slip Correction factor (C_c) to account for fluid 'slip' at the particle surface for particles whose size approaches the mean free path of the gas. The dynamic shape factor is defined as the ratio of the actual drag force to the resistance force on a sphere having the same volume and velocity and is typically determined empirically. The slip correction factor is given by equation (2.2)

$$C_c = 1 + \frac{\lambda}{D_p}\left[2.514 + 0.8\exp\left(-0.55\left(\frac{D_p}{\lambda}\right)\right)\right] \quad (2.2)$$

where λ is the mean free path of the gas. The modified Stokes' drag force can be balanced with the electrostatic force to give the terminal velocity, v_t, of a particle moving through an electric field. Dividing this terminal velocity by the strength of the field yields the electrical mobility, Z_p, of the particle given by equation 2.3

$$Z_p = \frac{v_t}{E} = \frac{neC_c}{3\pi\eta\chi D_p} \quad (2.3)$$

where is the viscosity of the gas surrounding the particle. The DMA sizes particles based on this electrical mobility. A known charge distribution is applied to the sample particles by passing the particles through a Kr[85] neutralizer. There are numerous collisions between a high concentration of bipolar ions generated by the Kr[85] source and the aerosol particles due to the random motion of the ions. This causes the particles to quickly reach a state of equilibrium with the ions in which the particles carry a bipolar charge distribution. Charged aerosol is then passed through the annular region between two

11

concentric cylinders, with sheath air surrounding the inner cylinder. The outer cylinder is grounded, while a known negative voltage is applied to the inner collector rod. The potential difference between the negatively charged rod and the grounded outer cylinder results in positively charged particles being attracted towards the rod in the induced electric field. Particles having too high a mobility will impact on the inner collector rod while particles with too low a mobility are swept out of the instrument with the excess flow. Particles with some critical mobility enter a narrow slit at the bottom of the cylinders and are transported to a particle counter with the monodisperse flow. The particle counter used during YACS was a TSI 3010 Condensation Particle Counter (TSI Inc., Minneapolis, MN), described in further detail in Section 2.2.2.

The critical mobility depends on the applied voltage, V, and the instrument flow rates and geometry. *Knutson and Whitby* [1975] determined a relationship between instrument parameters and electrical mobility (Equation 2.4) and mobility bandwidth (Equation 2.5) as

$$Z_p = \frac{\left[Q_t - 0.5\left(Q_m + Q_p\right)\right]}{2\pi VL} \ln \frac{r_{out}}{r_{in}} \tag{2.4}$$

$$\Delta Z_p = \frac{\left(Q_m + Q_s\right)}{2\pi VL} \ln \frac{r_{out}}{r_{in}} \tag{2.5}$$

where Q_m, Q_p, Q_s, and Q_e are the monodisperse, polydisperse, sheath, and excess flows, respectively. Total aerosol flow (Q_t) is given by $Q_t = Q_p + Q_s$ or $Q_t = Q_m + Q_e$. The model used at Yosemite had an outer cylinder radius (r_{out}) of 1.958 cm and an inner cylinder radius (r_{in}) of 0.937 cm. The length, L, between the aerosol sample inlet and the exit slit was 44.44 cm (TSI DMA instrument manual). Combining Equations (2.3) and (2.4) gives the relationship between collector rod voltage and particle diameter.

$$V = \frac{3\chi D_{\mathrm{p}} Q_{\mathrm{s}} \ln(r_{\mathrm{out}}/r_{\mathrm{in}})}{2neC_{\mathrm{p}}L} \qquad (2.6)$$

The size distribution of the aerosol sample is determined by inverting the measured mobility distribution. The mobility channels were forced to meet at the channel mobility limits to simplify this inversion for a selected sheath to sample flow ratio of 10:1. This corresponds to mobility increments of $Z_{p,i+1} = 1.222 \, Z_{p,i}$. To ensure this, the instrument volumetric flow rates were carefully monitored and maintained at $Q_{sheath} = 3.0$ LPM and $Q_{sample} = 0.3$ LPM through daily checks by the instrument operator. Variations in these flows were observed to be on the order of 3%. This study measured particle concentrations in 25 bins with a diameter range of $0.038 < D_{\mathrm{p}} < 0.85$ μm. The sample time for each channel increased with size, the largest diameters sampling longer to improve Poisson counting statistics [*Hand*, 2001].

A complication in the measurement occurs due to large particles with multiple charges that have the same mobility as smaller particles of unit charge. Small particles typically have only one charge, while larger particles (>70 nm) can have more than one charge because their larger size gives ions more surface area with which to interact. The mobility to diameter inversion process must account for these multiply charged particles in order to obtain an accurate size distribution as otherwise the instrument will misidentify the larger multiply charged particles as smaller singly-charged particles. Table 2.1 lists charging efficiencies calculated using the methods of *Wiedensohler* [1988] and *Fuchs* [1964]. Fuchs' model was used to compute the fraction of particles with three or more charges, while Wiedensohler's least-squares regression analysis was applied for particles with one and two charges. To close the set of equations, the inversion method requires a known cutoff point for the largest sized particle that can enter the DMA and

13

thus the largest multiply-charged particles that must be corrected for. The TSI instrument manual suggests that an impactor be used for this purpose. However, in this work, as in earlier studies, a correction for multiply charged particles was made by incorporating measurements from an optical particle counter (OPC) of larger sized particles into the DMA inversion routine [*Hand and Kreidenweis*, 2002]. Three artificial mobility channels were created for the DMA, corresponding to particle diameters larger than the maximum diameter physically sampled by the instrument. Table 2.1 gives charging efficiencies for 25 DMA channels and three artificial mobility channels for as many as six charges.

The DMA inversion can be described by the following equations. Raw DMA concentrations, c, are related to the corrected concentrations, N, by matrix $\mathbf{A}$ (Equation 2.7). The probability that an aerosol particle that enters the DMA through the inlet with mobility Z_p will leave through the instrument with the monodisperse flow is given by the transfer function and is governed by behavior of the flow inside the DMA cylinder. The transfer function was approximately triangular for the flow configuration used in the DMA, with a peak probability value occurring at the desired Z_p. The raw data were corrected for the approximately triangular DMA transfer function by multiplying the concentrations by a factor of two as half of the particles lying within a given DMA channel would not exit the instrument.

$$c = \mathbf{A}N \qquad (2.7)$$

In order to obtain the corrected concentration, the matrix $\mathbf{A}$ was inverted, giving Equation 2.8.

$$N = \mathbf{A}^{-1}c \qquad (2.8)$$

14

A included terms for multiply-charged particle corrections for both the original DMA channels and the three artificial channels containing the incorporated OPC data. **A** also included loss corrections as calculated in Appendix A. Losses in the DMA were on the order of 10 to 15%, with largest values near the instrument size limits. Combining charge corrections, **f**, and loss corrections, η, gives:

$$\mathbf{A} = \mathbf{f}\eta \tag{2.9}$$

2.2.2 TSI 3010 CONDENSATION PARTICLE COUNTER

A TSI 3010 condensation particle counter (CPC) was used to determine particle concentrations of the monodisperse aerosol passing out of the DMA. The CPC detects particles optically after they have grown through condensation in a region that is highly supersaturated with respect to the working fluid. The CPC operating at Yosemite used 1-butanol (Fisher Scientific Co., Houston, Texas) as the working fluid. All particles larger than ~ 0.01 µm undergo rapid growth upon entering the condensing chamber, allowing them to be easily detected by light scattering. The CPC required a sample flow rate of 1.0 LPM, so 0.7 LPM of filtered, dry dilution air was introduced to the 0.3 LPM DMA monodisperse flow.

2.2.3 PMS LASAIR 1002 OPTICAL PARTICLE COUNTER

Dry and ambient aerosol size distributions were measured with Particle Measuring Systems (PMS, Boulder, CO) optical particle counters (OPC). The LASAIR 1002 sampled dry aerosol size distributions with a 0.057 LPM flow rate giving a maximum detectable concentration of ~ 880 particles cm^{-3}. The LASAIR 1003 sampled

ambient aerosol size distributions with a 0.028 LPM flow rate giving a maximum detectable concentration of ~ 6800 particles cm^{-3}. The instruments size particles into eight size bins with manufacturer calibration lower bin limit diameters corresponding to 0.1, 0.2, 0.3, 0.4, 0.5, 0.7, 1.0, and 2.0 μm (PMS LASAIR 1002/1003 instrument manuals). An OPC sizes an aerosol particle based on the intensity of the light (λ = 632.8 nm) that is scattered by the particle at some known wavelength. The intensity of scattered light depends on particle size, shape and index of refraction, the last determined by the particle composition. The manufacturer calibrations were performed with polystyrene latex spheres (PSL, Duke Scientific, Palo Alto, California) with refractive index 1.588 (λ = 589 nm). Additional calibrations were performed for the LASAIR 1002 in the laboratory to determine the instrument response to particles with varying indices of refraction. The laser voltage of the instrument was recorded to determine cleanliness of the optics. During the study the voltage remained well above the manufacturer recommended limit of 4.5 volts for over 99% of the measurement sample intervals. A low sample flow rate is used to ensure that only one particle is present in the laser beam at any one time. This assumption is no longer valid for very high aerosol concentrations. The maximum concentration limit of the LASAIR 1003 was never observed during the study.

Both LASAIR instruments maintain flow rates by means of a mass flow meter inside the instrument that monitors the pressure drop across a venturi and displays volumetric flow on the instrument front panel. Ideally flow rates would be measured at least weekly with a Gilibrator low flow cell (Gilian, Clearwater, Florida) to check the accuracy of the instrument flow rate value. Unfortunately the low flow cell was

unavailable for most of the study, so frequent flow checks were only performed during the final days of August and September. An unusual phenomenon was observed during the study in which the measured flow rate of the LASAIR 1002 was lower than the set value by as much as 50 % for prolonged periods during most days. The diurnal signature evident most likely indicates some kind of temperature effect on the instrument. Though the LASAIR 1003 did not sample dried aerosol particles, it is likely that total number concentration measured by each instrument did not differ significantly given the very low instrument humidity (< 25%) and low particle hygroscopicity observed during the study [*Carrico et al.*, submitted]. Due to the strange behavior of the LASAIR 1002 measured flow rates, those data were not used and LASAIR 1003 measurements were assumed to be valid for dry particles. Unfortunately the instrument optics had been cleaned following YACS, so post-field calibrations were not able to be performed. *Hand and Kreidenweis* [2002] determined responses for the instrument during BRAVO through calibration with particles of known size and refractive index. These values were assumed valid for YACS and did not differ substantially from values determined as part of this work for the LASAIR 1002.

2.3 AEROSOL SAMPLING AND TRANSPORT

The sizing instruments were housed in an air-conditioned trailer located in a clearing near the top of Turtleback Dome. The sizing instrument sampling setup is diagrammed in Figure 2.2. All sizing instruments sampled aerosol particles from a common inlet located on the roof of the trailer. The inlet was sheltered by a rain hat to prevent excessive moisture entering the instrument sampling chambers. Sample air

17

entering the inlet passed through 40 inches of 0.5 inch outer diameter (OD) (0.402 inch inner diameter) stainless steel (SS) pipe before entering a five-way flow splitter located directly below the trailer ceiling. The sampling line between the trailer roof and the flow splitter was wrapped in insulating tape to maintain the aerosol sample flow close to its ambient temperature. The five-way flow splitter consisted of a 14-inch long, 3-inch diameter steel pipe with four 0.25 inch OD (0.194 inch ID) SS and one 0.5 inch OD (0.402 inch ID) SS tubes extending from the lower end of the pipe. The total flow rate through the sampling system before splitting of flows was approximately 6 LPM, though this flow was increased by approximately 0.9 LPM with the addition of another sampler on 10 August.

Aerosols sampled by the DMA/OPC drying system passed through 8 inches of 0.25 inch OD (0.194 inch ID) SS tubing at a flow rate of approximately 0.35 LPM before entering a 24-inch long SS Perma Pure dryer. After exiting the dryer, the aerosol sample flow passed through three inches of 0.25 inch OD (0.194 inch ID) SS tubing before reaching a Y-shaped flow splitter with 20 degree bends from the vertical. Sample was passed to the LASAIR 1002 through 8 inches of flexible 0.375-inch OD (0.19-inch ID) carbon impregnated tubing (Compound 1851, Vanguard Products, Danbury, CT) from one branch of the "Y" at a flow rate of approximately 0.05 LPM. The remaining 0.3 LPM of sample flow passed through 17 inches of carbon impregnated tubing to the sampling port of the DMA. Approximately 0.03 LPM of sample flow was drawn from another port of the five-way flow splitter through 16 inches carbon impregnated tubing before reaching the sampling port of the LASAIR 1003. Measurements were corrected for losses in the sampling and transport system and are described in detail in Appendix A.

Table 2.1 Charging efficiencies of aerosol particles of geometric size, D_p, determined using the methods of *Fuchs* [1964] and *Wiedensohler* [1988].

DMA channel	D_p (nm)	Charging efficiency (# of charges)					
		1	2	3	4	5	6
1[*]	1430.0	0.0839	0.0652	0.0469	0.0312	0.0192	0.0109
2[*]	1198.0	0.0926	0.0704	0.0488	0.0308	0.0177	0.0092
3[*]	1007.0	0.1017	0.0753	0.0499	0.0296	0.0157	0.0074
4	850.2	0.1098	0.0778	0.0501	0.0276	0.0134	0.0057
5	720.3	0.1177	0.0814	0.0494	0.0251	0.0109	0.0041
6	612.7	0.1269	0.0851	0.0478	0.0220	0.0085	0.0027
7	523.4	0.1372	0.0883	0.0453	0.0187	0.0063	0.0017
8	449.2	0.1480	0.0904	0.0419	0.0153	0.0044	0.0010
9	387.2	0.1591	0.0910	0.0379	0.0120	0.0029	0.0005
10	335.3	0.1700	0.0899	0.0334	0.0091	0.0018	0.0002
11	291.6	0.1804	0.0871	0.0287	0.0065	0.0010	0.0001
12	254.6	0.1899	0.0828	0.0240	0.0045	0.0005	0.0
13	223.2	0.1982	0.0773	0.0194	0.0029	0.0003	0.0
14	196.3	0.2052	0.0709	0.0152	0.0018	0.0001	0.0
15	173.3	0.2106	0.0639	0.0115	0.0011	0.0001	0.0
16	153.3	0.2144	0.0566	0.0084	0.0006	0.0	0.0
17	136.0	0.2165	0.0494	0.0059	0.0003	0.0	0.0
18	121.0	0.2169	0.0424	0.0039	0.0001	0.0	0.0
19	107.8	0.2155	0.0358	0.0025	0.0001	0.0	0.0
20	96.2	0.2126	0.0297	0.0015	0.0	0.0	0.0
21	86.0	0.2082	0.0242	0.0009	0.0	0.0	0.0
22	77.0	0.2025	0.0194	0.0005	0.0	0.0	0.0
23	69.0	0.1956	0.0153	0.0002	0.0	0.0	0.0
24	61.9	0.1877	0.0118	0.0001	0.0	0.0	0.0
25	55.6	0.1789	0.0089	0.0	0.0	0.0	0.0
26	50.0	0.1695	0.0065	0.0	0.0	0.0	0.0
27	45.0	0.1597	0.0047	0.0	0.0	0.0	0.0
28	40.5	0.1496	0.0033	0.0	0.0	0.0	0.0

[*]Artificial bins containing OPC data for multiple charge correction purposes

Figure 2.1 Map showing location of Yosemite National Park and location of the study site (Turtleback Dome) within the park (inset).
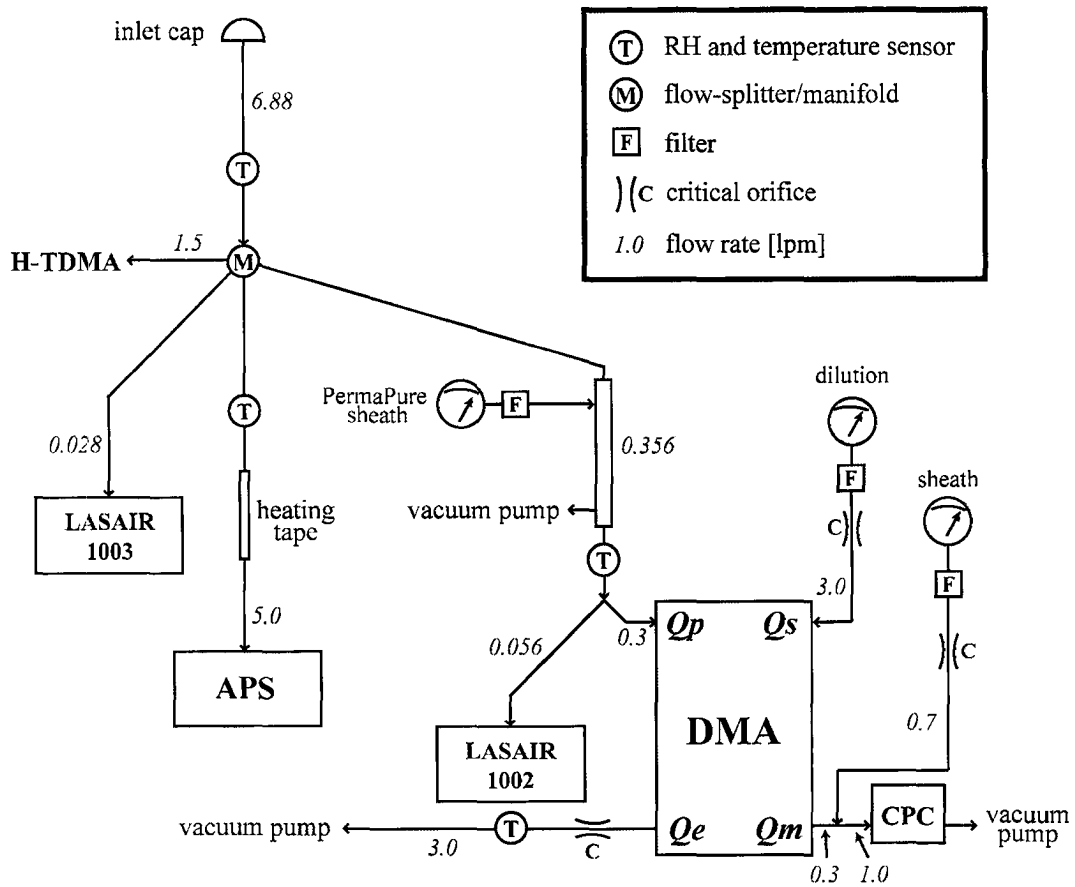
Figure 2.2 Experimental set-up of the aerosol sizing system.

CHAPTER 3. IDENTIFICATION OF SMOKE IMPACTED PERIODS

Measurements of aerosol chemical composition and size distributions, meteorological variables, and fire location and intensity were used to determine smoke-impacted periods at YNP. This chapter presents the methods and data used to determine these periods and an overview of the 2002 fire season, as described in further detail in *McMeeking et al.* [in progress].

3.1 THE 2002 FIRE SEASON

The National Interagency Fire Center (NIFC) reports fire statistics based on end-of-year reports compiled by all wildland fire agencies, which include the Bureau of Land Management, Bureau of Indian Affairs, National Park Service, United States Fish and Wildlife Service, USDA Forest Service and all state lands. NIFC reports that over 88,400 fires burned over 6.9 million acres in 2002 in the contiguous United States, compared to the 10-year average of just over 4.2 million acres. The severity of the 2002 fire season was driven primarily by extreme drought conditions throughout most of the United States, with 45 percent of the country reporting moderate to extreme drought conditions early in the season. Colorado, Arizona and Oregon recorded their largest fires in the last century [*National Interagency Fire Center*, Boise, Idaho].

Two very large fires were believed to have had the strongest impact on the site. The Biscuit Fire, located approximately 700 km north northwest of YNP, burned over 500,000 acres between 15 July and 5 September. The McNally Fire, located

approximately 150 km south of YNP, burned roughly 150,000 acres from 23 July to 28 August. In addition to these two large fires, numerous smaller fires with sizes greater than 500 acres burned throughout Oregon and California for shorter durations during the study. The National Interagency Fire Center (NIFC) does not report fires smaller than 500 acres in size. The National Park Service (NPS) provided times and locations of small local fires inside YNP. Figure 3.1 shows the locations of the large (>500 acre) fires for Oregon, Washington, and California and the locations and names of small fires within YNP (inset). Much of the fire activity during the summer occurred in the Pacific Northwest, with a large number of fires in southwestern Oregon. Limited fire activity occurred in Nevada during the study period. Several large fires occurred in western Nevada, but were contained before the July 20 (DOY 201) starting date of the analyses presented in this work. Only one wildfire larger than 1000 acres in size occurred after July 20 and was located within 50 miles of the Nevada-Utah border, a region where transport to YNP did not occur.

3.2 METEOROLOGY

Relationships between observations of aerosol and meteorological conditions are complicated by the study site location in complex mountain terrain. Large scale upper level wind patterns control the long-range transport of smoke from fire sources. Examination of upper-air charts shows the presence of an upper level high over the western United States for the most of the study. This resulted in relatively weak upper level winds over the region. Infrequent passage of weak upper level troughs caused increased northerly flow over northern California. Surface measurements of

23

meteorological variables show a very strong influence of a thermally driven mountain-valley wind system in addition to longer-term synoptic effects. In order to determine if emissions from wildfires reached the site it is necessary to account for both effects. This section describes surface measurements of meteorological variables and results of modeled back trajectory calculations that attempt to determine source regions for air masses sampled at Turtleback Dome.

3.2.1 SURFACE MEASUREMENTS

Surface measurements of temperature, relative humidity, wind speed and direction, solar insolation and barometric pressure were made at the study site for the duration of the study. Weather conditions at the Turtleback Dome site were sunny, dry and warm for the majority of the study period. Diurnal surface wind direction patterns were extremely regular during the study due to the presence of a thermally driven valley wind pattern [*Whiteman*, 2000]. Varying wind speed observed at the study site, averaged over all study days, is shown in Figure 3.2. Maximum hourly average wind speed peaked at approximately 12 m s^{-1} and typically occurred in the mid-afternoon. Lowest average wind speed was usually seen at 0800 PST and 2100 PST during transitions between up-valley and down-valley flow regimes. Figure 3.3 gives average wind direction over all study days with one standard deviation. Winds blew up the valley from the west (~ 250 degrees) from approximately 0900 PST to approximately 1900 PST and blew down the valley from the east (~ 60 degrees) during the night. The morning shift typically occurred between 0700 and 1000 PST, and was usually short, as indicated by the low variability in

wind direction before and after the transition. The evening shift was less abrupt with the transition occurring between 1600 and 2200 PST.

3.2.2 MODELED BACK TRAJECTORIES

In order to determine major sources and pathways of the air masses reaching YNP, an air mass backward trajectory analysis was performed. The National Oceanographic and Atmospheric Administration (NOAA) Hybrid Single-Particle Lagrangian Integrated Trajectory (HYSPLIT v 4.7) model [*Draxler*, 2003] was used to determine backward trajectories for each hourly arrival time at several receptor sites for each day of the study. Five-day (120 hr) backward trajectories were calculated for heights of 10, 100, 500, and 1000 m above ground level (AGL). In addition to the YNP receptor site (119.703 W; Lat 37.713 N; elevation 1615 m), calculations were also made for a San Joaquin Valley location (120.363 W; Lat 37.056 N; elevation 190 m) to determine if there were major differences in the source regions for the two locations. This determination was necessary because the mountain-valley wind system caused daily transport of San Joaquin Valley air to the park. The model was also used to determine forward trajectories from known fire locations at specific times for comparison with backward trajectory results. HYSPLIT uses gridded meteorological data computed by an external model. The Final (FNL) data product of the Global Data Assimilation System (GDAS) was used for the YACS backward trajectory analysis. The gridded data used the global spectral Medium Range Forecast model (MRF) to assimilate multiple sources of measured data and forecast meteorology. FNL data were on a 129 x 129 Polar

Stereographic grid with 120 km resolution and contained 12 vertical layers on constant pressure surfaces from 1000 to 50 hPa [*National Center for Environmental Prediction*].

Backward trajectories returned by HYSPLIT are shown for 12 PST for 13 August 2002 in Figure 3.4 for four different arrival heights to provide an example of the HYSPLIT output. The locations of wildfires that grew larger than 500 acres during the study period are also plotted for California, Oregon and Washington. The backward trajectories for this time all pass over the state of Oregon. Examination of backward trajectories for other times revealed two main paths for transport during the study. The first path originated off the coast of British Columbia, ran south over the coasts of Washington, Oregon and northern California before heading east over the San Francisco Bay Area and the San Joaquin Valley to the site. The other traveled through central Oregon and northwestern Nevada before reaching the park from the east. Additional modeled transport pathways originated from the south of YNP and to the west, though this occurred infrequently. In general, most transport pathways traveled over Oregon or very close to the Oregon coastline before reaching the study site.

3.3 DETERMINATION OF RESIDENCE TIME

While it is possible to easily interpret a small number of trajectories graphically by plotting individual trajectories on a map, examination of common transport patterns over long time periods is made easier through the use of statistical methods. *Gebhart et al.* [2001] determined how often air masses from the United States and Mexico arrived at Big Bend National Park by counting the number of trajectory endpoints in each country for a specified observation period. This method was used previously for air masses

arriving at Grand Canyon National Park from four different quadrants [*White et al.*, 1994]. *Ashbaugh et al.* [1985] developed a statistical method, residence time probability analysis, for interpreting backward trajectories to determine source regions for sulfate aerosol at Grand Canyon National Park. This method quantifies the relative impacts of source regions on the receptor site by determining the spatial probability distribution of the previous positions of air parcels (at some time interval) that arrived at the receptor over a specified time period (5 days during YACS). If n_{ij} is the number of trajectory endpoints (i.e. the positions of the air parcels at each time increment) that fell in the ijth cell of a domain surrounding the receptor site during the time interval T, and N is the total number of endpoints computed for the time interval, then the probability can be defined as

$$P[A_{ij}] = \frac{n_{ij}}{N} \tag{3.1}$$

The probability $P[A_{ij}]$ represents the residence time of a randomly selected air parcel in the ijth cell relative to the total time interval T [*Ashbaugh et al.*, 1985]. A hypothetical probability density function, $P[H_{ij}]$, can be constructed to compare with $P[A_{ij}]$ to determine whether the actual residence time is greater or less than what could be expected from a hypothetical distribution of trajectories [*Ashbaugh et al.*, 1985]. For a hypothetical distribution which assumes air parcels can arrive at the receptor from any direction with equal probability with a constant wind speed, v, it can be shown that

$$P[H_{ij}] = \frac{a_{ij}}{\pi R^2} \frac{R}{2r} \tag{3.2}$$

where a_{ij} is the area of the ijth cell, r is the mean distance between the cell and the receptor, and R is the radius of the spatial extent of all trajectories, given by $R = vT$. This

results in a distribution with a peak at the center, where all trajectories converge, and that decreases with the inverse of the distance of the cell from the receptor [*Ashbaugh et al.*, 1985]. Assuming v is 6 m s^{-1} (based on the average wind speed at 950 mb during the study period in the domain area) gives R as approximately 2600 km. A source contribution function can be defined as

$$S[A_{ij}] = \frac{P[A_{ij}]}{P[H_{ij}]} \tag{3.3}$$

If the source contribution function is greater than one, then the residence time for that cell is greater than would be expected from the chance hypothetical distribution. It can be shown that the source contribution function is proportional to the residence time multiplied by the distance from the grid cell center to the receptor [*Gebhart et al.*, 2001].

Source contribution functions were calculated for the entire study period (0000 PST, 20 July 2002 through 1200 PST 5 September) and to examine variability in major meteorological patterns. The grid domain used for the calculations was the box bounded by latitudes of 24 N and 74 N and the 170 W and 110 W meridians. Residence times were determined for 0.5 x 0.5 degree cells from the 500 m arrival height backward trajectories. Trajectories which hit the ground were removed from the analysis and accounted for approximately 20% of the total number of trajectories. Contours of the source contribution function for the entire study period are plotted in Figure 3.5. The majority of backward trajectories modeled during the study originated to the northwest of the study site, indicating this area was the dominant source region for air masses arriving at YNP during the study. Maximum values of the source contribution found in the region were on the magnitude of 25, indicating that the probability of an air parcel arriving at Yosemite National Park during the study residing in this region was 25 times that

expected for the hypothetical distribution. It should be noted that the magnitude of the source contribution function is sensitive the choice of v, which determines the radius of the hypothetical probability density distribution. An increase in the value assumed for v results in an increase in $S[A_{ij}]$.

3.4 TRACERS FOR WOODSMOKE

In addition to meteorological analyses, a number of wood smoke tracers were used to identify smoke-impacted periods at YNP. *McMeeking et al.* [in progress] provide detailed descriptions of measurements used to identify smoke in aerosol measurements. Water-soluble potassium ion (K^+) has been used as a wood smoke tracer in numerous studies in urban and remote locations. Observed concentrations of K^+ are presented in Figure 3.6. Measurements of K^+ were made with the Particle-in-Liquid Ion Chromatography (PILS-IC) system described in Chapter 2 and are given as hourly averages. Elevated K^+ concentrations can be seen between DOY 208 (27 July) and DOY 214 (2 August). Backward trajectory analysis for this time indicated a dominant transport pathway that passed over central Oregon and south over western Nevada and northeastern California before reaching the site. A second, longer period of elevated concentrations of K^+ occurred between DOY 221 (9 August) and DOY 234 (22 August) and contained one short period with lower concentrations near DOY 231 (19 August). Backward trajectory analysis indicated that the dominant transport pathway during this time consisted traveled down the coast of Oregon, over southwestern Oregon, the coast of California and through the San Francisco Bay Area before reaching the site. A shorter three-day period of elevated K^+ occurred between the two major events, DOY 216 – DOY 219 (4 August – 7

August). Transport during this time was similar to the transport seen during the second major event. Shorter-duration, high K^+ concentration events can also be seen on several other occasions during the study.

Another commonly-used wood tracer is levoglucosan, which is a stable combustion product of cellulose thought to be stable against degradation in the atmosphere [*Simoneit et al.*, 1999]. Levoglucosan concentrations were obtained by the analytically intensive method of derivatization followed by gas chromatography-mass spectrometry (GC-MS) and were only made for weekly filter samples and several individual daily filter samples. As these analyses are still underway, results are not included in this work, but will be included in future work.

Wood smoke has been found to absorb light preferentially for wavelengths in the ultra-violet (UV) due to the presence of aromatics [*Magee Scientific website*]. Absorption of UV light is quantified as a UV particulate matter (UVPM) concentration. Differences between the UVPM and BC concentrations measured with an aethalometer, normalized by BC concentration, are shown in Figure 3.7. Immediately apparent are the short, high events of large UV/BC difference during the beginning and end of the study. These are most likely associated with transport down the valley from local fires burning within the park. The periods of elevated K^+ concentrations identified earlier also correspond with increases in the UV/BC difference signal, though the first event shows less of an effect than the second. The shorter three-day event described above can also be seen in the signal.

A robust criterion for the classification of certain time periods of the study being 'smoke-influenced' is not provided. Instead, times thought to be smoke-influenced were

determined through the use of smoke tracer results described above, meteorology, and information about fire timing and location. Table 3.1 gives the proposed start and end times/dates for smoke-influenced periods at YNP and the primary reason for identification. The influenced periods are separated into long-term regional hazes and shorter-term events that include impacts from local fires. These classifications are used in the analysis of aerosol sizing data in the chapters that follow. They are by no means a definitive listing of all smoke-influenced air masses at YNP as other brief smoke-influenced periods are almost certainly present.

All indicators pointed to a considerably smoke-influenced event occurring between DOY 220 and DOY 235 (8 August – 26 August), though other events are less certain. The combination of transport from distant fires and influence from local fires is complicated by fire activity, fire locations, transport mechanisms, and local terrain influence on transport at the site itself. A more involved modeling study of the region would provide more robust estimates of smoke influence timing and sources, but the above analysis does show with reasonable certainty that much of the study period was affected by smoke emissions to some extent.

Table 3.1 Periods of smoke-influence at Yosemite National Park based on several smoke tracer concentrations and meteorological signatures.

Start Date	End Date	Classification	Justification
0500 PST 22 July	0800 PST 22 July	Local	A, SM
0900 PST 23 July	1000 PST 23 July	Local	A, SM
0100 PST 25 July	0900 PST 25 July	Local	A, SM
0000 PST 26 July	0900 PST 26 July	Local	A, SM
0000 PST 27 July	0000 PST 5 August	Regional	K, BTA
1700 PST 5 August	0400 PST 6 August	Local	A, SM
1200 PST 8 August	0900 PST 23 August	Regional	A, K, BTA
2200 PST 26 August	1200 PST 27 August	Local	A, K, SM, HO
2300 PST 1 September	1000 PST 2 September	Local	A, SM
2300 PST 2 September	0800 PST 3 September	Local	A, SM

A: aethalometer (UV – BC)
K: water soluble potassium
SM: surface wind measurements
BTA: back trajectory analysis
HO: human observation (strong smell of smoke)
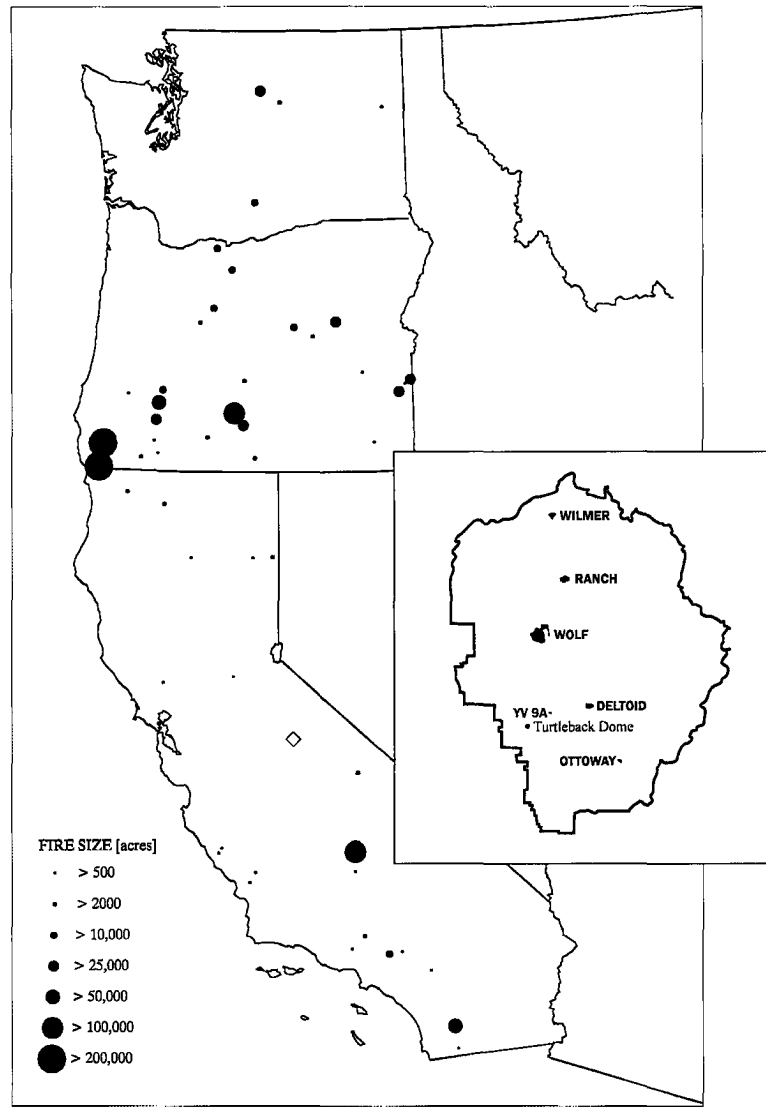
Figure 3.1 Locations of fires (>500 acres) during the study in Washington, Oregon and California and locations and names of selected fires within Yosemite National Park (inset). The two large fires in southwestern Oregon represent a series of major fires that, after merging together, were referred to as the Biscuit and Tiller fires and are simply referred to as the Biscuit fire in this work.

33
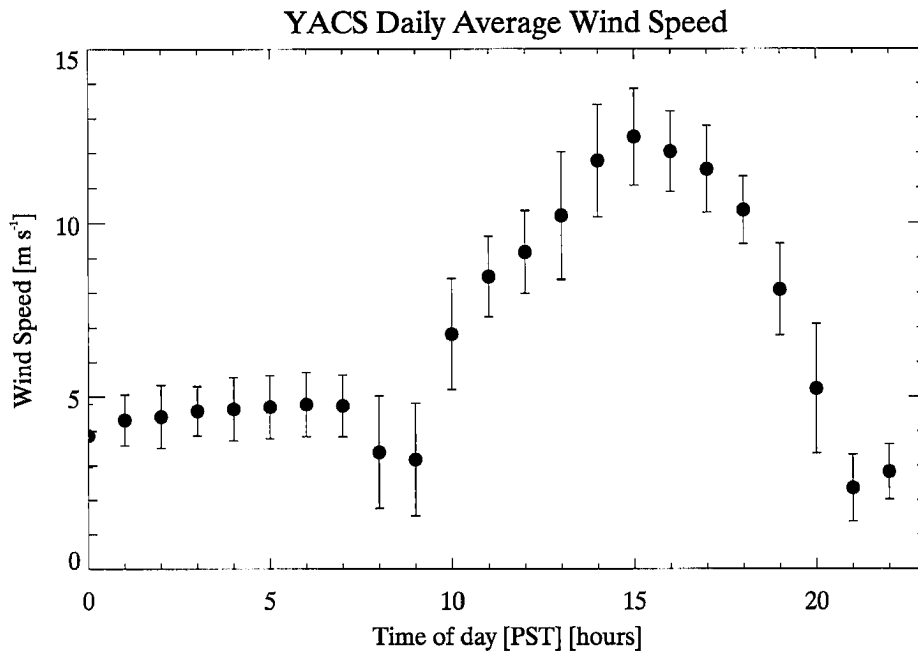
Figure 3.2 Daily averaged wind speed at Turtleback Dome during YACS. Error bars represent one standard deviation.
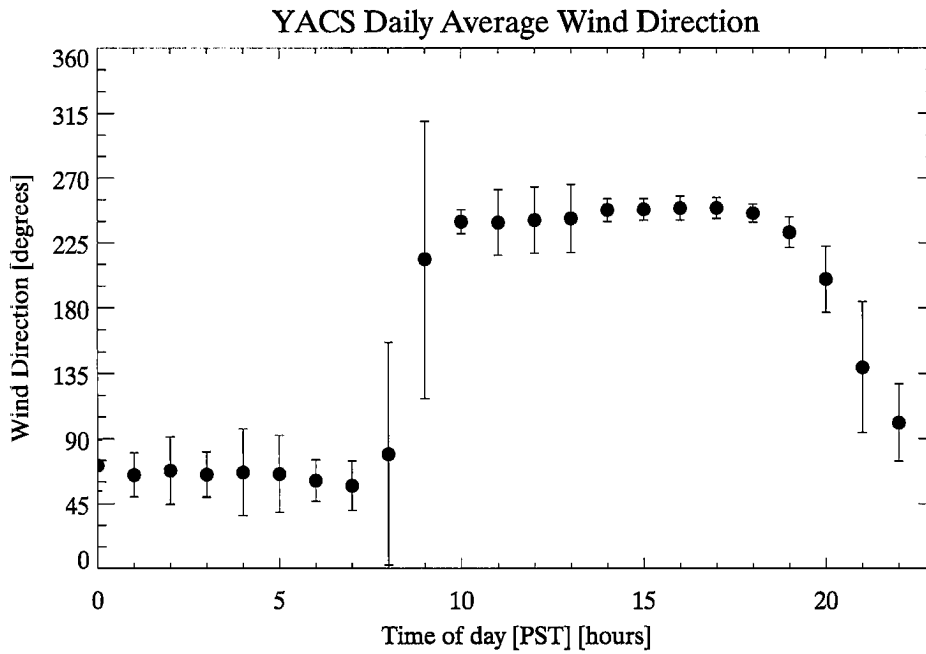
Figure 3.3 Daily averaged wind direction at Turtleback Dome during YACS. Error bars represent one standard deviation.
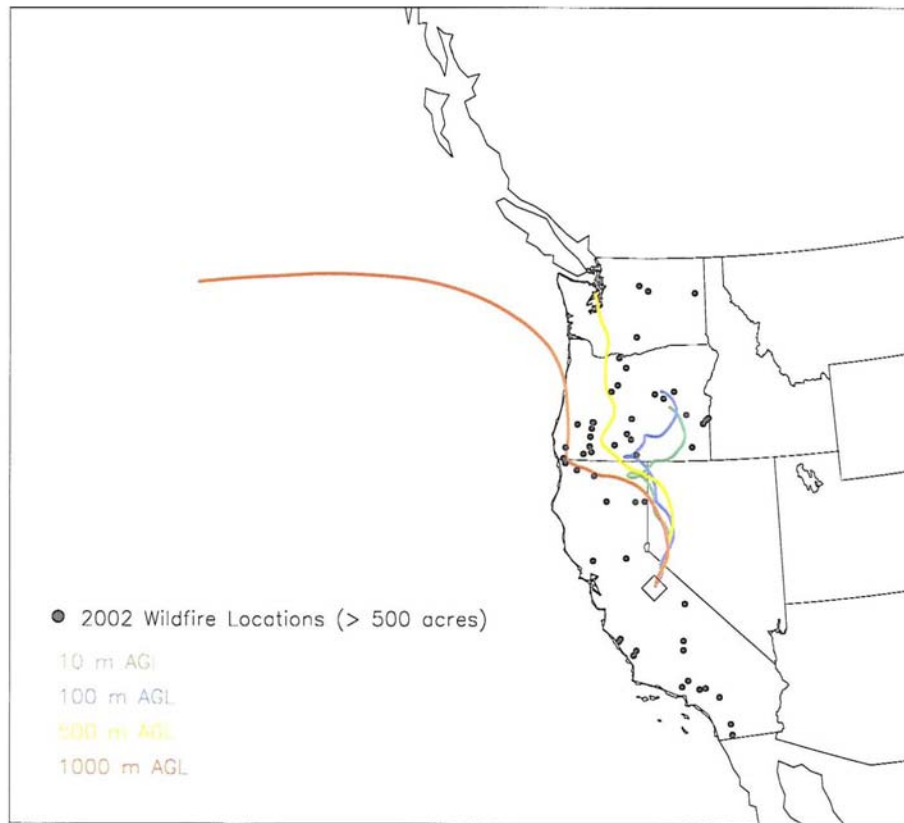
Figure 3.4 Plots of back trajectories modeled using HYSPLIT for 1200 PST 13 August 2002 for four different heights above ground level. Locations of fires that reached a size greater than 500 acres during the study are plotted with filled black circles. The study site location is indicated by the hollow diamond.
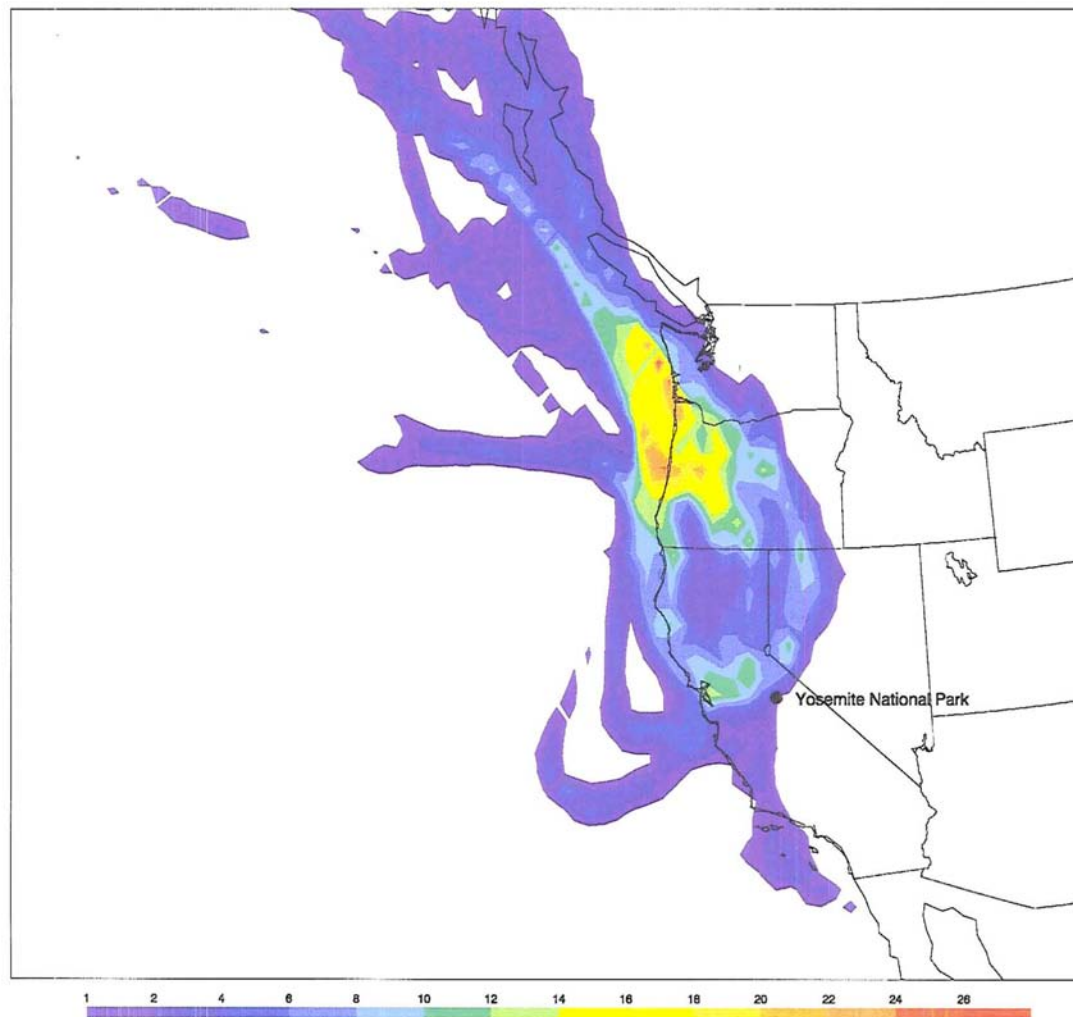
Figure 3.5 Contour plot of the source contribution function for all trajectories arriving at Turtleback Dome during the period 20 July 2002 thru 5 September 2002. Arrival height was 500 m above ground level. Hotter colors indicate a higher probability that the air parcel arriving at the site during this time was in that area prior to reaching the park.
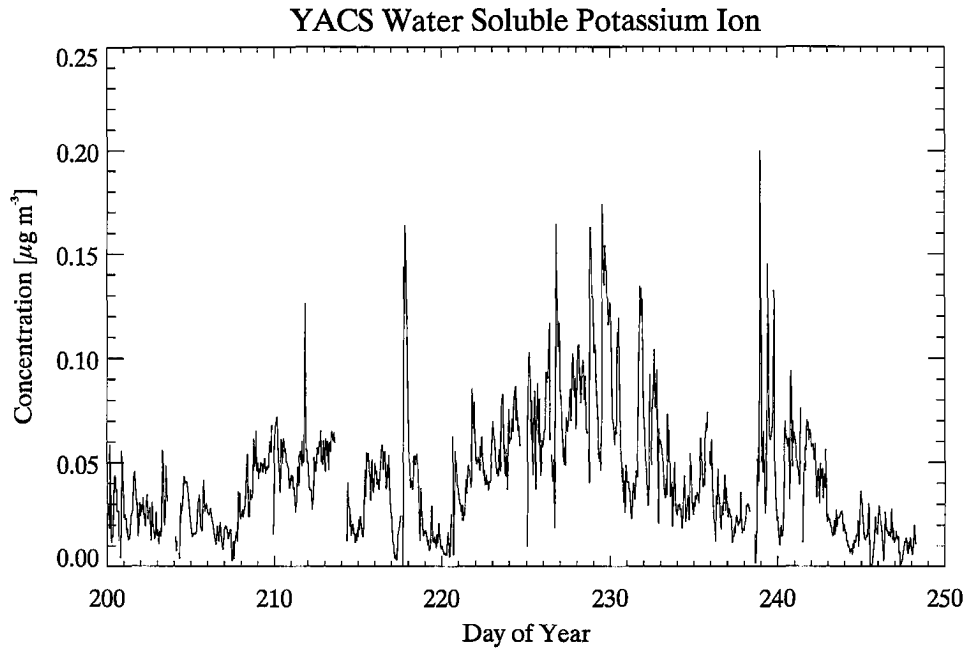
Figure 3.6 Timeline of hourly averaged PILS water soluble potassium ion concentration.
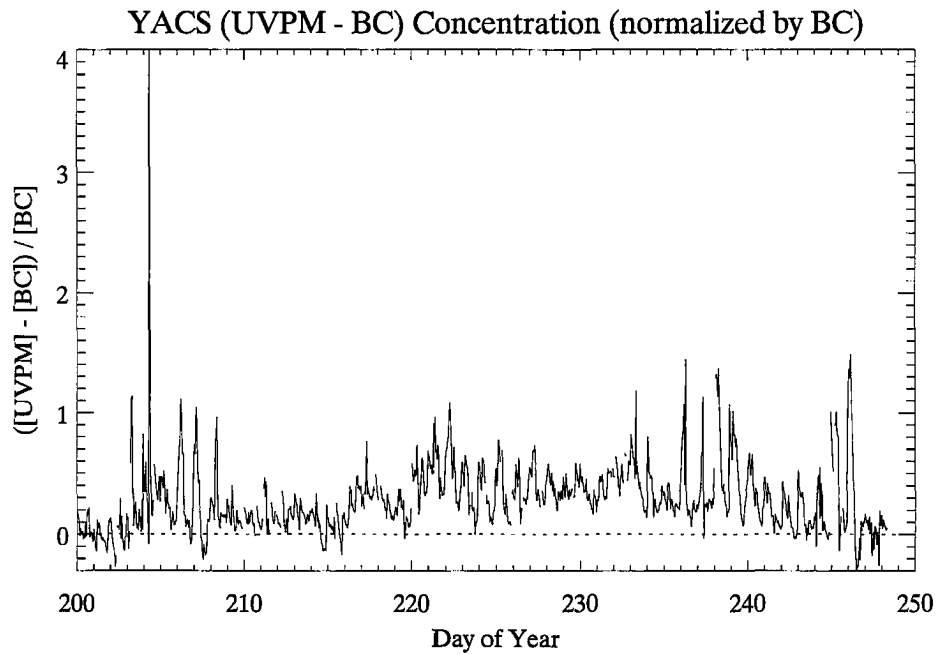
Figure 3.7 Timeline of the difference between UVPM and BC concentrations measured with an aethalometer, normalized by BC concentration.

CHAPTER 4. AEROSOL PHYSICAL AND CHEMICAL PROPERTIES

This chapter presents results from measurements of aerosol physical and chemical

properties during YACS. The method used to merge size distributions measured with the

DMA and OPC is described before the merged data are presented.

4.1 ALIGNMENT METHOD

As described in Chapter 2, the differential mobility analyzer (DMA) sizes an

aerosol particle according to its physical diameter modified by a shape factor to account

for the particle's non-spherical shape. The optical particle counter (OPC) sizes an aerosol

particle by its optical diameter, which is a function of the particle's size and index of

refraction. The index of refraction of an aerosol particle depends on the particle's

composition and the state of the mixture in the particle. Two particles that differ only in

refractive index will be sized in the same measurement channel by the DMA, but can be

sized into different measurement channels by the OPC. If the OPC response to particles

of differing refractive indices is well known, the size distribution measured by the

instrument can be converted into the correct distribution for the actual index of refraction.

Hand and Kreidenweis [2002] introduce a method for aligning OPC and DMA size

distributions by applying trial indices of refraction to OPC volume distributions

following the procedure described in Figure 4.1. For each trial index of refraction, the

routine calculates the DMA data inversion for multiply-charged particles, the OPC

inversion for index of refraction, a Twomey fitting procedure applied to OPC

distributions, a modified Twomey fitting procedure applied to DMA distributions, and a least-squares fit to both sets of data. It was noted in Chapter 2 that OPC data were used to correct DMA data for multiply-charged particles because no impactor was used with the DMA. Even though the DMA data do not depend on the index of refraction, this dependence on the OPC for the multiply-charged particles correction requires its inclusion in the index of refraction iterative loop. The range of trial indices of refraction used here was $1.45 < m < 1.65$ ($\Delta m = 0.005$) and the size range used in the least-squares fit was $0.2 < Dp < 0.7$ μm, following the method of *Hand and Kreidenweis* [2002].

Details of the alignment procedure are provided in *Hand and Kreidenweis* [2002] and will not be repeated in this work. Only a few minor modifications were made to the procedure for its use in YACS. In the original procedure a Twomey algorithm [*Twomey*, 1975; *Winklmayr et al.*, 1990] was applied to the DMA and OPC number and volume distributions to obtain size distributions interpolated to the same diameter grid for comparison purposes. The Twomey algorithm required measured concentrations and experimental uncertainties (described in detail in Appendix B) for each measurement channel as well as diameter limits for each channel and experimental collection kernels derived for the OPC. The collection kernel is used in the algorithm to account for imperfect instrument response. As the DMA inversion also accounts for instrument response, perfect kernels (100% collection for each channel) were assumed for the DMA when the Twomey algorithm was applied. *Markowski* [1987] found that narrow kernels could result in poor inversion of data. For this reason a smoothed linear interpolation of DMA data onto the grid used for the Twomey inversion of the OPC data was used instead of the full Twomey inversion.

The sensitivities of the alignment method to several factors such as the DMA-OPC overlap region and complex index of refraction are described in detail by *Hand* [2001] and will be summarized here. Final aligned size distributions were determined by aligning OPC and DMA data in an overlap region ranging from 0.2 < Dp < 0.7 μm with 18 channels. This range was used in the method's original application to avoid using data near the instrument measurement limits in the alignment. *Hand* [2001] found that increasing the overlap range to 0.1 < Dp < 0.75 μm with 30 channels resulted in a 2-4% change in the retrieved refractive index. Converged distributions were averaged together using a weighted-average algorithm to provide a single aligned distribution. The size ranges used for DMA only, DMA-OPC and OPC only values in the averaging algorithm were altered slightly from their original values used in *Hand and Kreidenweis* [2002]. The size range which consisted of only DMA data was increased to include all particles with D_p < 0.5 μm as there was good confidence in the DMA data up to that point.

The OPC instrument calibration used chemical species that were nonabsorbing at the operating wavelength of the instrument. The alignment method can only retrieve the real part (*n*) of the index of refraction for this reason. *Hand* [2001] provides a discussion of the complications that the treatment of absorbing particles introduces to the alignment. The complications arise because while the OPC calibration uses only nonabsorbing (at the wavelength of the instrument) particles, aerosol particles in the atmosphere can contain absorbing species. In theory, absorbing particles of some geometric diameter can be undersized or oversized compared to nonabsorbing particles of the same geometric diameter. This is because the OPC instrument response is related, through the geometry of the instrument optics, to the intensity of light scattered by a particle. Mie theory can

provide a rough idea of the differences in direction and intensity of the light scattered by absorbing and nonabsorbing particles and the corresponding effect on the instrument response. Despite this, *Hand and Kreidenweis* [2002] found that the uncertainty in retrieved refractive index due to this complication was small (3%) compared to other experimental uncertainties.

The χ^2 statistic was calculated for the least-squares fit between DMA and OPC data for each trial refractive index given by:

$$\chi^2 = \sum_{j=1}^{n} \frac{[g(x_j) + h(x_j)]^2}{\sigma^2(g_j) + \sigma^2(h_j)} \tag{4.1}$$

where $g(x_j)$ and $h(x_j)$ are values of the volume distribution for each instrument in bin j and $\sigma^2(g_j)$ and $\sigma^2(h_j)$ are the variances in each bin. The intercept of the least squares fit was forced to 0 to avoid multiplicative offset between the two data sets. The number of bins used in the comparison is given by n. The refractive index that aligned the DMA and OPC data best was selected using the trial solution with the lowest χ^2. Figure 4.2 shows volume distributions (*dV/dlogDp*) for 1200 PST 9 August 2002 measured by the DMA and OPC for two different indices of refraction. The application of the 1.53 index of refraction resulted in an overestimation of the volume distribution by the OPC while the retrieved value of 1.57 gives much better agreement between the two distributions.

4.2 DATA QUALITY CONTROL

Several criteria were used to accept measurements made with the OPC and DMA as representative of sampled particles. Data from periods during which instrument parameters did not lie within manufacturer's recommendation were removed and were

41

very few in number. The relative humidity (RH) of the excess flow in the DMA increased briefly following instrument flow checks due to the instrument being open to room air. Data were not included in the analysis when the excess flow RH was greater than 15%, which typically included the first 2 or 3 15-minute samples following the daily flow checks. Data collected during the first hour following the restoration of power following an outage that occurred over the night of 25-26 August were also removed to allow the instruments to warm-up. It is believed that failure of the instrument trailer air conditioning system caused elevated temperatures in the trailer the night of 12-13 August. The impact of the elevated temperatures on the instrument performance is uncertain. Anomalously low values of the retrieved index of refraction were found during this period. As a precaution, all data from time periods when the trailer temperature exceeded 35°C were not included in the analysis.

Failure of the LASAIR 1002 model OPC, configured to sample off the same drying inlet as the DMA, made it necessary to perform the alignment using the LASAIR 1003 model OPC that sampled ambient air. Hygroscopic particles can take up varying amounts of water depending on the particle composition and RH. The addition of water results in an increased particle size and a decreased particle refractive index. The response of the OPC to dry and ambient aerosol particles could be very different for hygroscopic particles measured at high RH. Figure 4.3 gives values of RH measured in exhaust flows of the ambient OPC (LASAIR 1003) and dried OPC (LASAIR 1002). The RH of the exhaust flow of the OPCs was lower than the ambient air because of heating effects in the instruments. It is likely that the heating of the aerosol sample in the ambient OPC acted to partially dry the particle, though this drying was not as effective as the

drying system used for the DMA and dried OPC. The overall mean and standard deviation of RH for the ambient OPC exhaust flow was 14 ± 4 % while the mean and standard deviation of the dried OPC (1002) was 6 ± 1 %. Measurements made by *Carrico et al.* [submitted] indicated that the aerosol growth factor, which describes the ratio of wet to dry particle size, was low for RH < 70%. This, combined with the absence of a strong diurnal pattern in χ^2 (see Figure 4.4) and index of refraction values returned by the alignment, which could be expected if there were an RH effect due to the strong diurnal pattern in RH, indicated that the particles sampled by the OPC likely contained as little water as those sampled by the DMA. For this reason no OPC data were removed. Examination of the effects of removing OPC data sampled during periods of RH > 20% and RH > 15% on study averaged aerosol properties showed no significant difference from averages without RH removal.

4.3 AEROSOL SIZE DISTRIBUTION STATISTICS

Aerosol size distribution statistics were calculated for each aligned size distribution during the study. The coarse mode was not fully captured by the instruments used in the alignment procedure, so statistics were performed for the accumulation mode only. The accumulation mode was defined by the minimum in the volume distribution between the two modes [*Hand et al.*, 2002] and was found through an automated routine that sought the minimum volume distribution value between $0.5 < D_p < 2.1$ μm. In cases where there was no obvious minimum in the volume distribution below 2.1 μm, the accumulation mode was assumed to extend to 2.1 μm. In these particular cases there was no evidence of a coarse mode in the DMA/OPC instrumentation, indicating that it was

43

likely present at a large size range not seen by those instruments. In general, particles with $1 > D_p > 2$ μm represented a very small fraction of the total particle number and volume for the size range studied.

Geometric mean diameter (D_{gv}) was calculated using Equation 4.2:

$$D_{gv} = anti\log\left[\frac{\sum_{D_{p,min}}^{D_{p,max}} \log D_{p,m} \dfrac{dV}{d\log D_p} d\log D_p}{V_{mode}}\right] \qquad (4.2)$$

where $D_{p,min}$ and $D_{p,max}$ mark the upper and lower limits of the accumulation mode and $D_{p,m}$ is the geometric midpoint of the bin. The integrated volume (V_{mode}) was calculated by summing over all channels from $D_{p,min}$ to $D_{p,max}$. The $D_{p,min}$ was fixed at 0.038 μm and the $D_{p,max}$ varied between 0.8 and 1.2 μm. Geometric standard deviation was calculated using Equation 4.3:

$$\sigma_g = anti\log\left[\sqrt{\frac{\sum_{D_{p,min}}^{D_{p,max}} \left(\log D_{p,m}\right)^2 \dfrac{dV}{d\log D_p} d\log D_p}{V_{mode}} - \left(\log D_{gv}\right)^2}\right] \qquad (4.3)$$

Number concentrations for the accumulation mode were calculated by integrating number distributions over all channels from $D_{p,min}$ to $D_{p,max}$ and were also computed for the entire measurement range ($0.038 < D_p < 2.1$ μm).

Figure 4.5 presents 15-minute integrated number concentrations. Uncertainty in the number concentrations was on the order of 1% (see Appendix B). Highest number concentrations occurred during the first two weeks of the study, typically peaking near midnight at values on the order of 4000-5000 cm^{-3}. Number concentration values are lower during the heavy regional haze smoke episode, though the diurnal pattern is still

evident, with higher number concentrations found during the night. The peak in number concentration that occurs during the evening of DOY 238-239 (26-27 August) is associated with a local smoke event (see Table 3.1).

Figure 4.6 gives the timeline of integrated accumulation mode volume concentrations. Uncertainty in the integrated accumulation mode volume concentrations was on the order of 1-3%. Two distinct periods of elevated volume are evident during the two regional haze episodes as well as the local smoke event of DOY 238-239 (26-27 August). Relatively elevated volume concentrations were seen during time periods with possible local nighttime smoke influence during the time period DOY 204-208 (23-27 July). The overall mean and standard deviation of the accumulation mode volume concentration was 6.7 ± 3.9 μm^3 cm^{-3} with highest values during the second regional haze event peaking at roughly 27 μm^3 cm^{-3}. The mean concentrations and standard deviation during the first and second regional haze events were 7.9 ± 1.1 and 10.2 ± 4.6 μm^3 cm^{-3}, respectively.

Accumulation mode volume mean geometric diameters are shown in Figure 4.7. Uncertainties were less than 1% (see Appendix B). Highest volume geometric mean diameters were observed during the second regional haze period with values approaching 0.40 μm. Lowest values of D_{gv} were observed during the first week of the study, but displayed more variation during the period. Figure 4.8 presents a scatter plot of accumulation mode D_{gv} with accumulation mode volume. Higher values of D_{gv} correspond to higher volumes through a non-linear relationship. The overall mean and standard deviation of D_{gv} during the study was 0.28 ± 0.05 μm.

Figure 4.9 shows accumulation mode volume geometric standard deviations. The overall average was 1.67 ± 0.11, with largest values observed during the first half of the study and lowest values seen during the second regional haze episode. A strong relationship between σ_g and D_{gv} is evident in Figure 4.10, with the lowest standard deviations corresponding to higher mean diameters. This may reflect the aging of particles, which can result in increased particle size as mass is added and a narrowing of the standard deviation, approaching about 1.5. This is supported by a theoretical analysis suggesting that competing mechanisms of distribution broadening and narrowing result in a stable size distribution, known as the "self-preserving size distribution" [*Hinds*, 1982].

Figure 4.11 shows a contour plot of volume distributions for the entire study. Higher volume distribution values are given in warmer colors with diameter on the abscissa and day of year on the ordinate. Regional smoke haze episodes are clearly visible with high volume distribution values near 0.3-0.5 μm from DOY 208-215 (27 July – 3 August) and DOY 222-234 (10-22 August). The shift to larger diameters during smoke haze episodes can also be seen in the distributions. Volume distribution values above 1.0 μm are low except during the heaviest smoke haze periods (~ DOY 226-234; 14-22 August), though they are still much lower than the values below 1.0 μm. It is difficult to see the presence of the small tail of the coarse mode in Figure 4.11 due to low instrument resolution in this size range and low numbers of particles in this size range. As the method used to determine the location of the accumulation mode upper size limit depended on the location of a minimum value in this range, confidence in the upper size limit of the accumulation mode is low. It was often difficult to determine the end of the accumulation mode and the start of the coarse mode tail from volume distributions.

Modifying the upper limit of the accumulation mode had a small effect on the accumulation mode number and volume concentrations, but had noticeable, but still quite small, effects on D_{gv} and σ_g, particularly during the early part of the study when D_{gv} was small.

Number distributions are shown in Figure 4.12 using the same method used to illustrate volume distributions in Figure 4.11. High concentrations of sub-100 nm particles are immediately noticeable during the first two weeks of the study and are responsible for the high observed number concentrations during this time (Figure 4.5). Number distributions become bimodal during the two regional smoke haze episodes, especially so for the second episode. Diurnal and longer term patterns in number and volume distributions are discussed in greater detail in Chapter 6.

4.4 AEROSOL COMPOSITION

Data from a number of aerosol composition measurements were available for analysis and comparison to aerosol physical sizing data. While beyond the scope of this paper, a detailed discussion of the comparisons between various measurement techniques and analysis methods is available [*Malm et al.*, in progress]. This paper will use IMPROVE results for organic carbon (OC) and elemental concentrations used to generate soil concentrations, Aethalometer results for black carbon (BC) concentration, and URG filter sampling system results for ion concentrations. Measurement techniques used to obtain these data are described in Chapter 2 and in further detail in *Lee et al.* [in progress] and *Malm et al.* [in progress]. Aerosol composition measurements represent integrated

24-hour samples, collected from approximately 0800 PST to 0800 PST the following day, of $PM_{2.5}$ aerosol and are given in Appendix C.

Sulfate was fully neutralized by ammonium throughout most of the study, the exception being periods near the beginning and end of the study. Figure 4.13 presents a timeline of the ammonium to sulfate molar ratio. The average and standard deviation of the molar ratio was 2.04 ± 0.19. Mass fractions of $PM_{2.5}$ composition are presented in Figure 4.14. The composition of ammoniated sulfate species was assumed to vary between $(NH_4)_2SO_4$ and $(NH_4)_3HSO_4$ depending on the molar ratio value. Excess ammonia was assumed to be associated with nitrate in the form of NH_4NO_3 and any remaining nitrate was assumed to be associated with sodium in the form of $NaNO_3$. Organic carbon mass was given as carbon determined by thermal optical reflectance (TOR) combustion [*Chow et al.*, 1993] multiplied by a molecular weight to carbon weight ratio (OM/OC) of 1.9. This ratio accounts for the mass of non-carbon species such as O and N that are present in the organic compounds. The value of 1.9 is used because it gives the best agreement between reconstructed mass concentrations computed from composition data and observed gravimetric mass concentrations [*Malm*, personal communication]. *Turpin and Lim* [2001] suggest values of C/M of 1.6 for urban aerosols and 2.1 for remote aerosols that bracket the 1.9 value used in this study. Soil composition was reconstructed from IMPROVE elemental mass concentrations using Equation 4.4:

$$[soil] = 2.20[Al] + 2.49[Si] + 1.63[Ca] + 2.42[Fe] + 1.94[Ti] \qquad (4.4)$$

On average, OM was by far the dominant $PM_{2.5}$ species during the study with an average (and standard deviation) mass fraction of $65 \pm 15\%$, reaching maximum values during regional smoke/haze episodes on the order of 85%. Ammoniated sulfate was the

48

next most abundant species with an average (and standard deviation) mass fraction of 20 ± 11%. Average mass fractions of the remaining species were less than 10%, with soil as 6.9 + 3.1%, sodium nitrate as 4.3 ± 3.5%, BC as 2.9 ± 0.5% and ammonium nitrate as 1.3 ± 1.6%.
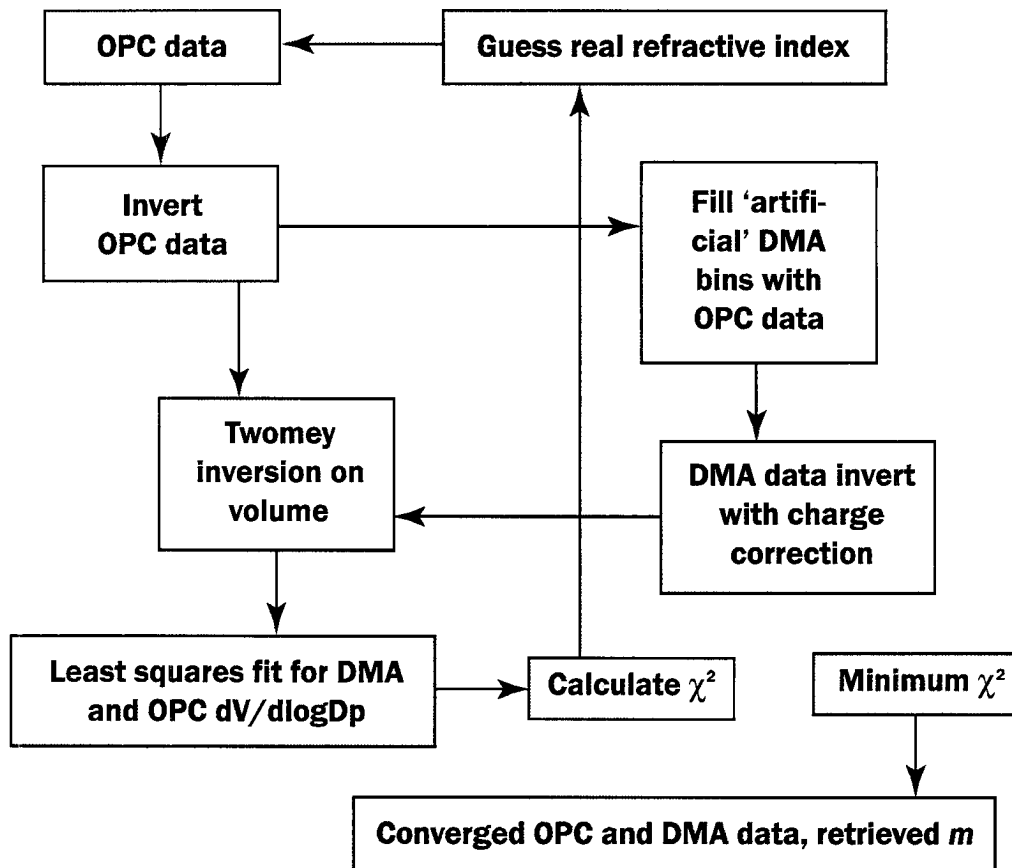
Figure 4.1 Schematic of the alignment procedure from *Hand and Kreidenweis* [2002].

YACS Unaligned and Aligned dV/dlogDp (9 August)
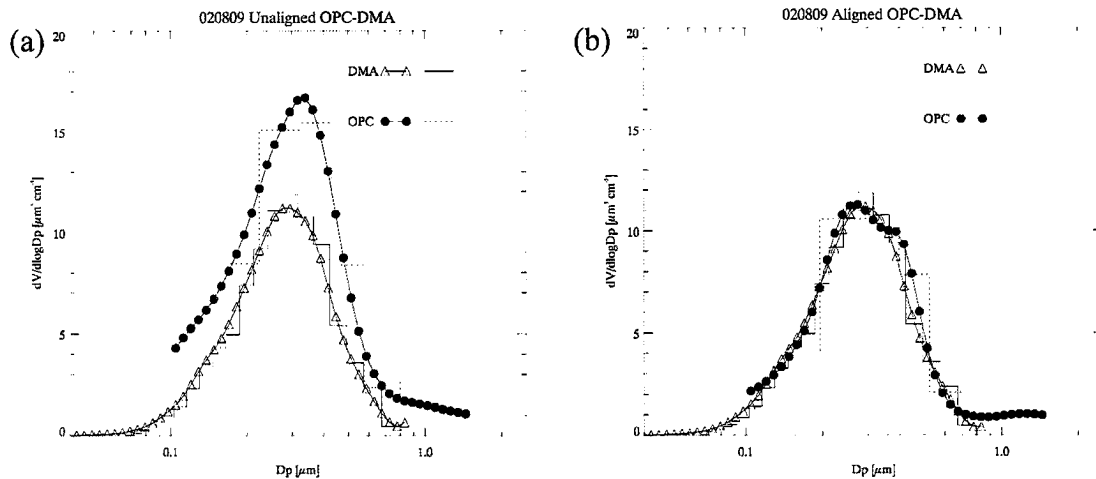
Figure 4.2 (a) Unaligned OPC and DMA volume distributions for 9 August 2002. A refractive index of m = 1.53 was applied to the OPC data. Data for both instruments are shown as histograms representing instrument bins overlaid with Twomey distributions. (b) Aligned OPC and DMA volume distributions for the same case as in (a), except a refractive index of m = 1.57 (corresponding to the minimum χ^2) was applied to OPC data.
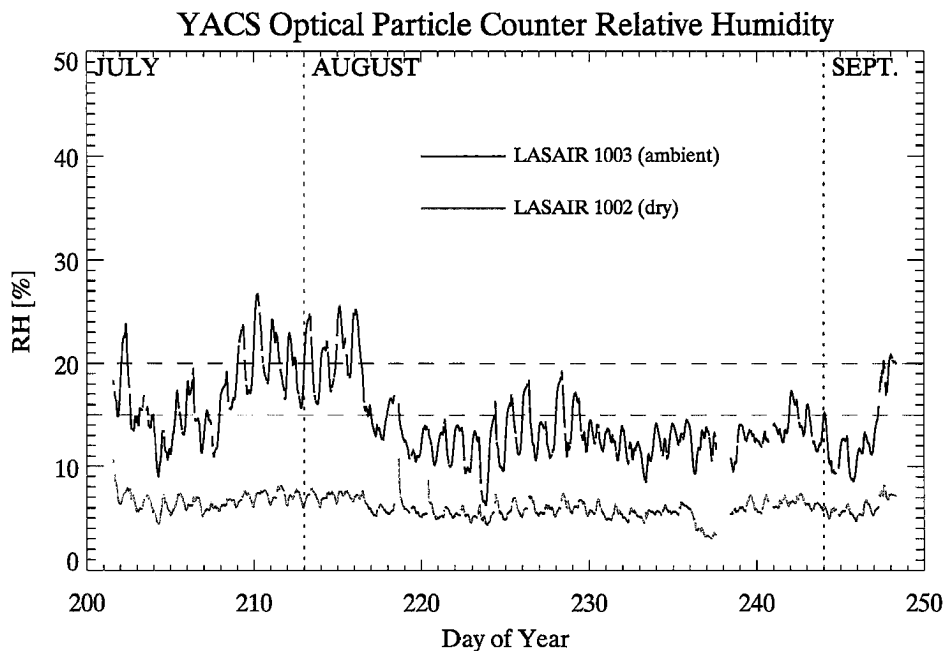
Figure 4.3 Instrument relative humidity of exhaust flow for the ambient (1003) and dried (1002) OPC models. Reference values are given at 15 and 20% as dashed lines.

51
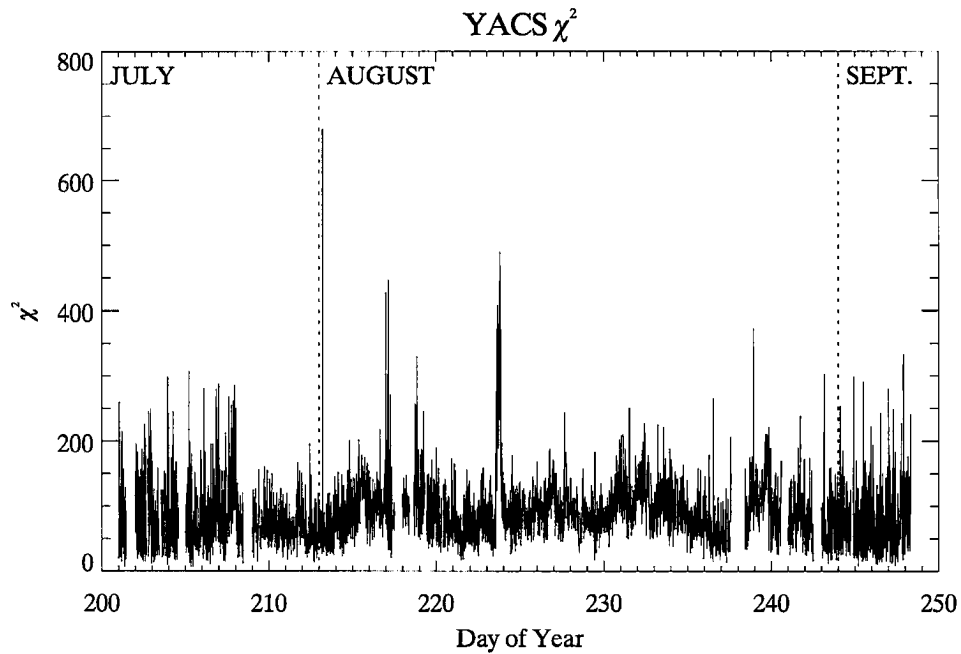
Figure 4.4 Values of the minimum χ^2 statistic calculated for the least square fit of OPC and DMA volume distributions. The refractive index and aligned size distribution were selected based on this criterion.
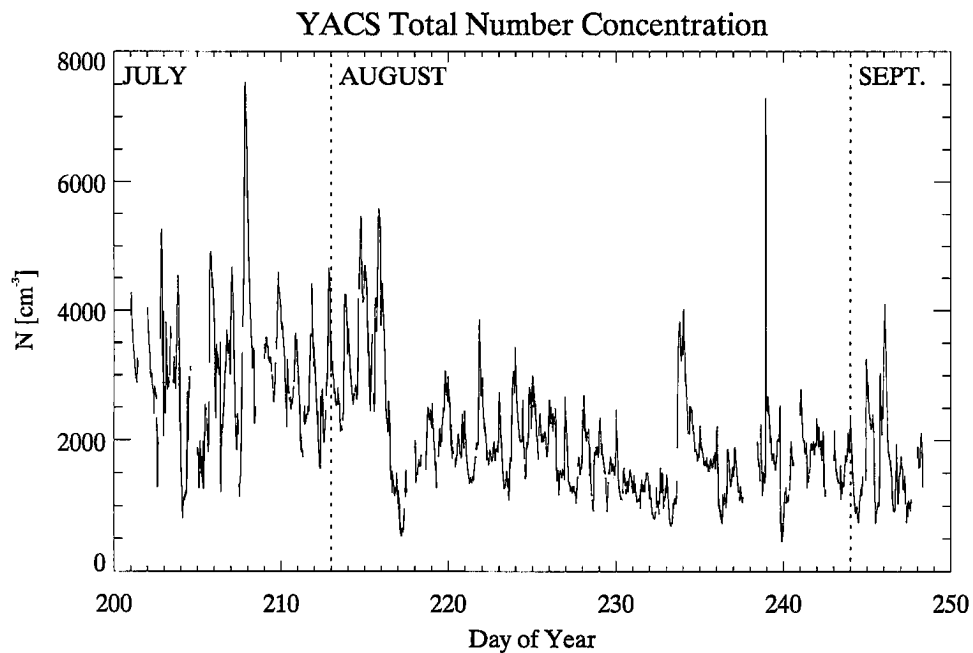
Figure 4.5 Integrated total number concentrations from measured dry size distributions.

52
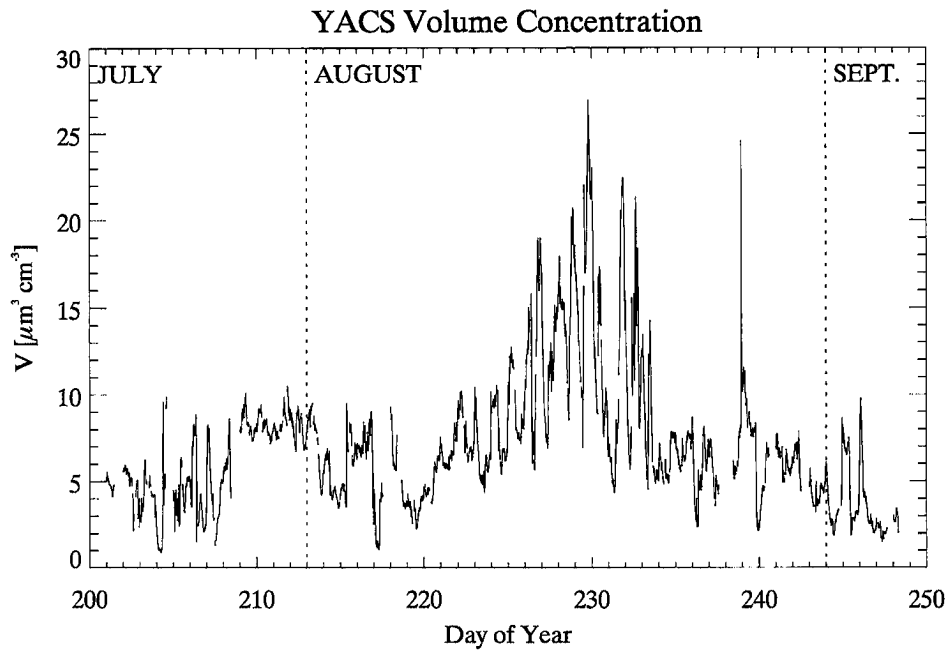
Figure 4.6 Total volume concentrations integrated from dry size distributions.
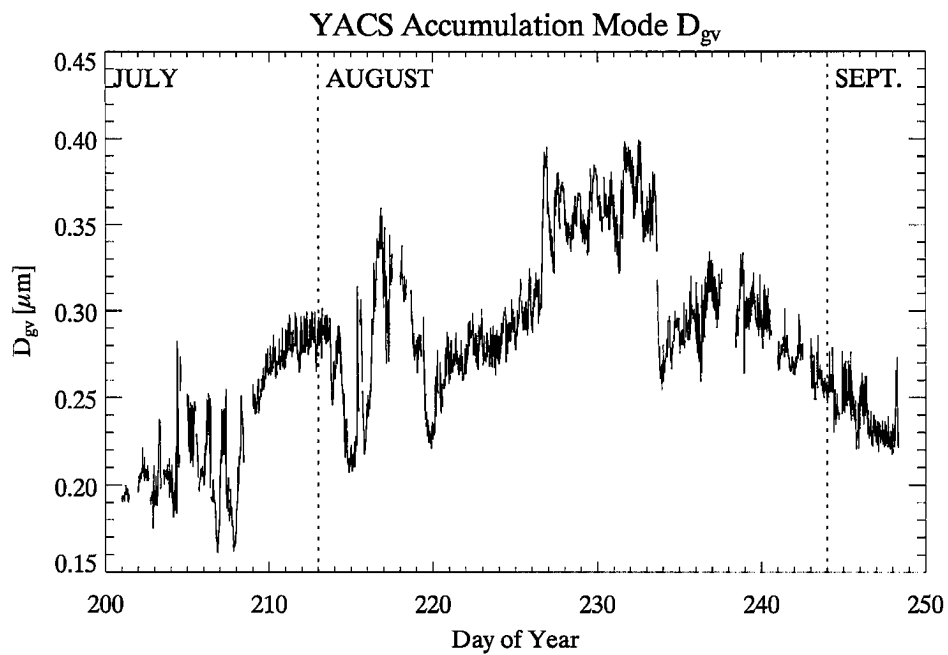
Figure 4.7 Accumulation mode volume mean geometric diameter (D_{gv}).
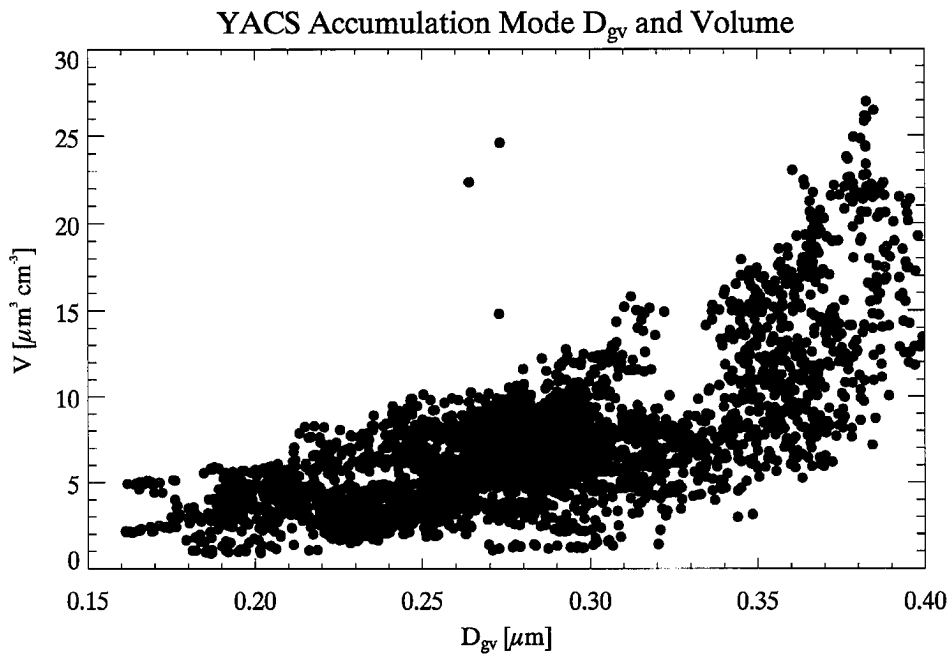
Figure 4.8 Accumulation mode D_{gv} and integrated accumulation mode volume from dry size distributions.
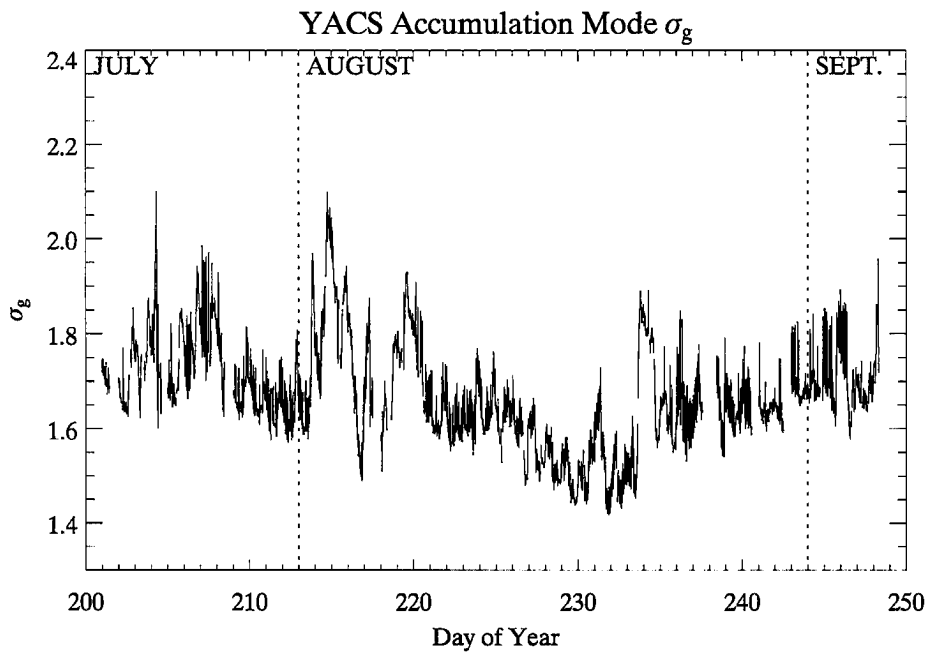
Figure 4.9 Accumulation mode volume geometric standard deviation (σ_g)

54
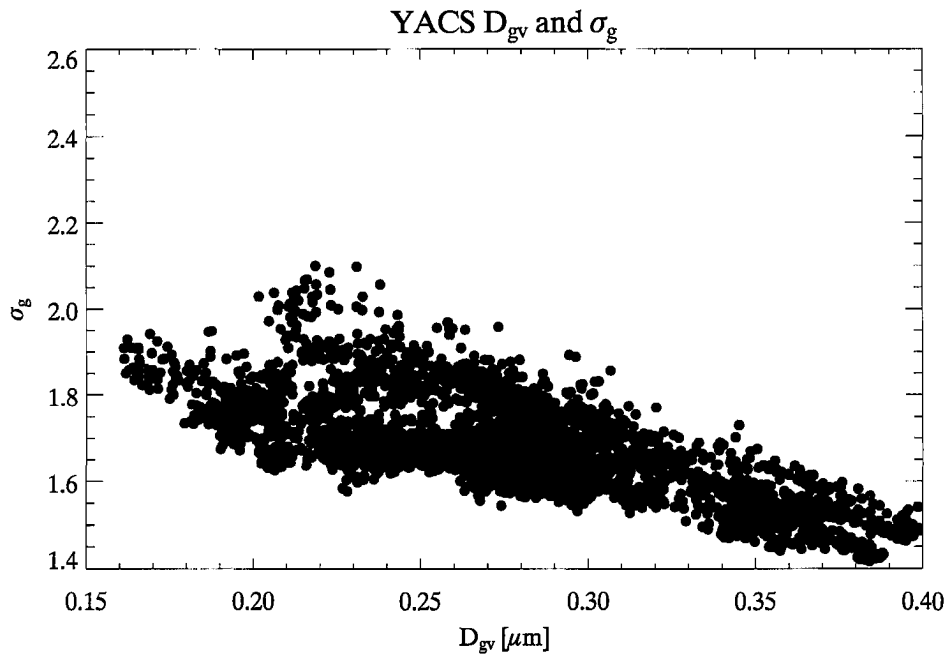
Figure 4.10 Accumulation mode dry geometric mean diameter and standard deviation.
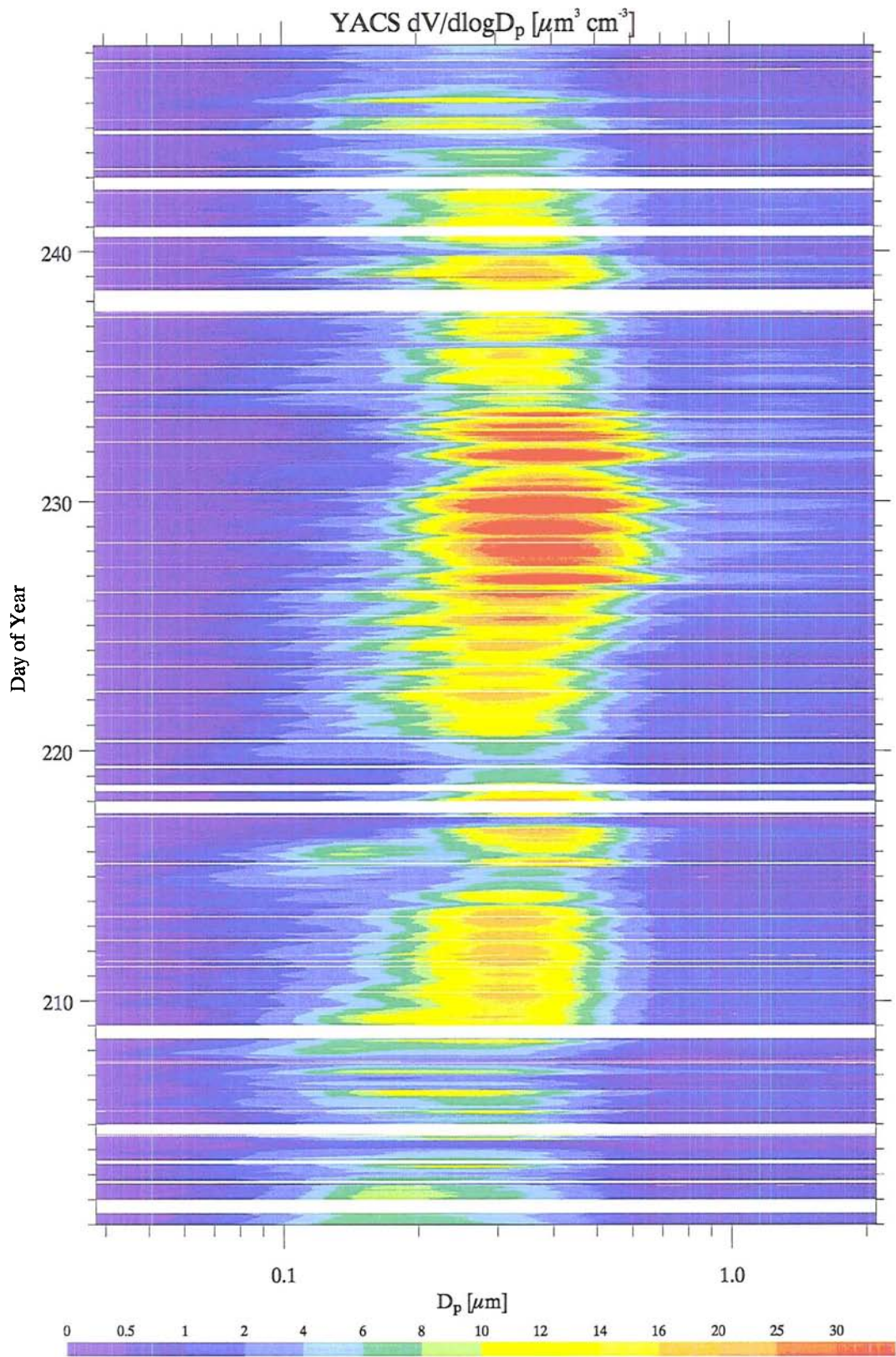
Figure 4.11 Contours of dry volume distributions.
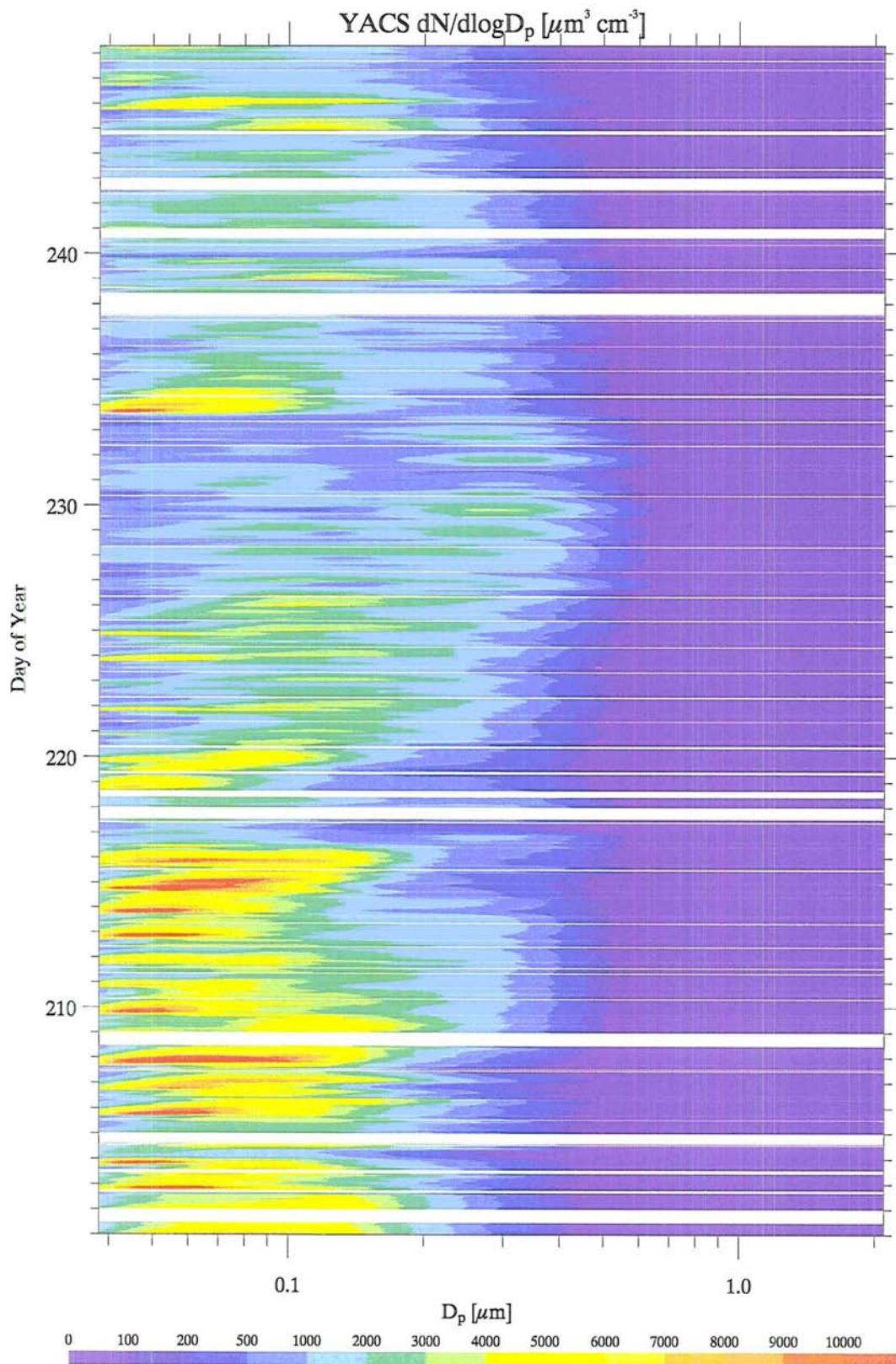
Figure 4.12 Contours of dry number distributions.
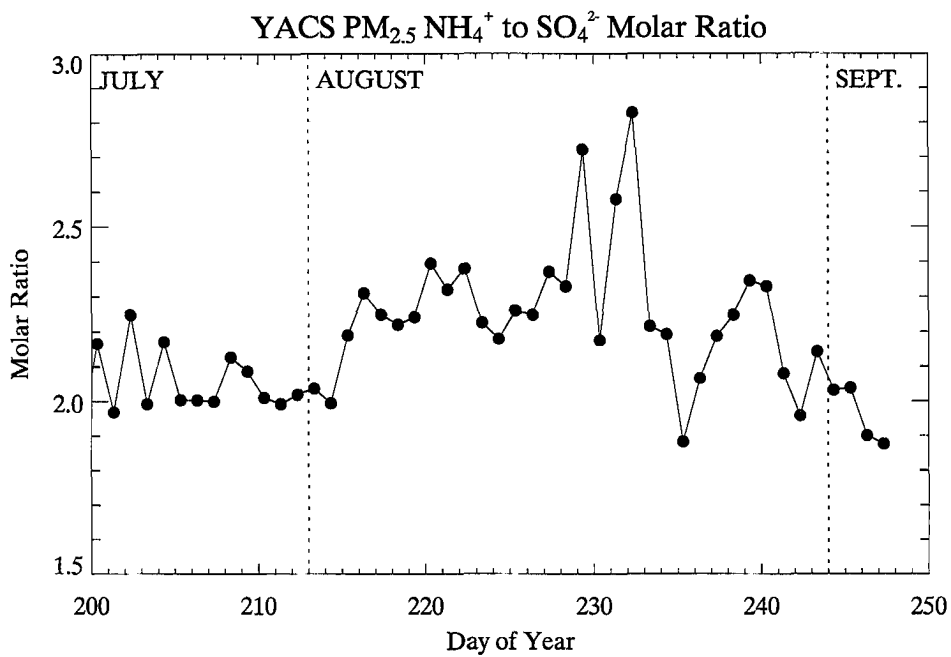
Figure 4.13 Ammonium to sulfate molar ratios calculated from $PM_{2.5}$ data.
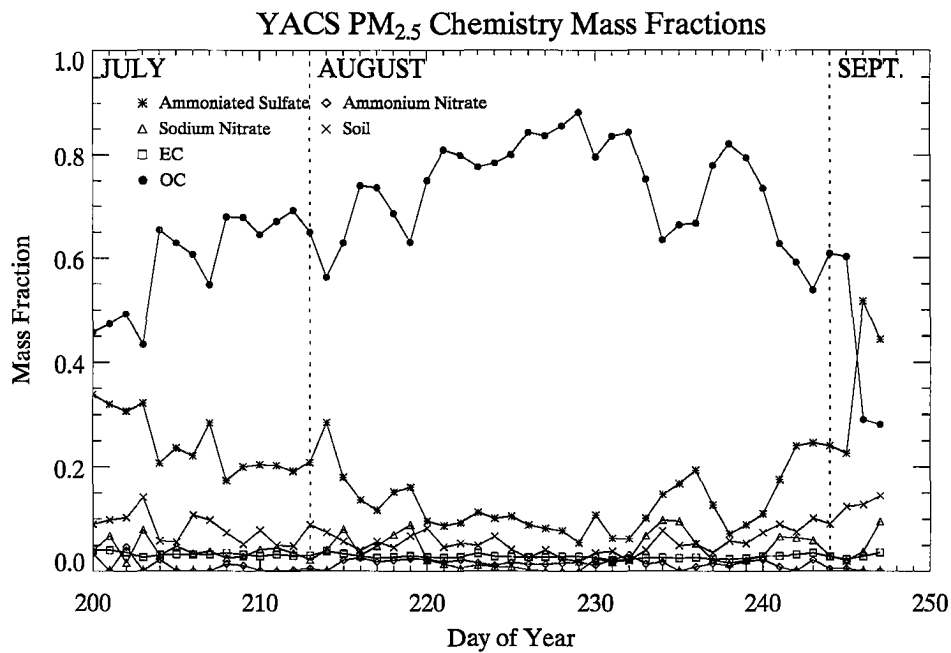
Figure 4.14 $PM_{2.5}$ composition mass fractions.

58

CHAPTER 5. VISIBILITY ESTIMATES

Total light extinction coefficients (b_{ext}) are common diagnostics used to indicate visibility levels. The IMPROVE network measures total extinction with transmissometers and scattering with nephelometers. These measurement techniques are integrative measurements that do not provide any information on the size or chemical makeup of the particles (or gases) responsible for the extinction. Impactor measurements provide some idea of the size and composition dependence of light extinction though these methods may not capture all species present in the aerosol, have low resolution and are analytically expensive. Mie theory applied to aerosol size distributions can be used to reconstruct particle scattering coefficients given some estimate of the index of refraction and assuming spherical particles.

Extinction coefficients can be calculated from measurements of aerosol composition using a linear model, given certain mixing assumptions [*Ouimette and Flagan*, 1982]. Defining α_i as the scattering and absorption efficiencies per unit mass and c_i as the mass concentrations for species i, the extinction coefficient can be given as:

$$b_{ext} = \sum_i^N \alpha_i c_i \qquad (5.1)$$

where N is the number of species present in the mixture. This model is valid only if the aerosol is externally mixed, i.e., each particle is composed of a single chemical species, or if the aerosol is internally mixed in fixed proportion that does not vary with size. Humidification factors can be applied to the mass scattering efficiencies of hygroscopic

species to account for water uptake in the model. *Malm et al.* [1994] use the linear model to estimate reconstructed particle scattering and absorption from IMPROVE network measurements of sulfate, nitrate, organics, soil, light absorbing carbon (LAC) and coarse mass concentration. Values of α_i used in the study are given in Table 5.1. Scattering efficiencies for sulfate and nitrate compounds were assigned a value of 3 m^2 g^{-1} based on a nominal size distribution and were expected to vary between 1-4 m^2 g^{-1} [*Malm et al.*, 1994]. Organic carbon mass (OM) is assumed to have a scattering efficiency of 4 m^2 g^{-1} because of its lower density. Observations of these values vary substantially and have a significant impact on the calculated extinction [*Lowenthal and Kumar*, 2003; *Watson*, 2002; *Zhang et al.*, 1994].

In general, the linear reconstruction methods listed above perform best in regions where the fine aerosol is dominated by sulfate compounds, where scattering properties are relatively well understood. One goal of this study was to better characterize the scattering properties of organic particles. Scattering properties of organic particles are not well understood due to the incomplete identification of the multitude of compounds, the form these compounds take in atmospheric particles and the lack of size distribution observations [*Watson*, 2002]. This chapter presents results of scattering calculations performed using measured YACS size distributions and compares findings with direct measurements of light scattering and light scattering reconstructed from composition observations. Chapter six provides further discussion on the significance of the results, explores the effect of changing various assumptions used to obtain the results in this chapter and compares YACS results with other scattering and optical property measurements reported in the literature for biomass burning aerosol.

5.1 MIE THEORY AND SCATTERING CALCULATIONS

Light scattering coefficients were calculated using size distribution measurements of the aerosol particles over the size range $0.038 < D_p < {\sim}2.1$ μm. Light scattering by particles is one of four components of the total light extinction coefficient, which is given in Equation 5.1:

$$b_{ext} = b_{sp} + b_{sg} + b_{ap} + b_{ag} \qquad (5.1)$$

where b_{sp} is light scattered by particles, b_{sg} is light scattered by gases, b_{ap} is light absorption by particles and b_{ag} is absorption by gasses [*Seinfeld and Pandis*, 1998]. Scattering by gas particles is pressure dependent and is known as Rayleigh scattering, which has been well described in the literature. Light absorption by gasses at visible wavelengths is mainly due to NO_2 and is negligible at a remote site such as Yosemite National Park. Light absorption by particles in the visible wavelengths is more complicated. Black carbon (BC) is usually assumed to be the main absorbing particle type; however several mineral dust species can also absorb light at visible wavelengths [*Tegen et al.*, 1996]. It has also been speculated that certain forms of organic carbon (OC) can absorb light at visible wavelengths [*Gelencser et al.*, 2003; *Mayol-Bracero et al.*, 2002].

An assumption for the value of the true complex index of refraction ($m = n - ki$) allows for the calculation of b_{sp} from measured volume distributions using Equation 5.2:

$$b_{sp} = \int \frac{3}{2} \frac{Q_{sp}}{D_p} \frac{dV}{d \log D_p} d \log Dp \qquad (5.2)$$

where $Q_{sp}(D_p, m, \lambda)$ is the Mie scattering efficiency for spherical particles and λ is the wavelength ($\lambda = 530$ nm). The complex refractive index includes a real (scattering) part (n) and an imaginary (absorbing) part (k). The scattering contribution for any size range of particles can be calculated by fixing the limits of the integral in Equation 5.2. Replacing Q_{sp} with the Mie extinction efficiency (Q_{ep}) in Equation 5.2 gives extinction coefficients (b_{ep}). The difference between the scattering and extinction coefficients is the absorption coefficient.

Determination of Q_{ep} requires a value for the imaginary (absorbing) part of the complex index of refraction, which can be calculated from measurements of BC. These calculations are sensitive to the type of mixing that is assumed between the absorbing BC and non-absorbing components of the aerosol. Results in this chapter assume volume-homogenous mixing between the two components. A model that assumes the internally mixed particles consist of an absorbing core surrounded by a nonabsorbing shell may be more reasonable for biomass burning aerosol [*Martins et al.*, 1998].

5.2 AEROSOL SCATTERING RESULTS

Estimates of m were calculated from measurements of aerosol composition for comparison with retrieved refractive index ($m_{ret} = n_{ret} - 0i$). The retrieved refractive index consists of a nonzero n and a zero k component because the alignment method can not determine the imaginary part of the refractive index. The calculated values ($m_c = n_c - k_c i$) of the refractive index were determined using the volume weighted method of *Stelson* [1990] given by Equation 5.3:

$$\overline{m} = \overline{\rho} \sum_i \frac{X_i n_i}{\rho_i} - \overline{\rho} \sum_i \frac{X_i k_i}{\rho_i} i \qquad (5.3)$$

with

$$\frac{1}{\overline{\rho}} = \sum_i \frac{X_i}{\rho_i} \tag{5.4}$$

where n_i is the real part of the index of refraction for species i and k_i is the imaginary (absorbing) part, ρ_i is the density of the individual species and X_i is the mass fraction of species i. Table 5.2 gives values used in the calculation for the species observed during the study used to determine m_c. OC was the dominant aerosol species during the study, especially so during smoke-haze episodes, so m_c is most sensitive to the density and index of refraction assumed for OC. Mass fractions of the species used in the calculation are shown in Figure 4.14. The values given for the refractive index (1.55) and density (1.4) of OC are based on detailed measurements of various organic species in urban areas, but have been applied in both urban and remote locations [*Dick et al.*, 2000; *Hand and Kreidenweis*, 2002; *Stelson*, 1990; *Turpin and Lim*, 2001; *Zhang et al.*, 1994]. As the properties of OC and soil depend, respectively, on the presence of many different organic compounds and mineral compounds present in a given particle, it is likely that values given in Table 5.2 for soil and OC may vary substantially for different aerosol types.

Figure 5.1 presents timelines n_{ret}, the retrieved refractive index, and the calculated refractive index, n_c. Good agreement is observed between n_{ret} and n_c for the duration of the study. Best agreement is found during the early and late periods of the study when OC concentrations were low. During carbon dominated periods there is a bigger difference between n_{ret} and n_c, but it is still small, 1-2%, within the experimental uncertainty. Larger differences during carbon dominated periods suggest that the assumed refractive index for OC was too low. Overall there was little variation in n_{ret} and n_c during the study, reflecting the nearly continual presence of a dominant carbon mass

fraction. The mean and standard deviation were 1.577 ± 0.008 for n_{ret} and 1.570 ± 0.006 for m_c.

Figure 5.2 gives values for the imaginary part of the complex index of refraction calculated using Equation 5.4 and concentrations of BC measured with an aethalometer. The average ($\pm$ one standard deviation) imaginary part of the index of refraction was 0.015 ± 0.003 and ranged between approximately $0.01 < k < 0.025$. Highest values for k were found during the early and late periods of the study, reflecting a larger contribution by BC to total $PM_{2.5}$ mass.

The timeline of b_{sp} computed using Equation 5.2 is given in Figure 5.3. The real part of the refractive index used in the Mie computation was n_{ret} and was specific to each 15-minute dry size distribution. The imaginary part of the refractive index was assigned the value of k calculated for that day using Equation 5.3. Volume homogenous mixing of the absorbing and nonabsorbing species was assumed in the calculation. The average ($\pm$ one standard deviation) total dry b_{sp} was 49 ± 36 Mm^{-1} with highest values observed during the heavy smoke-haze episode that occurred in mid- to late August. Elevated values are also seen during the first smoke-haze episode beginning in late July. Experimental uncertainties due to uncertainties in particle losses in the sampling lines were roughly 7%. Calculated dry b_{sp} tracks well with total volume concentration. Figure 5.4 shows an approximately linear relationship between calculated b_{sp} and total volume during the study.

5.2.1 Light scattering distributions

Light scattering coefficient distributions ($db_{sp}/dlogD_p$) were calculated to explore the relationship between particle size and visibility degradation. Figure 5.5 presents the

scattering distribution for a day during the smoke-haze episode, 15 August 2002 (DOY 227). The figure shows that particles between $0.25 < D_p < 0.6$ μm were responsible for the vast majority of the scattering on this day, with a peak at ~ 0.45 μm. There was a very small contribution to light scattering by particles larger than 1.0 μm on this day. The light scattering coefficient distribution on a clean day (DOY 242, 30 August) is also shown in the figure. Overall the scattering coefficient is much lower than for the smoke-haze case. In addition, the peak in the scattering distribution occurs at a lower size, ~ 0.3 μm. Figure 5.6 presents the timeline of calculated accumulation mode (as defined previously in Chapter 4) b_{sp} geometric mean diameter (D_{gb}). Accumulation mode volume geometric mean diameter (D_{gv}) is also plotted for comparison. A clear shift to larger sizes in both parameters can be seen during the August regional smoke-haze period. The two diameters tracked well, though D_{gb} was always the larger of the two. As can be seen in Figure 5.7, increasing D_{gv} corresponded to increasing D_{gb}. If there was no size dependence on scattering, one might expect D_{gv} and D_{gb} to be the same, as they would both track with particle volume distributions and would thus fall on the one-to-one line shown on Figure 5.7. The larger values of D_{gb} show that larger particles contributed more effectively to light scattering. That is, despite the fact that there may have been more particles of a smaller size on a volume basis, the scattering distributions peaked at larger size because those particles are most effective at scattering. As D_{gv} approached 0.4 μm, the two distributions merged, indicating these size particles are near the peak in scattering efficiency. Calculated accumulation mode b_{sp} and D_{gb} are compared in Figure 5.8. Larger D_{gb} correspond to higher b_{sp}, consistent with the relationship between D_{gb} and D_{gv} described above. The relationship weakens for $D_{gv} > 0.4$ μm, when higher scattering is

observed due to increased numbers of particles with effective scattering diameters rather than shifts in size to those diameters. Figure 5.9 presents contours of calculated dry b_{sp} distributions for the entire study. The previously discussed trends in light scattering can be seen in the figure: increased scattering during smoke periods, importance of particles with $0.3 < D_p < 0.6$ μm to scattering and the shift of b_{sp} distributions to larger sizes during periods with heaviest light scattering.

5.2.2 Light extinction and absorption

Light extinction coefficients were calculated in a similar fashion to b_{sp}, except the imaginary portion of the complex refractive index calculated as described above was included. Figure 5.10 gives the Mie scattering and absorption efficiencies as functions of particle size for three complex refractive indices ($m = 1.57 - 0i$, $m = 1.57 - 0.02i$, $m = 1.54 - 0i$), two which represent typical retrieved results with and without an absorbing component, and one intended to illustrate the effect of ignoring the absorption component of the refractive index. Homogenous volume mixing was assumed in the calculations. A portion of the light that would have been scattered by the absorbing particle is instead absorbed. This effect becomes larger as the particles increase in size, as the absorption efficiency of the particle increases with size. As can be seen in Figure 5.10, the absorbing particle has roughly the same scattering efficiency as the non-absorbing particles for sizes less than 0.3 μm. As a significant portion of the scattering calculated for YACS size distributions occurs at sizes larger than this, we expect to see lower b_{sp} in calculations performed assuming absorbing particles as opposed to calculations that assume non-absorbing particles. Inclusion of the absorbing part of the refractive index has roughly the

same effect as reducing the real part of the refractive index. The Mie scattering efficiencies with refractive indices $m = 1.54 + 0i$ and $m = 1.577 + 0.02i$ are nearly equal for $D_p < 0.45$ μm, which includes the particles responsible for the majority of the scattering during YACS (see Figure 5.10). This suggests that light scattering calculations that do not account for light absorption by particles will return approximately the same b_{sp} as calculations that do account for absorption with substantially lower real components of the refractive index. Calculations that failed to include the absorbing part of the refractive index were roughly 7% higher than calculations that included the absorbing part.

5.2.3 Comparison with measured scattering

Dry PM$_{2.5}$ b_{sp} ($\lambda = 530$ nm) was measured by the National Park Service (NPS) using an integrating nephelometer (Model M903, Radiance Research, Seattle, WA) with a PM$_{2.5}$ size cut. *Malm and Day* [2000] provide a detailed description of the drying system and the instrument. Uncertainty in the instrument calibration resulted in loss of nephelometer data prior to DOY 215 (3 August) [*Malm*, personal communication]. Scattering coefficients calculated using size distribution measurements with $m = n_{ret} + k_c i$ were compared to direct measurements of b_{sp}. Figure 5.11 gives timelines of calculated b_{sp} and measured b_{sp} during the study. Calculated b_{sp} was higher than measured b_{sp}, but agreed well for trends showing extremely good correlation (see Figure 5.12). The overall average ($\pm$ one standard deviation) percent difference was 6.1 $\pm$ 5.4%. A previous study that used the same alignment method applied to YACS measurements showed a similar, though somewhat larger, difference between calculated and measured b_{sp}.

5.2.4 Mass scattering efficiency

Estimates of mass scattering efficiency (α_s) were made by applying size distributions and calculated light scattering coefficients $(m = n_{ret} + k_c i)$ to Equation 5.5:

$$\alpha_s = \frac{b_{sp}}{M} = \frac{b_{sp}}{V\rho} \tag{5.5}$$

The mass concentration was determined by multiplying the integrated volume concentration (V) over all sizes $(0.038 < D_p < 2.1\ \mu m)$ times density calculated for each day based on composition measurements. It should be noted that some bias may be present due to the presence of water on filters analyzed for gravimetric mass due to the fact that filters are weighed at an equilibration RH (35%). This effect is likely to be small due to the low growth factors observed at the equilibrium RH for aerosol sampled during the study [*Carrico et al.*, submitted]. Some mass may be lost from the filter due to volatilization of semi-volatile OC that is not completely accounted for. Figure 5.14 gives a timeline of α_s during the study and represents all fine species present (mostly OC and ammoniated sulfate). The average mass scattering efficiency (± one standard deviation) was $4.3 \pm 0.8\ m^2\ g^{-1}$ with highest values (~ $6\ m^2\ g^{-1}$) occurring during the smoke-haze periods and lowest values occurring during the higher sulfate contribution times during the early and later portions of the study. Note that these values are substantially higher than the values used for the most abundant species observed during YACS, $4\ m^2\ g^{-1}$ for OC and $3\ m^2\ g^{-1}$ for sulfates and nitrates, which are used by the IMPROVE program to calculate scattering (given in Table 5.1). The higher scattering efficiency observed during YACS is likely a combination of slightly higher refractive indices (1.57 as opposed to 1.55) and narrower size distributions at larger sizes (more particles at effective scattering

68

diameters) than those assumed to generate the value of 4 m^2 g^{-1} for OC α_s by IMPROVE. Light scattering reconstructed from chemical measurements using these numbers would underestimate total scattering, by as much as 50%, especially during heavy smoke/haze periods when calculated values of α_s approach 6 m^2 g^{-1}. Values of α_s observed in YACS are compared to previous findings for biomass burning aerosol in the next chapter.

Table 5.1 Values used in IMPROVE webs site to determine light extinction from composition measurements.

Species	Dry Mass Scattering Efficiency $(m^2 g^{-1})$
Sulfate	3
Nitrate	3
OMC	4
Soil	1
Coarse mass	0.6
EC	10[*]

[*] Mass absorption efficiency

Table 5.2 Physical constants of species used to calculate refractive index and density.

Species	Density (g cm^{-3})	Index of Refraction
$(NH_4)_3H(SO_4)_2$	1.83[1]	1.527[1]
$(NH_4)_2SO_4$	1.76[2]	1.531[2]
Organic Carbon	1.4[3]	1.55[1]
Elemental Carbon	2.0[4]	1.96-0.66[4]
NH_4NO_3	1.725[5]	1.564[5]
$NaNO_3$	2.261[2]	1.587[2]
Soil	4[6]	2[6]

[1] *Stelson* [1990]
[2] *Tang* [1996]
[3] *Dick et al.* [2000]
[4] *Seinfeld and Pandis* [1998]
[5] Handbook of Chemistry and Physics, 61st Edition (1980-1981)
[6] Based on values reported in *Hand and Kreidenweis* [2002]

YACS Dry Refractive Index
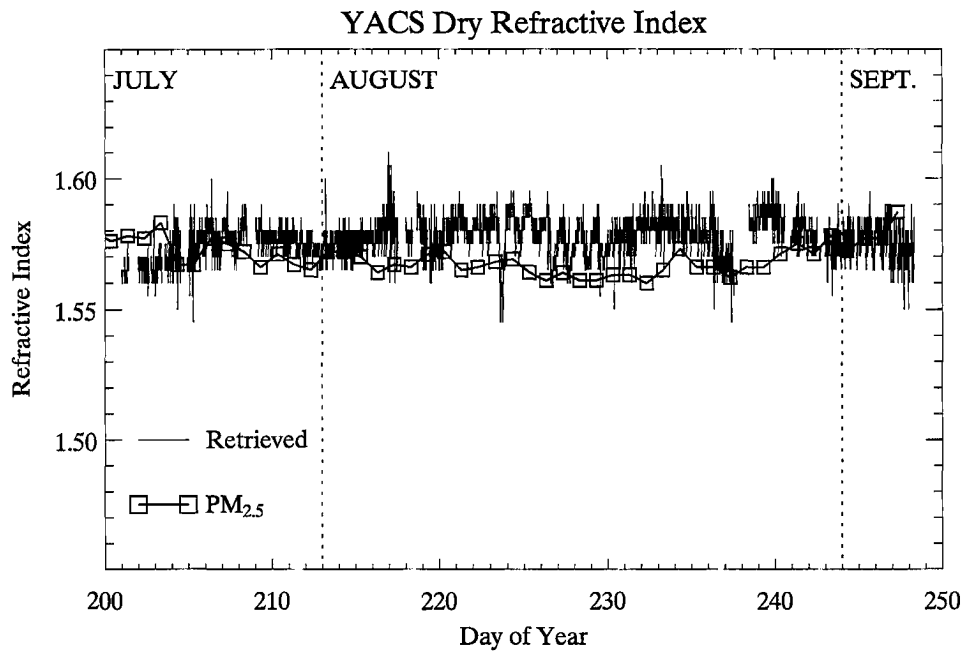
Figure 5.1 Retrieved dry refractive indices with computed fine estimates using chemical compositions.

YACS Imaginary Part of Refractive Index
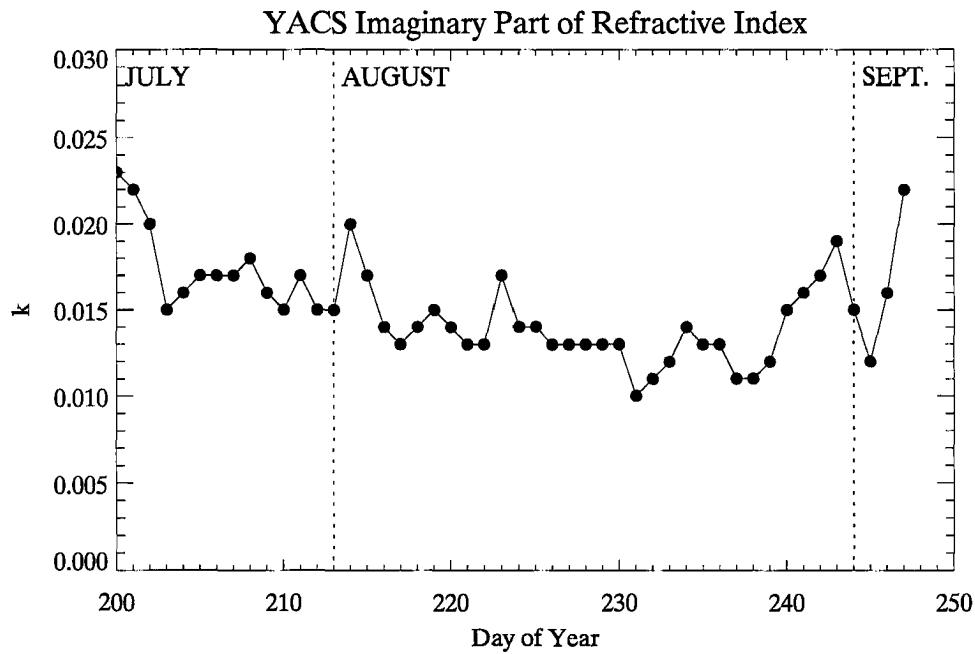
Figure 5.2 Imaginary part of refractive index computed with the assumption that elemental (black) carbon was the only absorbing species and was present predominantly in the $PM_{2.5}$ size fraction.

YACS Dry b_sp
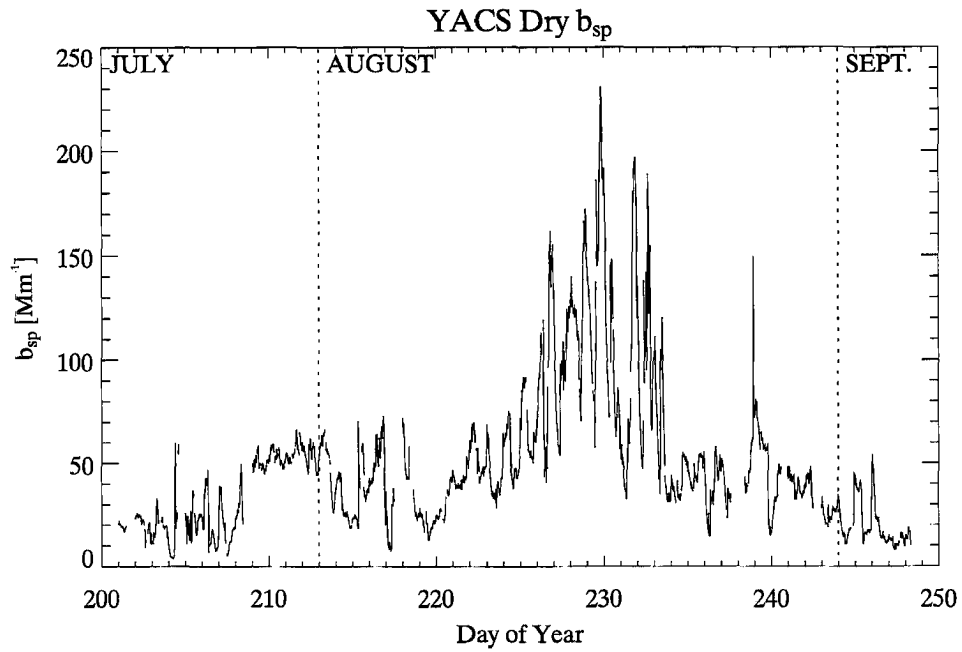
Figure 5.3 Dry calculated b_{sp} ($m = n_{ret} + k_c i$) from volume size distributions and retrieved refractive indices with imaginary component estimated from BC measurements.

YACS Total Volume and b_sp
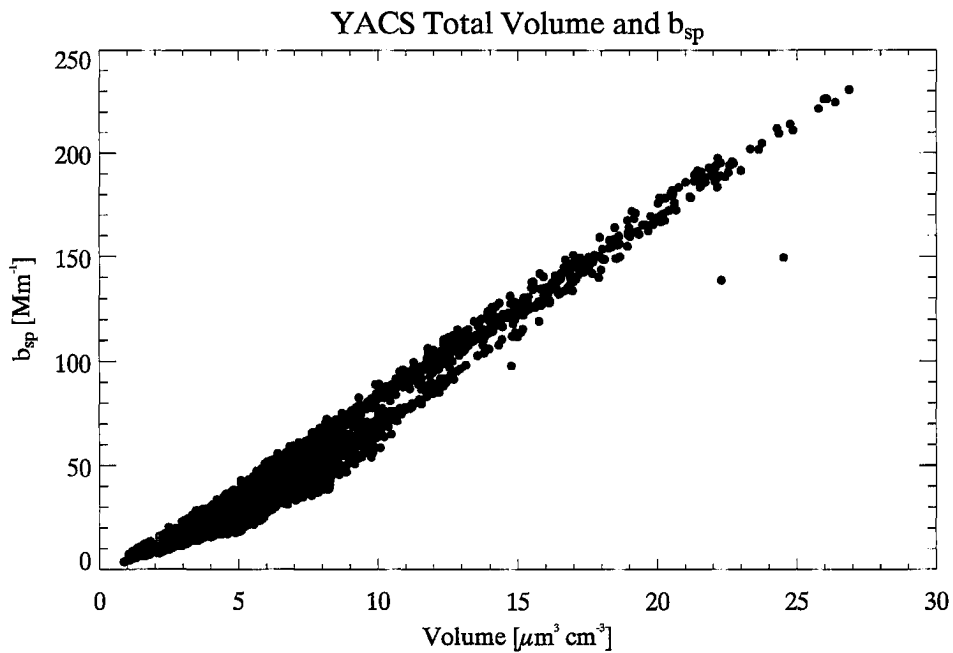
Figure 5.4 Total calculated b_{sp} ($m = n_{ret} + k_c i$) versus total integrated volume concentrations.

73
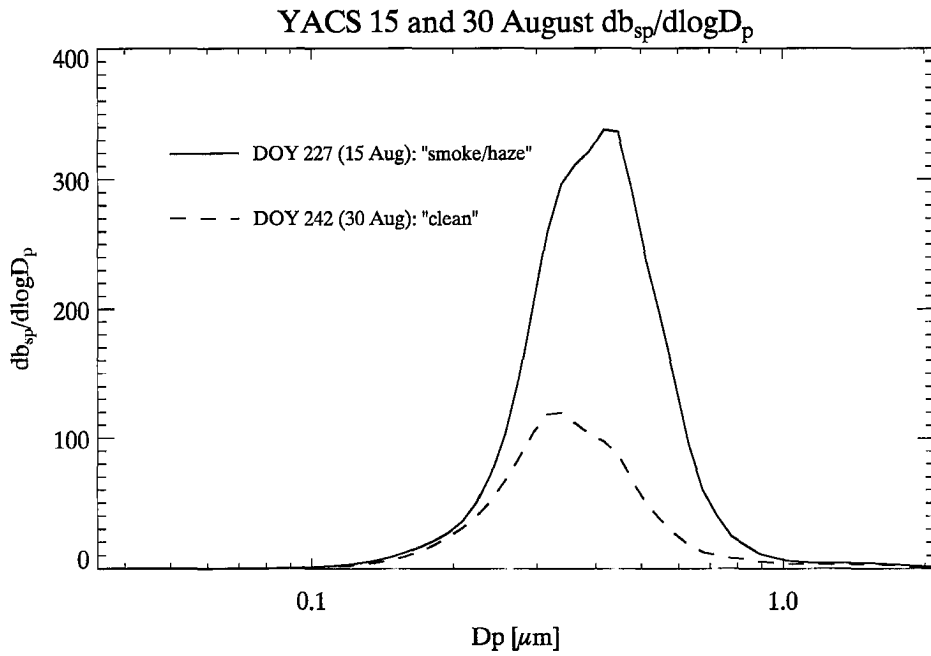
Figure 5.5 Light scattering coefficient distributions ($db_{sp}/dlogD_p$) for 15 and 30 August.
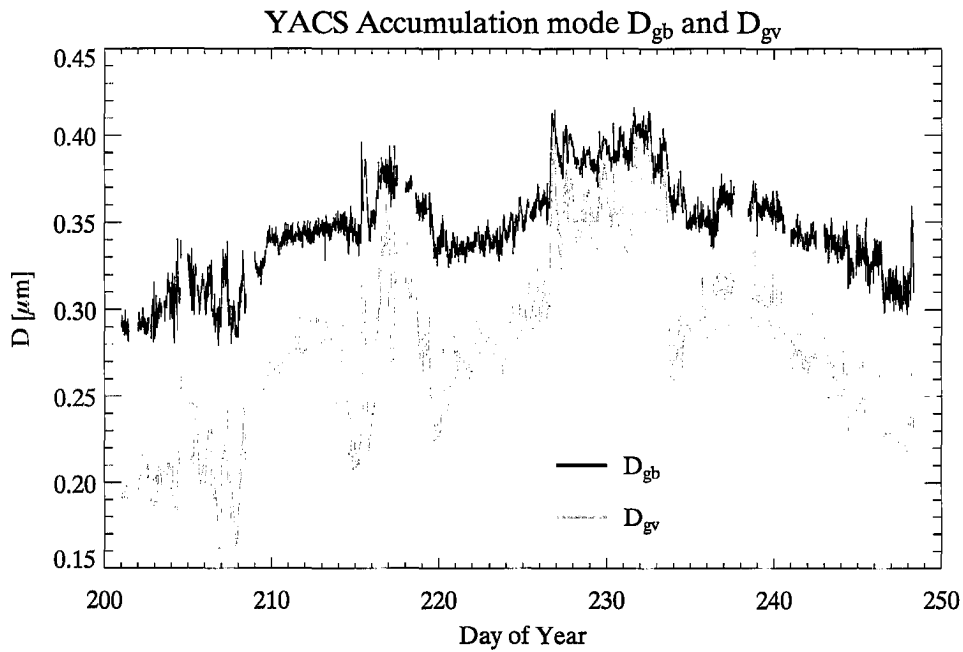
Figure 5.6 Dry accumulation mode volume geometric mean diameter (D_{gv}) and calculated light scattering geometric mean diameter (D_{gb}).
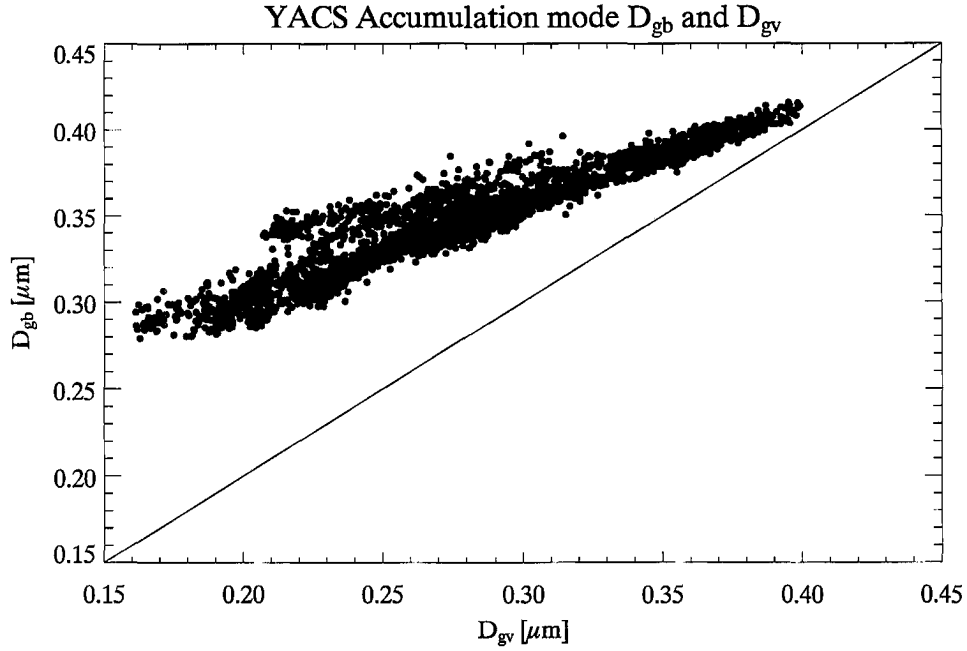
Figure 5.7 Accumulation mode volume mean geometric diameter (D_{gv}) versus light scattering geometric mean diameter (D_{gb}).
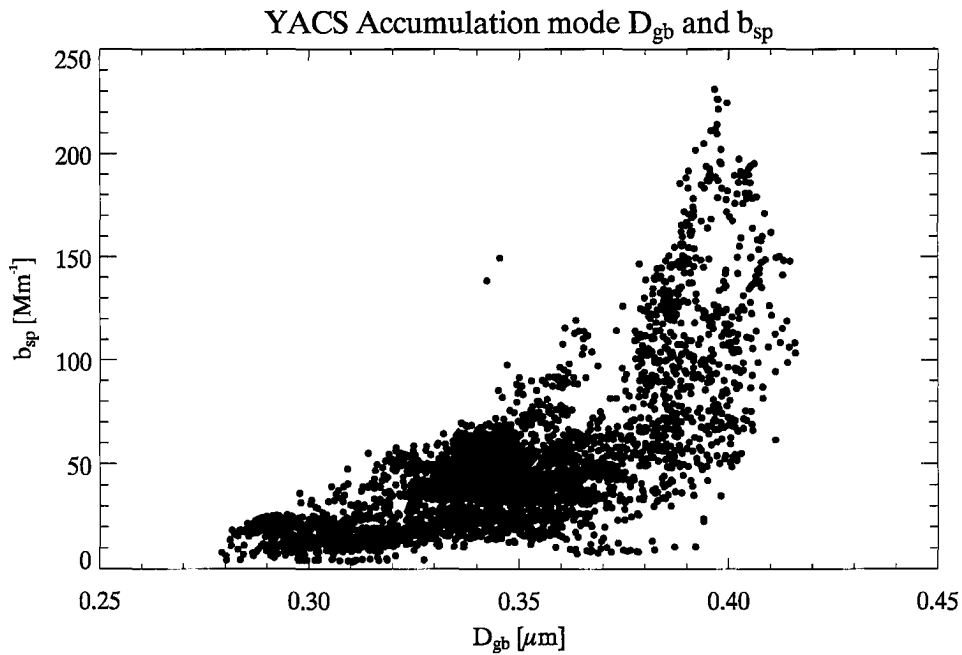
Figure 5.8 Calculated accumulation mode b_{sp} $(m = n_{ret} + k_c i)$ and accumulation mode light scattering geometric mean diameter (D_{gb}).
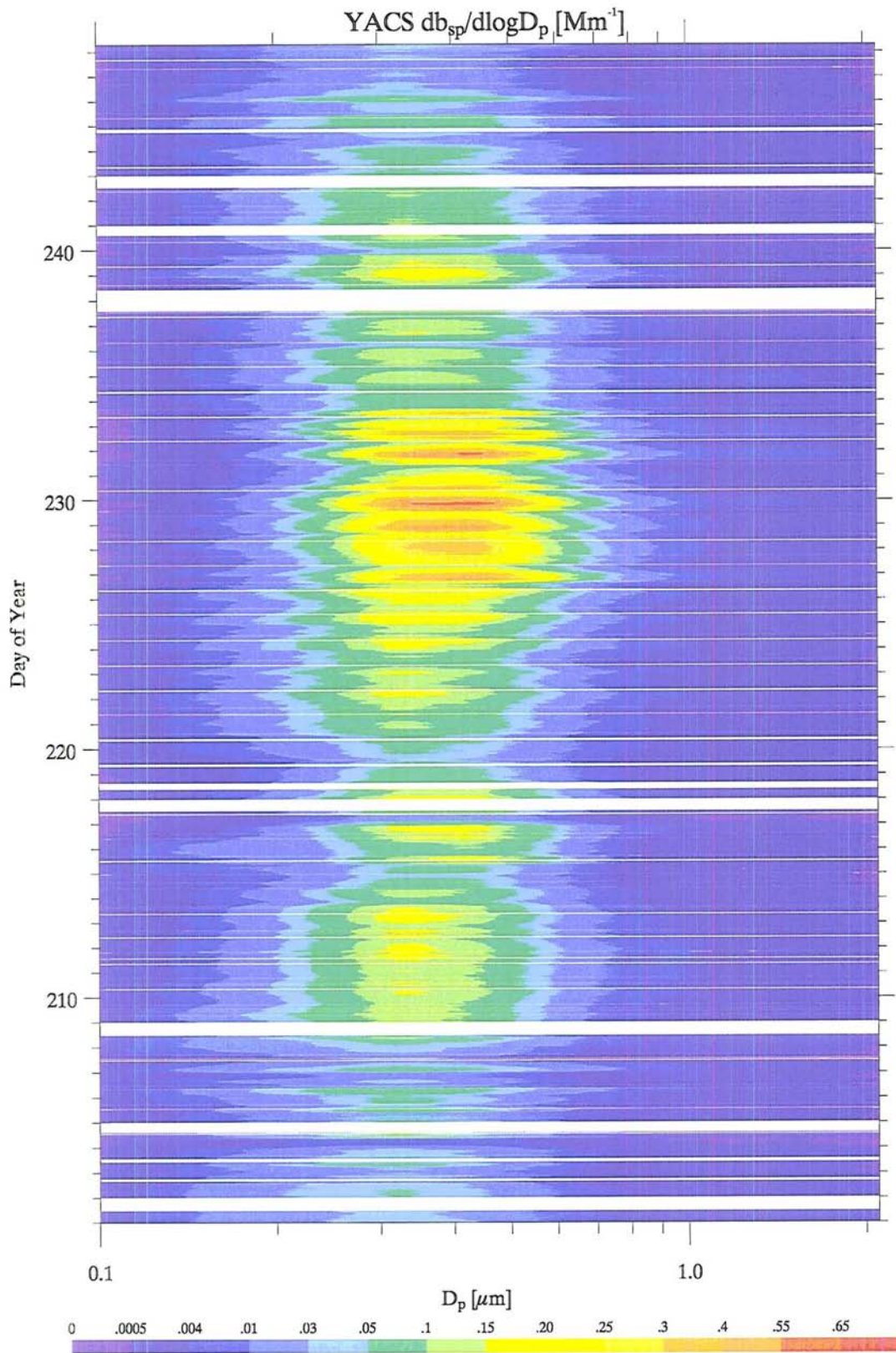
Figure 5.9 Contours of calculated ($m = n_{ret} + k_c\boldsymbol{i}$) light scattering coefficient distributions.

76
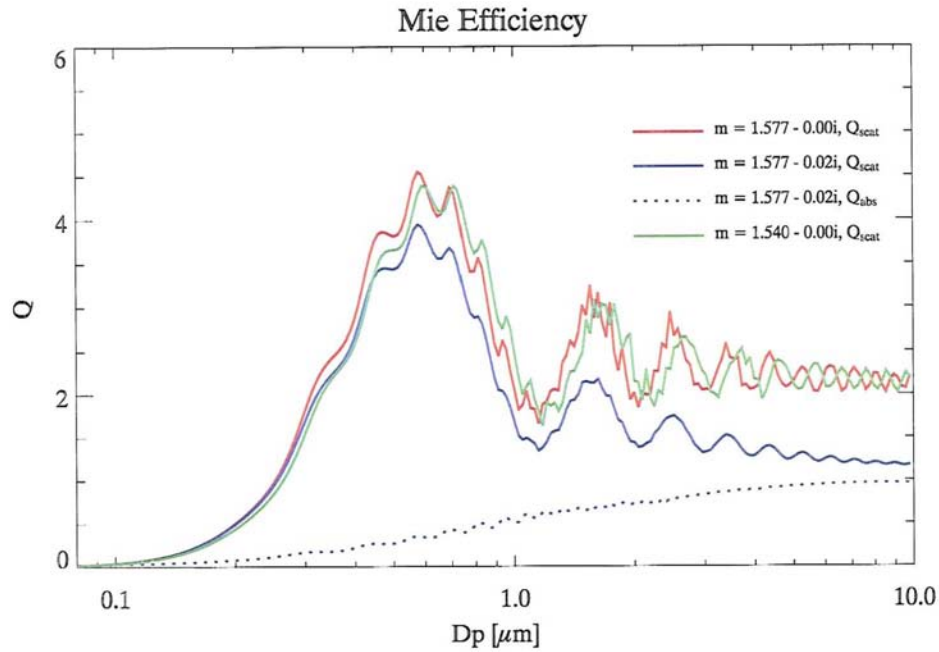
Figure 5.10 Efficiencies for extinction, scattering and absorption calculated using Mie theory for particles with complex refractive indices m = $1.57 - 0i$, m = $1.57 - 0.02i$ and m = $1.54 - 0i$ as a function of particle diameter.
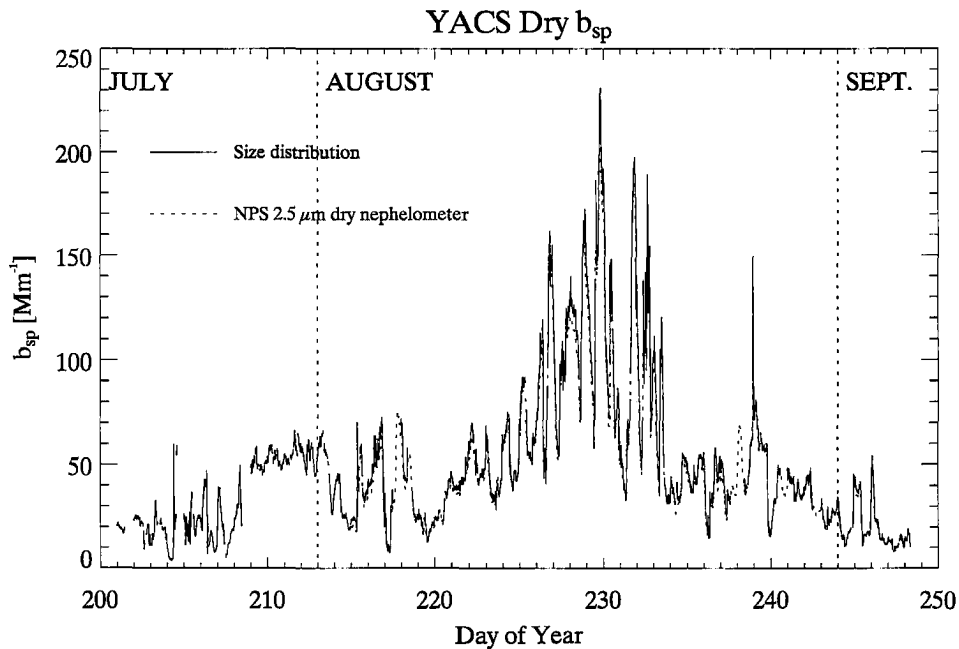
Figure 5.11 Timeline of hourly averaged dry NPS nephelometer $PM_{2.5}$ b_{sp} with calculated b_{sp} ($m = n_{ret} + k_c i$).

YACS Calculated (absorbing) and Measured b$_{sp}$
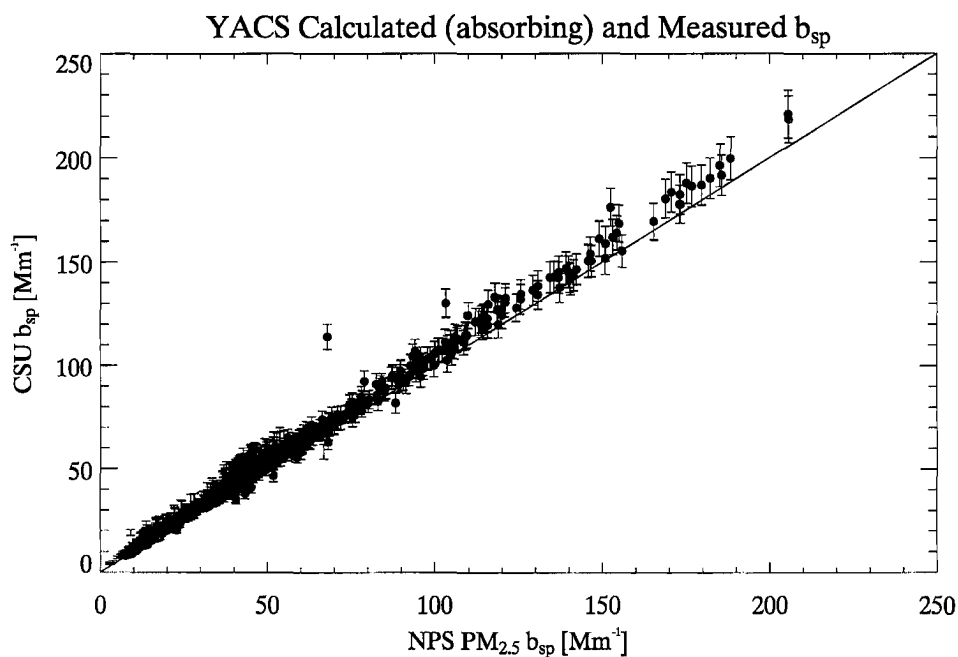
Figure 5.12 Calculated hourly averaged total b_{sp} ($m = n_{ret} + k_c i$) with uncertainties (one standard deviation; see Appendix A) versus NPS nephelometer PM$_{2.5}$ b_{sp}. The 1:1 line is also plotted.

YACS Density
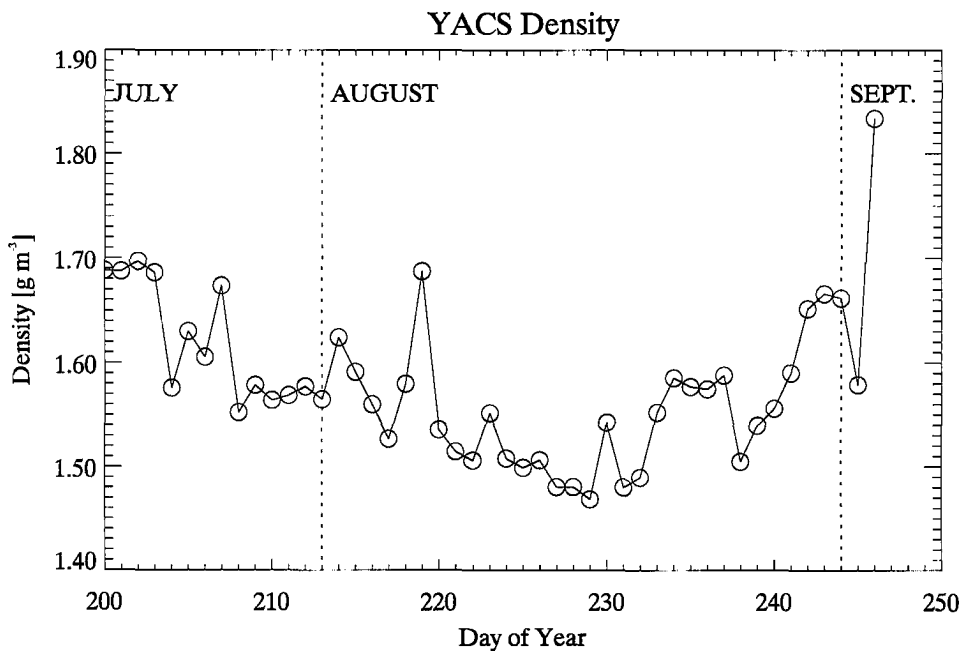
Figure 5.13 Estimates of particle density calculated from chemical compositions.
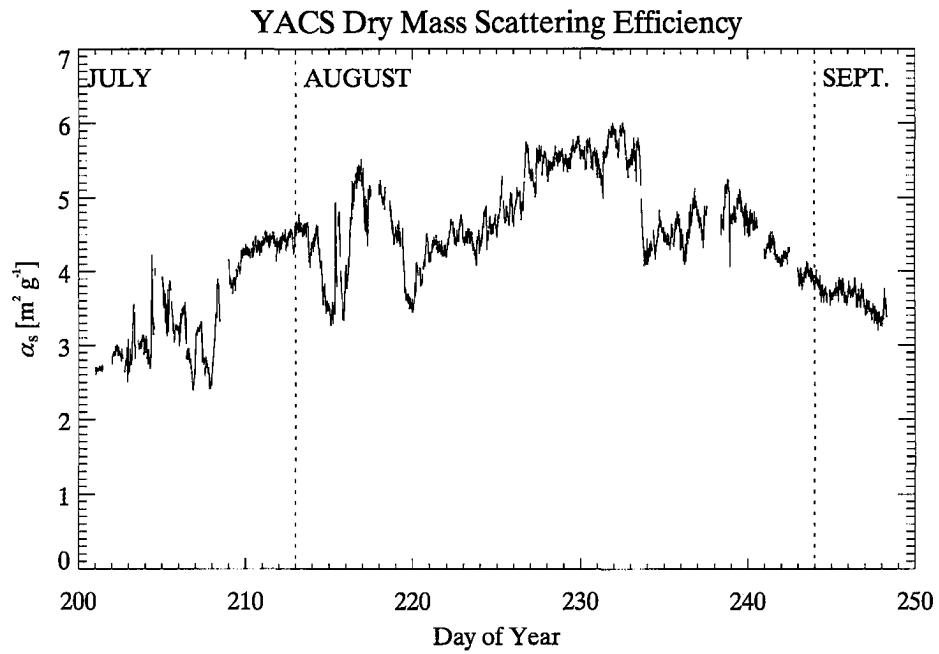
Figure 5.14 Timeline of dry mass scattering efficiencies calculated from volume distributions ($m = n_{ret} + k_c i$) assuming a density of 1.5 g cm^{-3}.

CHAPTER 6. FINDINGS

Previous chapters have presented observations and analyses of size distribution data, composition measurements and scattering calculations, and have attempted to justify the validity of the data. This chapter investigates broader issues to determine what conclusions can be made from the YACS data set. It is divided into three major subject areas which address the following issues:

- What influence, if any, does wildfire smoke have on visibility in Yosemite National Park (YNP)? Are differences in the locations of wildfires or transport pathways manifested through visibility conditions?

- What insights into the chemical, physical and optical properties of organic carbon can be gained from YACS observations? How do these measurements compare to other observations of biomass burning aerosol?

- Did the procedure for aligning size distributions obtained with different instruments introduced by *Hand and Kreidenweis* [2002] perform well for organic dominated aerosol? What improvements, if any, can be made to the method?

Each of these subjects is explored in further detail in the following sections. Particular attention is paid to effects of various assumptions made in previous chapters on final results.

6.1 SMOKE AND VISIBILITY

Characteristics of smoke-influenced haze observed at YNP will depend primarily on the production of smoke particles by fires that contribute to haze and processing of the smoke particles as they travel from the source region to the park. Wildfires are an inherently dynamic source of aerosol particles. Unlike emissions from a fixed pollution source, such as a power plant, emissions from wildfires will vary with location during the lifetime of the fire and vary on shorter time scales. The combustion process through which smoke particles are produced can be affected by factors such as humidity, temperature and fuel type [*Andreae and Merlet*, 2001]. A number of studies have observed different smoke aerosol properties for different fuel types and fire stages [*Bertschi et al.*, 2003; *Christian et al.*, 2003; *Ward et al.*, 1996]. In these cases, plumes from individual fires are sampled directly by aircraft, so the source fire characteristics are relatively well known. Back trajectory analysis (see Chapter 3), together with information about wildfire location and timing, can provide some insight into source fires, but not near the level of detail of an aircraft-based plume measurement. Analysis is further complicated by processing of the smoke particles during transport from the fire location to the measurement site. Other emissions, both natural and anthropogenic, can interact and mix with smoke particles reaching the measurement site.

Previous chapters have provided evidence for the influence of wildfire smoke at YNP during the study period. Two distinct periods (27 July – 5 August; 8 August – 23 August) were classified as having 'regional smoke/haze influence' in Table 3.1, which will be classified as Events I and II in the following discussion. Analyses described in the previous two chapters show that these two periods had markedly different physical and

optical aerosol characteristics. The first smoke/haze period (Event I) was characterized by lower scattering coefficients and mass scattering efficiencies than the second smoke/haze period (Event II). In addition, while integrated volume concentrations and b_{sp} showed large diurnal variation during Event II, this was not the case during Event I. Physical characteristics also differed between these two periods. Volume distributions had lower mean geometric diameter (D_{gv} = 0.27 ± 0.03 μm), lower integrated volume concentration (V = 7.9 ± 1.1 μm³ cm⁻³) and higher integrated number concentration (N = 3110 ± 930 cm⁻³) during Event I compared to Event II (D_{gv} = 0.32 ± 0.04 μm; V = 10.2 ± 4.6 μm³ cm⁻³; N = 1800 ± 610 cm⁻³). Composition measurements showed a higher contribution to fine aerosol composition by sulfate during the earlier smoke/haze period. The difference in absorption between the ultraviolet and visible wavelength channels measured with the aethalometer is also larger during Event II than Event I.

These differences lead to substantially different visibility during the two events. On average, scattering by aerosol particles during Event II was up to four times higher than during Event I, resulting in heavily degraded visibility. The Koschmeider equation gives the maximum range at which a typical observer can detect a contrast of 2%, which is the usually taken to be the lowest contrast value that is still perceptible during daylight viewing conditions:

$$x_v = \frac{3.912}{b_{ext}} \quad (6.1)$$

where x_v is the visual range [*Seinfeld and Pandis*, 1998]. Assuming b_{ext} is composed of only scattering by gas molecules (Rayleigh scattering; a constant ~ 10 Mm⁻¹ at YNP) and scattering and absorption by particles, visual range can be approximated with scattering coefficients calculated in the previous chapter. The particle light absorption coefficient,

b_{ap}, was calculated with the same method used to calculate b_{sp}, replacing the Mie scattering efficiency in Equation 5.2 with the Mie absorption efficiency. In general, b_{ap} was approximately equal to Rayleigh scattering (10 Mm^{-1}) and was 5-10% of the total extinction during the study. Equation 6.1 gives x_v of approximately 55 km during Event I and 18 km during Event II. Both values are low compared to x_v for a particle-free atmosphere, 390 km, and x_v during a relatively clean day at the park, 125 km.

Figure 6.1 presents contours of normalized residence times computed using the method employed in Chapter 3 for Events I (Figure 6.1a) and II (Figure 6.1b). To avoid uncertainty in defining exact beginning and ending dates for the haze events, only trajectories arriving at YNP during the middle of the events (29 July – 3 August; 10 August – 21 August) are considered. The major transport pathway during Event I consists of the movement of parcels down the coasts of British Columbia and Washington, through central Oregon, and then westward over the Sierra Nevada to reach the park. Figure 6.1b shows that the dominant transport pathway during Event II consisted of parcels traveling down the Pacific Northwest coastline, over southwestern Oregon, south over the coast of northern California and San Francisco Bay Area before reaching the site. A secondary transport path was similar to the central Oregon route seen in Figure 6.1a. Based on the back trajectory analysis, it appears that there was little influence from the Biscuit fire during the first smoke/haze event. It is possible that the smaller fires burning in central Oregon emitted fewer smoke particles, or smoke particles with different physical and chemical properties that result in the different observations made during these two periods. Another possibility is that the smoke particles emitted were similar, but interacted with different emission types and encountered different

environmental conditions along the different transport routes which resulted in different properties to be observed at the park. Different emissions into the plume along the transport path could also have had an affect. Particles seen during different episodes may also have been of different ages.

Unfortunately, the lack of a detailed transport model that can account for both large scale transport variations seen in backward trajectory analyses, as well as surface boundary layer mechanisms, severely limits the ability to explain the different smoke properties observed at the site. This work has attempted to provide some explanation of the possible influences on the smoke. Given the duration of YACS, the observations of smoke-influenced haze at YNP should represent a relatively complete spectrum of visibility conditions possible in the park during wildfire season. Observations of the properties of the smoke during these times are useful to policy makers on their own merits, though future efforts to explore the modification of smoke aerosol as it travels from the fire to a receptor site would be of interest and are discussed further in Chapter 7.

6.2 COMPARISON TO PREVIOUSLY-REPORTED RESULTS

The optical properties of biomass burning aerosol have been measured in a variety of locations using many different techniques. Uncertainties and assumptions used by the different techniques complicate efforts to verify the validity of new observations and tease out physical variations in the properties of biomass burning arising from natural differences in fire fuel sources, transport mechanisms and climate. This section compares YACS findings to results reported in the literature for fires in a number of tropical and extra-tropical locations. The focus is on observations of regional hazes similar to those

observed during YACS as opposed to properties of fresh emissions from biomass burning.

Table 6.1 gives previously observed mass scattering efficiencies (α_s) and estimated complex indices of refraction for aged biomass burning hazes. *Formenti et al.* [2003] determined α_s to be 4.6 ± 0.8 m^2 g^{-1} for aged smoke hazes off the coast of Namibia in southern Africa using aircraft-based nephelometer measurements (λ = 550 nm) of the dry scattering coefficient and mass reconstructed from submicron aerosol composition measurements using a varying OM/OC ratio based on other measurements. *Haywood et al.* [2003] estimated α_s of 4.6 ± 0.5 m^2 g^{-1} by applying Mie theory (λ = 550 nm) to size distributions (0.1 < D_p < 3.0 µm) measured on the same aircraft. The refractive index used in the Mie calculations was m = 1.54 − 0.018i and was estimated from measurements of aerosol composition assuming an EC density of 1.7 g cm^{-3} and an aerosol density of 1.35 g cm^{-3}. *Reid et al.* [1998] conducted aircraft-based measurements of particle size distributions, composition and scattering properties (0.01 < D_p < 4 µm) for biomass burning hazes over Brazil. Size distribution measurements showed trends of increasing particle size and decreasing standard deviations with increasing smoke age. Measurements of aged smoke hazes were found to have volume median diameters on the order of 0.35 µm and σ_{gv} of 1.5, similar to results for smoke-impacted aerosol sampled during YACS. Filters were gravimetrically analyzed in a humidity-controlled chamber (RH = 35%) to determine aerosol mass concentration. Nephelometer measurements were used to determine scattering coefficient (λ = 550 nm) for aerosols dried to RH < 35%. Mass scattering efficiencies of aerosols sampled in a region thought to contain smoke on the order of 2-4 days old were 3.8 ± 0.8 m^2 g^{-1} and were higher (4.1 ± 0.9 m^2 g^{-1}) if soil

was removed in the calculations. *Reid et al.* [1998] also showed that α_s increased as the smoke haze aged due to particle growth through condensation and coagulation mechanisms.

The amount of water present on smoke/haze particles sampled during YACS was lower than during the studies listed above because of the lower ambient relative humidity and drying of the particles during sampling. As water has a much lower density (1.0 g cm^{-3}) and refractive index ($m = 1.33 - 0i$) than the other species likely to be present in biomass burning aerosol, it can significantly reduce the density and refractive index of these particles. Though the hygroscopicity of smoke particles is thought to be low [*Carrico et al.*, submitted], relative humidity can be high in the tropics, causing some water uptake by the smoke particles. This effect may explain some of the differences between YACS mass scattering efficiencies and those reported by *Haywood et al.* [2003] and *Formenti et al.* [2003] for African biomass burning hazes. It is more difficult to account for the difference between YACS α_s and those reported by *Reid et al.* [1998] for aged hazes in Brazil, as aerosol in their work, was dried to RH < 35%. This is a higher sample RH than used during YACS, but is still low enough that it is not likely that a significant amount of water was present on the smoke particles. Another possibility is that hazes sampled by *Reid et al.* [1998] were younger than those sampled during YACS. *Reid et al.* [1998] found that the mass scattering efficiency of biomass burning aerosol increased up to 30% as it aged. Biomass burning aerosol could have accumulated in the San Joaquin Valley during the major haze episode in mid-August. Figure 5.14 shows α_s increasing during the period DOY 221–226 (9 – 14 August) before reaching a maximum value of approximately 5.5 m^2 g^{-1}. Mass scattering efficiencies at the beginning of this

86

increase are close to the values reported by *Reid et al.* [1998]. The increasing values of α_s could be explained by further aging (i.e., increase in size and narrowing of number distribution) of haze that is trapped in the valley to some maximum value. The larger D_{gv} observed during this time supports this older particle hypothesis and the age of the smoke sampled at Turtleback Dome could be verified through a modeling study to better determine transport mechanisms of the complex mountain valley system.

Yamasoe et al. [1998] retrieved an 'effective' real part of the complex refractive index of n = 1.533 ± 0.035 (λ = 438 nm) and m = 1.553 ± 0.036 (λ = 670 nm) for aged biomass burning hazes in Brazil using Sun/sky radiometer measurements. *Colarco et al.* [2004] report values of m = 1.524 − 0.0056i (λ = 440 nm) and m = 1.554 − 0.0043i (λ = 670 nm) using a similar technique for a single measurement of an aged smoke plume over Washington D.C. thought to have originated over eastern Canada. Measurement of the complex refractive index at 550 nm, the wavelength assumed for YACS scattering calculations, was not available because the instruments do not operate at that wavelength, though the values are reported at wavelengths that bracket the YACS value. Refractive indices retrieved during YACS are higher than these values. Some of the difference between YACS and the literature values can be explained by the likely presence of water on smoke haze aerosols observed by the radiometer, which would cause the 'effective' refractive index to be lower than for dried smoke particles. *Wandinger et al.* [2002] inverted LIDAR measurements of highly aged (~ 6 days) biomass burning smoke haze from Canadian fires over Europe to retrieve the real and imaginary components of the refractive index. Higher values were found, on the order of m = 1.65, than reported previously in the literature and this study. *Wandinger et al.* [2002] cite differences in

humidity and the presence of iron oxide as the most likely reasons for the higher values, and noted that decreasing relative humidity was correlated with higher retrieved refractive index values. It should be noted the retrieved LIDAR refractive indices in their study could not be reconciled with values of refractive index determined with simultaneous *in situ* composition measurements. This calculation assumed an internal mixture of absorbing, soot-like and nonabsorbing, ammonium-sulfate-like material and is suggested by the authors to be used only as a very rough estimate of refractive index.

6.3 IMPLICATIONS FOR ORGANIC CARBON PROPERTIES

As mentioned earlier, the properties of organic carbon are not well known, primarily due to the lack of adequate speciation of the organic compounds present. The properties of OC relevant to this study are density, refractive index and organic mass (OM) to OC ratio. Varying the values assumed for these three properties will affect the refractive index and density used in mass and scattering calculations significantly due to the dominance of organic carbon on aerosol composition observed during the study. For example, reducing the density of OC from 1.4 g cm^{-3}, the value commonly cited in the literature, to 1.2 g cm^{-3}, the value suggested by *Turpin and Lim* [2001], reduced the average $PM_{2.5}$ density from 1.57 g cm^{-3} to 1.40 g cm^{-3}. The average computed refractive index decreases slightly as well, from 1.569 to 1.567, because the volume weighted refractive index calculation depends on assumed densities. The computed refractive index is also highly sensitive to the value assumed for the refractive index of organic carbon. The OM/OC ratio affects $PM_{2.5}$ density and refractive index by controlling the mass fraction of OM in the calculations. Higher OM/OC ratios would cause a larger

contribution from OC, while lower OM/OC ratios would lead to a smaller contribution. The choice of OC and EC data sources complicates matters, as at times concentrations from the different measurements did not agree within a reasonable factor, though recent results after artifact correction suggest better confidence in IMPROVE OC and EC values [J. Collett, personal communication].

Figures 6.2, 6.3, and 6.4 show measured gravimetric mass and mass calculated using different density assumptions. Good agreement can be seen between gravimetric mass and mass assuming a constant particle density of 1.5 g cm^{-3} (Figure 6.2) and assuming densities calculated from composition measurements using an OC density of 1.4 g cm^{-3} (Figure 6.3). Applying an OC density of 1.2 g cm^{-3} (Figure 6.4) requires a larger OM/OC ratio to maintain mass closure, suggesting the OM/OC ratio may be closer to the value of 2.3 suggested by *Turpin and Lim* [2001] for OC in remote regions. Many different combinations of assumed OC density and OM/OC ratio are possible to maintain mass closure using this method. Both the reduction of the OC density and the increase of the OM/OC ratio lead to higher weighting of the assumed OC refractive index in the calculation of the PM$_{2.5}$ refractive index. As a result, the assumed OC refractive index is extremely important to the final result. Results from this study suggest that the OC refractive index should be slightly larger, on the order of 1.57 as opposed to 1.55, to reach agreement with retrieved values. This increase is not dramatically different from previously applied values, and may be reasonable considering the 1.55 estimate originated from studies pertaining to urban OC, which may be substantially different in composition from OC from smoke and biogenic sources. Obtaining a new estimate for the OC refractive index was not the primary aim of this study. As a result, a number of

factors, such as the measurement technique used to determine OC concentrations and the treatment of soil in reconstructing the refractive index, complicate efforts to make a robust estimation. A study designed to eliminate these uncertainties could provide a much better application of this interesting new application of the alignment method.

6.4 VALIDATION OF ALIGNMENT METHOD

A minor goal of this study was to apply the alignment method developed by *Hand and Kreidenweis* [2002] to a region with substantially different aerosol composition than that of the original application during the Big Bend Regional Aerosol and Visibility Observation study (BRAVO). Carbon, as opposed to sulfate, was much more important at Yosemite National Park than it was at Big Bend National Park (BBNP). Scattering coefficients estimated using aligned size distributions, retrieved real part of the complex index of refraction, and reconstructed complex part of the refractive index agreed with measured scattering coefficients within experimental uncertainty, though a small bias was still present. Better agreement was found between estimated and measured scattering during YACS than during BRAVO, though it is not known if this represents improvement in the alignment method or better nephelometer calibrations. The retrieved refractive indices for aerosol particles were slightly higher than reconstructed values and values previously reported in the literature for biomass burning aerosol, but given the uncertainty in the properties of organic carbon, its dominance during YACS and differences in the natural conditions during YACS and previous studies, there is no reason to believe the alignment method performed poorly.

The usefulness of the alignment method during YACS is somewhat mixed. Higher concentrations of super-micron particles were observed during the BRAVO and these particles played a more important role in total scattering. Adequate characterization of these particles was therefore crucial. There were substantially fewer particles in the size range $0.85 < Dp < 2.1$ µm during YACS. Total failure of the alignment method would have only a small effect on retrieved aerosol physical properties, as data from the differential mobility analyzer are fairly representative of total fine particle size distributions. Determination of optical properties depends greatly on the assumed refractive index, however. This fact, combined with the ease and relatively low increase in expense required by the addition of the optical particle counter to the sizing measurement setup, suggests inclusion of the alignment method in future measurements of aerosol size distributions in other carbon dominated locations is justified.

Table 6.1 Mass scattering efficiency and refractive index for biomass burning aerosol measured in several different locations.

LOCATION	PLATFORM	α_s [m^2 g^{-1}]	$M = n + ki$ (λ)
Western United States[1]	Ground	5.5 ± 0.5 (estimate)	1.57 − 0.02i
Southern Africa[2]	Aircraft	4.6 ± 0.6	-
Southern Africa[3]	Aircraft	4.6 ± 0.5	1.54 − 0.018i
Brazil[4]	Aircraft	4.1 ± 0.9	-
Brazil[5]	Ground (radiometer)	-	1.533 ± 0.035 (438) 1.553 ± 0.036 (670)
Northern Europe[6]	Ground and aircraft (LIDAR)	-	1.64 ± 0.09 − 0.05i ± 0.02i
Eastern United States[7]	Ground (radiometer)	-	1.524 − 0.0056i (440) 1.554 − 0.0043i (670)

[1] this study
[2] *Formenti et al.* [2003]
[3] *Haywood et al.* [2003]
[4] *Reid et al.* [1998]
[5] *Yamasoe et al.* [1998]
[6] *Wandinger et al.* [2002]
[7] *Colarco et al.* [2004]
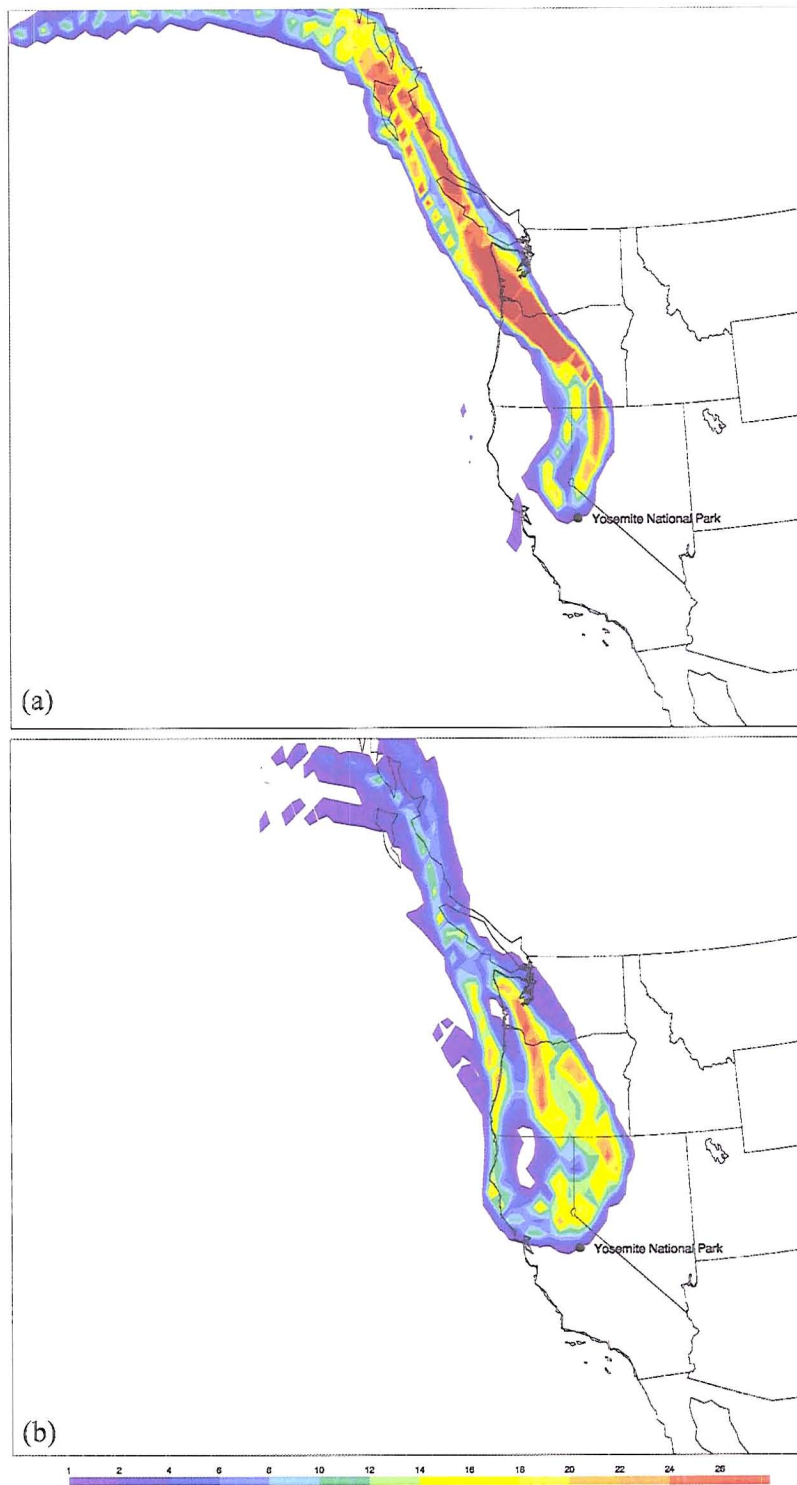
Figure 6.1 Source contribution function contours for Event I (a) (27 July through 5 August) and Event II (b) (8 August through 23 August).

YACS Fine Gravimetric Mass and Calculated Mass
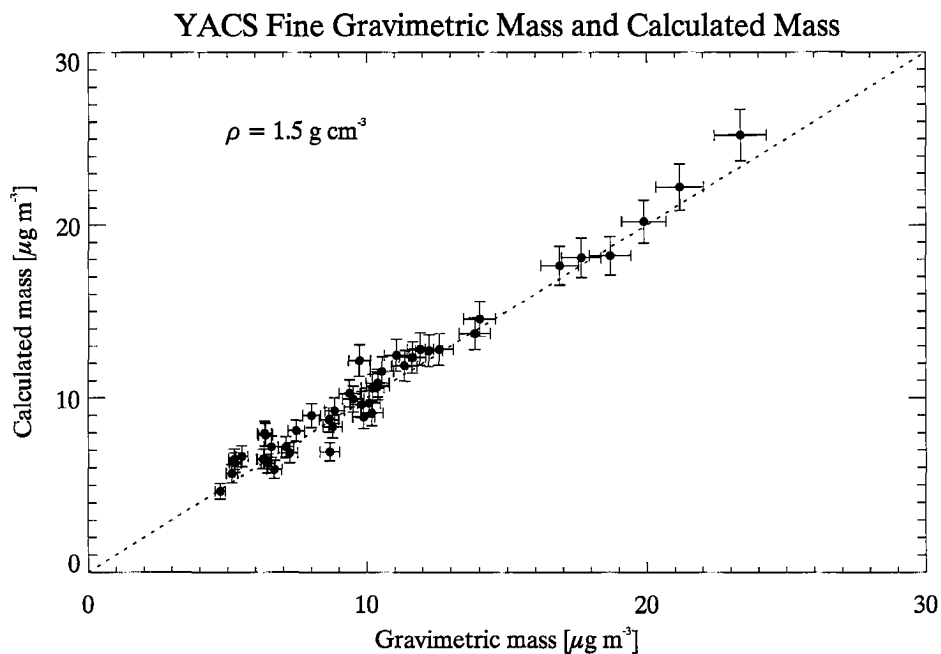
Figure 6.2 YACS gravimetric mass and mass calculated from integrated volume concentrations and assuming a constant particle density of 1.5 g cm^{-3}. Error bars represent one standard deviation.

YACS Fine Gravimetric Mass and Calculated Mass
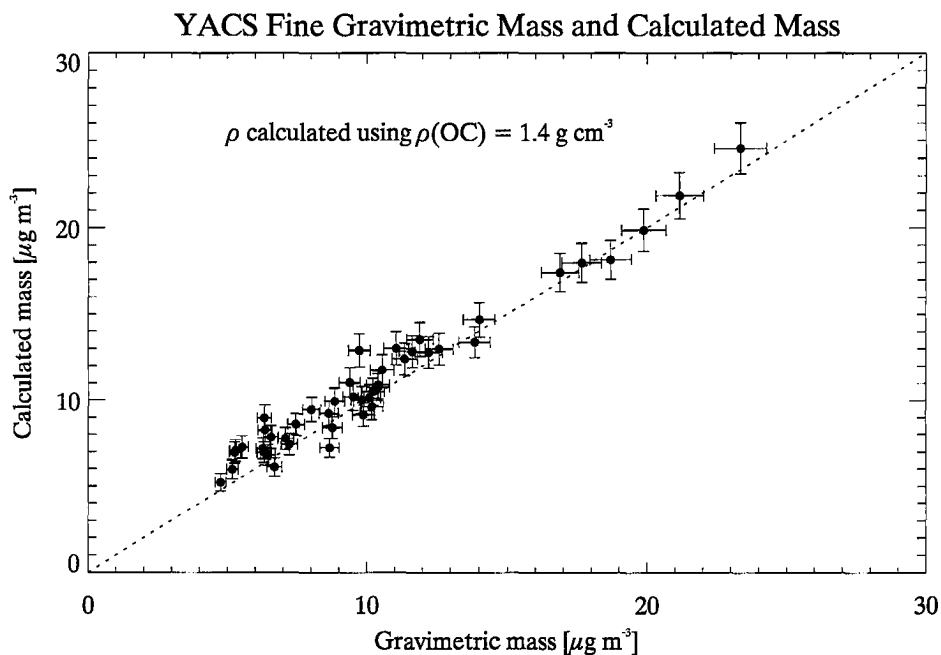
Figure 6.3 YACS gravimetric mass and mass calculated from integrated volume concentrations and density calculated from composition measurements. A density of 1.4 g cm^{-3} is assumed for organic carbon (OC) and the organic matter to OC ratio is 1.8. Error bars represent one standard deviation.

YACS Fine Gravimetric Mass and Calculated Mass

ρ calculated using $\rho(OC) = 1.2$ g cm^{-3}
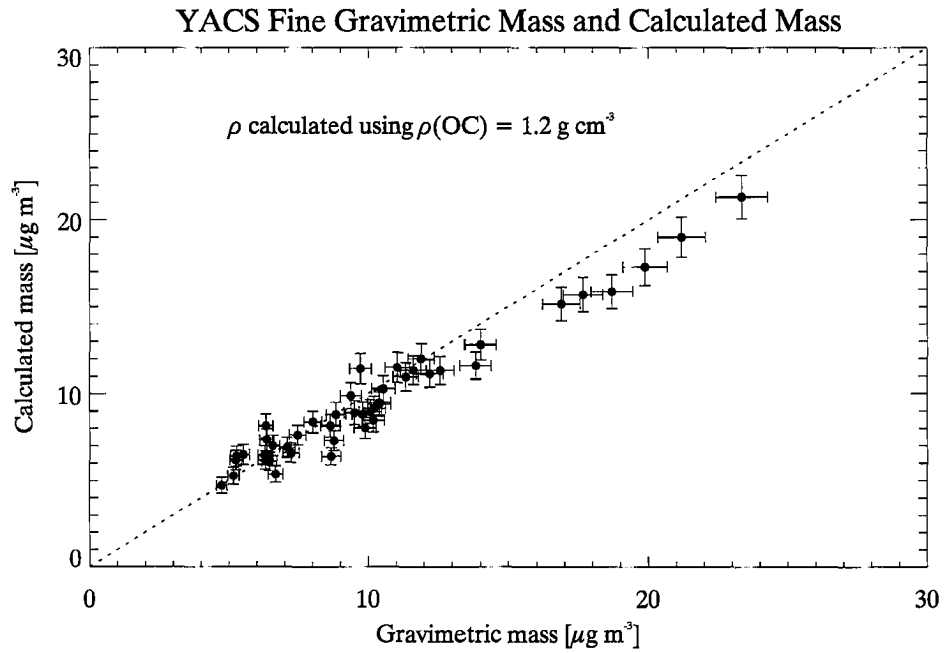
Figure 6.4 YACS gravimetric mass and mass calculated from integrated volume concentrations and density calculated from composition measurements. A density of 1.2 g cm^{-3} is assumed for organic carbon (OC) and the organic matter to OC ratio is 1.8. Error bars represent one standard deviation.

CHAPTER 7. SUMMARY AND FUTURE WORK

7.1 SUMMARY

Several very large wildfires and numerous smaller fires occurred during YACS and smoke from these fires was observed at Yosemite National Park. Meteorological conditions suggested that fires burning in Oregon had the biggest impact on air quality in the park based on backward trajectory analyses. Very little variation was seen in wind patterns during the study, with only occasional transport from the south and west, and almost no transport from the east of the park. Smoke-impacted haze episodes lasting several days occurred in late July and mid August. YACS allowed for investigation of the chemical, physical and optical properties of this aged biomass burning haze and its contribution to visibility in the park. Local fires occurred during the study, but smoke from these fires was difficult to separate from aged smoke during times when both influenced the site. Smoke episodes were linked to elevated particle volume concentrations and an increase in the mean particle size.

Dry aerosol size distributions were measured using two instruments with different measurement ranges and techniques. A TSI Differential Mobility Analyzer (DMA) measured mobility diameter for the size range $0.038 < D_p < 0.85$ μm and a PMS Optical Particle Counter (OPC) measured optical size from 0.1 μm to 2.1 μm. Failure of the dried OPC required use of data from an OPC sampling ambient aerosol, though low particle hygroscopicity and very low instrument relative humidity suggested that no bias was introduced by this necessity. Extensive calibrations were performed for the dried OPC,

but not for the ambient OPC. Calibration results performed for the dried OPC were very similar to those determined for a previous study, thus results from those calibrations were used and assumed to be valid. The alignment method introduced by *Hand and Kreidenweis* [2002] was used to reconcile data in the overlap region between the two instruments to produce a complete size distribution from 0.04 to 2.1 μm and retrieve a particle refractive index. The average retrieved refractive index was 1.577 ± 0.008.

Fine (PM$_{2.5}$) aerosol chemical composition data were obtained from 24-hour filter samples, continuous measurements of carbonaceous aerosol, and continuous measurements of water soluble ion concentrations. Organics were the dominant contributor to fine mass, making up 65 ± 15% of the total concentration on average. Organics contributed up to 85% of the fine mass during smoke haze episodes. Sulfate and ammonia were the most important ionic species, combing to contribute 20 ± 11% of the fine mass concentration. The average ammonium to sulfate molar ratio was 2.04 ± 0.19, suggesting aerosol particles were neutral during most of the study. Soil made up 6.9 ± 3.1%, sodium nitrate 4.3 ± 3.5%, elemental carbon 2.9 ± 0.5% and ammonium nitrate 1.3 ± 1.6% of the fine mass concentration.

Continuous measurements of water-soluble potassium ion (K^{+}) and the difference in measured absorption of black carbon between two wavelengths were used to identify smoke aerosol during the study. In addition, concentrations of certain organic wood smoke tracers such as levoglucosan and vanillin were determined from filter samples. Backward trajectory analysis was also used to determine transport pathways from fire regions to the park. These data were used to help define smoke-impacted periods at the park.

Composition data were used to compute complex refractive index and bulk densities using volume-weighted mixing rules. The overall average real part of the complex refractive index was 1.570 ± 0.006, in good agreement with retrieved values, and the imaginary part was 0.015 ± 0.003. The average bulk density was 1.58 ± 0.09 g cm^{-3} and was highly dependent on the density assumed for organic carbon (OC) (ρ_{OC} = 1.4 g cm^{-3}).

Size distribution measurements showed that volume concentrations increased significantly during smoke haze episodes. Size parameters derived from aerosol size distributions showed that particles were larger during smoke haze episodes than during other times and had narrower distributions. High number concentrations of sub-100 nm particles were observed at night just after winds shifted to down-valley flow on most days, particularly during the first two weeks of the study. These events were associated with increased sulfate to carbon ratio and may reflect the presence of aerosol transport from the free troposphere. Few particles were observed at sizes greater than 1 μm, though the small upper size limit (~ 2 μm) of the measurements presented in this work complicates conclusions being drawn about the contribution of coarse mode particles during YACS.

Measured volume distributions, retrieved real components of the complex index of refraction and calculated imaginary components were used to determine dry light scattering coefficients. The average total dry light scattering coefficient was 49 ± 36 Mm^{-1}. Highest calculated values were on the order of 200 Mm^{-1} and occurred during a smoke haze episode. Periods identified as smoke influenced (through chemical analyses) typically had elevated light scattering coefficients, though the magnitudes varied

considerably over the study. Lowest values approached Rayleigh scattering and were linked to rapid transport from marine environments. Particles less than 1 μm in size had the largest contributions to scattering. Comparisons of calculated light scattering coefficients to nephelometer measurements of dry $PM_{2.5}$ scattering coefficients were highly correlated and agreed within the experimental uncertainty, though a slight bias appeared to be present. This bias may be due to a number of assumptions, including magnitude of loss corrections in the aerosol sizing instrumentation and the nephelometer and assumptions involved in calculation of the imaginary part of the complex index of refraction.

Dry mass scattering efficiencies were calculated using estimated light scattering coefficients and mass concentrations derived from applying an assumed density to integrated volume concentrations. The assumed density, 1.5 g cm^{-3}, gave best agreement between calculated mass and gravimetric mass measured from filter samples. Calculations were performed with varying density that showed no substantial improvement The average mass scattering efficiency was 4.3 ± 0.8 m^2 g^{-1}, near the value for OC (4 m^2 g^{-1}) applied in the IMPROVE formula. Replacing the constant density used in the calculation with densities calculated from composition measurements had a small effect, but density calculations were highly sensitive to assumptions about OC properties. When a combination of ρ_{OC} = 1.4 g cm^{-3} and a organic mass to carbon mass ratio of 1.9 was used to determine densities used for mass calculations, gave good agreement was found with measured mass, though other combinations could be found. Values of mass scattering efficiency approached 6 m^2 g^{-1} during smoke haze episodes when OC was more dominant. This is substantially higher than the value applied in the IMPROVE

formula. Mass scattering efficiencies during the beginning and end of the study when sulfate played a more important role were close to the value of 3 m^2 g^{-1} used for non-soil, non-carbon species in the IMPROVE formula.

Results presented in Chapters 4 and 5 suggest that the alignment method performed well during YACS. Better agreement was observed between calculated and measured light scattering during YACS than during the method's original application, though this fact does not necessarily prove the validity of the method. Reasonable estimates of the various OC properties can produce refractive indices matching those produced by the alignment. This should not be taken as a definitive validation of the alignment, however, given wide range of reasonable refractive indices that can be assumed for OC. In addition, estimates of scattering coefficients, mass concentrations and other aerosol properties derived through other methods are also sensitive to assumptions involving OC. Comparison between these methods and the results presented in this work should be viewed with this in mind.

7.2 FUTURE WORK

The large number of observations during YACS has allowed for a number of analyses of observed aerosol properties and provide ample opportunity for future investigations. The good agreement found between measured and calculated light scattering coefficients suggest that fine aerosol physical properties are relatively well understood. Incorporation of time of flight measurements made using a TSI Aerodynamic Particle Sizer (APS) would add aerosol size information for particles in the size range 0.7 < D_p < 20 μm and would allow for retrieval of an effective density. This would provide

more information about the importance of coarse particles to total scattering during smoke haze periods and other times. Effective densities would allow for better evaluation of the alignment method by providing another variable for comparison with estimates from composition measurements. More accurate determination of calculated aerosol mass and mass scattering efficiency would also be possible.

The difficulties encountered in determining transport effects on smoke aerosol measured at the site were considerable, due mostly to uncertainties involving transport mechanisms operating in the park and surrounding areas. One major question involves the role of the San Joaquin Valley, and whether its large anthropogenic and agricultural emissions play a significant role in modifying smoke aerosol before it reaches the park. A modeling study could provide a great deal more insight into the transport mechanisms operating in the region than the limited backward trajectory analyses described in Chapter 3 can provide. More information regarding regional scale processes involving smoke could be gained through incorporation of observations from other measurement sites. The National Oceanographic and Atmospheric Administration (NOAA) carried out measurements of aerosol properties on the coast of northern California, located 50 km south of the Oregon-California border. The University of California, Berkeley and Lawrence Berkeley Laboratory conducted measurements of trace gasses and aerosols at Blodgett Forest Research Station, located roughly 150 km north of YNP. Other IMPROVE network sampling sites also carried out standard measurements during the study. Future work is planned that will examine regional trends in aerosol properties and influences of biogenic aerosols using data from all three sites.

One topic of future work suggested in *Hand* [2001] was testing the alignment method's performance in a region with significant fraction of light absorbing aerosol. It was thought that smoke would provide a good test due to high black carbon concentrations. High BC concentrations were not observed in Yosemite. As a result, the absorbing fraction of the aerosol was not significantly higher than seen during BRAVO. Thus, determination of alignment performance in a region of high BC content remains a useful area of future research. Other questions posed by *Hand* [2001], such as the performance of the alignment in regions where aerosol properties may not be constant over the tested size range and effects of water uptake, remain topics for future research.

Other questions that were raised during the processing and analyses presented in this work are more general. It would be interesting to attempt to use the alignment method to determine properties of OC in different regions in order to test the validity of the typically assumed refractive index and density of OC. Results from YACS indicate that OC properties in remote areas under heavy smoke influence are quite different from those determined and assumed for other areas, especially so for urban regions. Also of considerable interest is the wavelength dependence of the refractive index of various aerosol species. Alignments using data from OPCs operating at different wavelengths could provide useful information.

REFERENCES

Abel, S.J., J.M. Haywood, E.J. Highwood, J. Li, and P.R. Buseck, Evolution of biomass burning aerosol properties from an agricultural fire in southern Africa, *Geophysical Research Letters*, *30* (15), 2003.

Allen, M.D., and O.G. Raabe, Slip Correction Measurements of Spherical Solid Aerosol-Particles in an Improved Millikan Apparatus, *Aerosol Science and Technology*, *4* (3), 269-286, 1985.

Andreae, M.O., and P.J. Crutzen, Atmospheric Aerosols: Biogeochemical Sources and Role in Atmospheric Chemistry, *Science*, *276* (5315), 1052-1058, 1997.

Andreae, M.O., and P. Merlet, Emissions of trace gases and aerosols from biomass burning, *Global Biogeochemical Cycles*, 2001.

Ashbaugh, L.L., W.C. Malm, and W.Z. Sadeh, A Residence Time Probability Analysis of Sulfur Concentrations at Grand-Canyon-National-Park, *Atmospheric Environment*, *19* (8), 1263-1270, 1985.

Baron, P.A., and K. Willeke, Aerosol measurement: principles, techniques and applications, Wiley-Interscience, New York, 2001.

Bertschi, I., R.J. Yokelson, D.E. Ward, R.E. Babbitt, R.A. Susott, J.G. Goode, and W.M. Hao, Trace gas and particle emissions from fires in large diameter and belowground biomass fuels, *Journal of Geophysical Research-Atmospheres*, *108* (D13), 2003.

Bevington, P., and D. Robinson, *Data Reduction and Error Analysis for the Physical Sciences*, McGraw-Hill, Inc., New York, 1992.

Chow, J.C., J.G. Watson, L.C. Pritchett, W.R. Pierson, C.A. Frazier, and R.G. Purcell, The DRI thermal/optical reflectance carbon analysis system: Description, evaluation and applications in U. S. air quality studies, *Atmos. Environ.*, *27A* (8), 1185-1201, 1993.

Christian, T.J., B. Kleiss, R.J. Yokelson, R. Holzinger, P.J. Crutzen, W.M. Hao, B.H. Saharjo, and D.E. Ward, Comprehensive laboratory measurements of biomass-burning emissions: 1. Emissions from Indonesian, African, and other fuels, *Journal of Geophysical Research-Atmospheres*, *108* (D23), 2003.

Colarco, P.R., M.R. Schoeberl, B.G. Doddridge, L.T. Marufu, O. Torres, and E.J. Welton, Transport of smoke from Canadian forest fires to the surface near

Washington, D. C.: Injection height, entrainment, and optical properties, *Journal of Geophysical Research-Atmospheres*, *109* (D6), 2004.

Conny, J.M., and J.F. Slater, Black carbon and organic carbon in aerosol particles from crown fires in the Canadian boreal forest, *Journal of Geophysical Research-Atmospheres*, *107* (D11), 2002.

Dick, W.D., P. Saxena, and P.H. McMurry, Estimation of water uptake by organic compounds in submicron aerosols measured during the Southeastern Aerosol and Visibility Study, *Journal of Geophysical Research-Atmospheres*, *105* (D1), 1471-1479, 2000.

Draxler, R.R., HYSPLIT 4 User's Guide, NOAA Air Resources Laboratory, NOAA Technical Memorandum #ERL ARL-224, 2003.

Fine, P.M., G.R. Cass, and B.R.T. Simoneit, Chemical characterization of fine particle emissions from fireplace combustion of woods grown in the northeastern United States, *Environmental Science & Technology*, *35* (13), 2665-2675, 2001.

Fine, P.M., G.R. Cass, and B.R.T. Simoneit, Chemical characterization of fine particle emissions from the fireplace combustion of woods grown in the southern United States, *Environmental Science & Technology*, *36* (7), 1442-1451, 2002a.

Fine, P.M., G.R. Cass, and B.R.T. Simoneit, Organic compounds in biomass smoke from residential wood combustion: Emissions characterization at a continental scale, *Journal of Geophysical Research-Atmospheres*, *107* (D21), 2002b.

Fine, P.M., G.R. Cass, and B.R.T. Simoneit, Chemical characterization of fine particle emissions from the fireplace combustion of wood types grown in the Midwestern and Western United States, *Environmental Engineering Science*, *21* (3), 387-409, 2004.

Formenti, P., W. Elbert, W. Maenhaut, J. Haywood, S. Osborne, and M.O. Andreae, Inorganic and carbonaceous aerosols during the Southern African Regional Science Initiative (SAFARI 2000) experiment: Chemical characteristics, physical properties, and emission data for smoke from African biomass burning, *Journal of Geophysical Research-Atmospheres*, *108* (D13), 2003.

Fuchs, N., *The Mechanics of Aerosols*, 408 pp., Macmillan, New York, 1964.

Gebhart, K.A., S.M. Kreidenweis, and W.C. Malm, Back-trajectory analyses of fine particulate matter measured at Big Bend National Park in the historical database and the 1996 scoping study, *Science of the Total Environment*, *276* (1-3), 185-204, 2001.

Gelencser, A., A. Hoffer, G. Kiss, E. Tombacz, R. Kurdi, and L. Bencze, In-situ formation of light-absorbing organic matter in cloud water, *Journal of Atmospheric Chemistry*, *45* (1), 25-33, 2003.

Griffin, R.J., D.R. Cocker, R.C. Flagan, and J.H. Seinfeld, Organic aerosol formation from the oxidation of biogenic hydrocarbons, *Journal of Geophysical Research-Atmospheres, 104* (D3), 3555-3567, 1999.

Hand, J.L., A new technique for obtaining aerosol size distributions with applications to estimates of aerosol properties, Ph.D. Dissertation thesis, Colorado State University, Fort Collins, CO, 2001.

Hand, J.L., and S.M. Kreidenweis, A new method for retrieving particle refractive index and effective density from aerosol size distribution data, *Aerosol Science and Technology, 36* (10), 1012-1026, 2002.

Hand, J.L., S.M. Kreidenweis, D.E. Sherman, J.L. Collett, S.V. Hering, D.E. Day, and W.C. Malm, Aerosol size distributions and visibility estimates during the Big Bend regional aerosol and visibility observational (BRAVO) study, *Atmospheric Environment, 36* (32), 5043-5055, 2002.

Hao, W.M., and M.H. Liu, Spatial and Temporal Distribution of Tropical Biomass Burning, *Global Biogeochemical Cycles, 8* (4), 495-503, 1994.

Haywood, J.M., S.R. Osborne, P.N. Francis, A. Keil, P. Formenti, M.O. Andreae, and P.H. Kaye, The mean physical and optical properties of regional haze dominated by biomass burning aerosol measured from the C-130 aircraft during SAFARI 2000, *Journal of Geophysical Research-Atmospheres, 108* (D13), 2003.

Hinds, W.C., *Aerosol Technology: Properties, Behavior, and Measurement of Airborne Particles*, 424 pp., Wiley-Interscience, New York, 1982.

Hinzman, L.D., M. Fukuda, D.V. Sandberg, F.S. Chapin, and D. Dash, FROSTFIRE: An experimental approach to predicting the climate feedbacks from the changing boreal fire regime, *Journal of Geophysical Research-Atmospheres, 108* (D1), 2003.

Iziomon, M.G., and U. Lohmann, Optical and meteorological properties of smoke-dominated haze at the ARM Southern Great Plains Central Facility, *Geophysical Research Letters, 30* (3), 2003.

Kaufman, Y.J., P.V. Hobbs, V.W.J.H. Kirchhoff, P. Artaxo, L.J. Remer, B.N. Holben, M.D. King, D.E. Ward, E.M. Prins, K.M. Longo, L.F. Mattos, C.A. Nobre, J.D. Spinhirne, Q. Ji, A.M. Thompson, J.F. Gleason, S.A. Christopher, and S.-C. Tsay, Smoke, couds, and radiation - Brasil (SCAR-B) experiment, *Journal of Geophysical Research, 103* (D24), 31783-31808, 1998.

Knutson, E.O., and K.T. Whitby, Aerosol Classification by Electric Mobility: Apparatus, Theory and Applications, *Journal of Aerosol Science, 6*, 443-451, 1975.

Lee, T., S.M. Kreidenwels, and J.L. Collett, Aerosol ion characteristics during the Big Bend Regional Aerosol and Visibility Observational Study, *Journal of the Air & Waste Management Association, 54* (5), 585-592, 2004.

Liousse, C., J.E. Penner, C. Chuang, J.J. Walton, H. Eddleman, and H. Cachier, A global three-dimensional model study of carbonaceous aerosols, *Journal of Geophysical Research-Atmospheres, 101* (D14), 19411-19432, 1996.

Lowenthal, D.H., and N. Kumar, PM2.5 mass and light extinction reconstruction in IMPROVE, *Journal of the Air & Waste Management Association, 53* (9), 1109-1120, 2003.

Malm, W.C., and D.E. Day, Optical properties of aerosols at Grand Canyon National Park, *Atmospheric Environment, 34* (20), 3373-3391, 2000.

Malm, W.C., J.F. Sisler, D. Huffman, R.A. Eldred, and D.M. Cahill, Spatial and seasonal trends in particle concentration and optical extinction in the United States, *J. Geophys. Res., 99* (D1), 1347-1370, 1994.

Markowski, G.R., Improving Twomey's Algorithm for Inversion of Aerosol Measurement Data, *Aerosol Science Technology, 7*, 127-141, 1987.

Martins, J.V., P. Artaxo, P.V. Hobbs, C. Liousse, H. Cachier, Y. Kaufman, and A. Plana-Fattori, Particle size distributions, elemental compositions, carbon measurements, and optical properties of smoke from biomass burning in the Pacific Northwest of the United States, 1996.

Martins, V.J., P. Artaxo, C. Liousse, J.S. Reid, P.V. Hobbs, and Y.J. Kaufman, Effects of black carbon content, particle size, and mixing on light absorption by aerosols from biomass burning in Brasil, *Journal of Geophysical Research, 103* (D24), 32041-32050, 1998.

Mayol-Bracero, O.L., P. Guyon, B. Graham, G. Roberts, M.O. Andreae, S. Decesari, M.C. Facchini, S. Fuzzi, and P. Artaxo, Water-soluble organic compounds in biomass burning aerosols over Amazonia - 2. Apportionment of the chemical composition and importance of the polyacidic fraction, *Journal of Geophysical Research-Atmospheres, 107* (D20), 2002.

McDonald, R.J., B. Zielinska, E.M. Fujita, J.C. Sagebiel, J.C. Chow, and J.G. Watson, Fine particle and gaseous emission rates from residential wood combustion, *Environmental Science & Technology, 34* (11), 2080-2091, 2000.

Ogunjobi, K.O., Z. He, K.W. Kim, and Y.J. Kim, Aerosol optical depth during episodes of Asian dust storms and biomass burning at Kwangju, South Korea, *Atmospheric Environment, 38* (9), 1313-1323, 2004.

Ouimette, J.R., and R.C. Flagan, The Extinction Coefficient of Multicomponent Aerosols, *Atmospheric Environment, 16* (10), 2405-2419, 1982.

Park, R.J., D.J. Jacob, M. Chin, and R.V. Martin, Sources of carbonaceous aerosols over the United States and implications for natural visbility, *Journal of Geophysical Research, 108* (D12), doi:10.1029/2002JD003190, 2003.

Penner, J.E., H. Eddleman, and T. Novakov, Towards the Development of a Global Inventory for Black Carbon Emissions, *Atmospheric Environment Part a-General Topics, 27* (8), 1277-1295, 1993.

Radke, L.F., D.A. Hegg, P.V. Hobbs, J.D. Nance, J.H. Lyons, K.K. Laursen, R.E. Weiss, P.J. Riggan, and D.E. Ward, Particluate and Trace Gas Emissions from Large Biomass Fires in North America, in *Global Biomass Burning: Atmospheric, Climatic and Biospheric Implications*, edited by R. Prinn, pp. 219-224, MIT Press, 1991.

Reid, J.S., P.V. Hobbs, R.J. Ferek, D.R. Blake, J.V. Martins, M.R. Dunlap, and C. Liousse, Physical, chemical, and optical properties of regional hazes dominated by smoke in Brazil, *Journal of Geophysical Research-Atmospheres, 103* (D24), 32059-32080, 1998.

Roberts, G.C., A. Nenes, J.H. Seinfeld, and M.O. Andreae, Impact of biomass burning on cloud properties in the Amazon Basin, *Journal of Geophysical Research-Atmospheres, 108* (D2), 2003.

Rogge, W.F., L.M. Hildemann, M.A. Mazurek, G.R. Cass, and B.R.T. Simoneit, Sources of fine organic aerosol. 9. Pine, oak and synthetic log combustion in residential fireplaces, *Environmental Science & Technology, 32* (1), 13-22, 1998.

Rogge, W.F., M.A. Mazurek, L.M. Hildemann, G.R. Cass, and B.R.T. Simoneit, Quantification of urban organic aerosols at a molecular level: Identification, abundance, and seasonal variation, *Atmos. Environ., 27A* (8), 1308-1330, 1993.

Seinfeld, J.H., and S.N. Pandis, *Atmospheric Chemsitry and Physics: From Air Pollution to Climate Change*, John Wiley, New York, 1998.

Simoneit, B.R.T., J.J. Schauer, C.G. Nolte, D.R. Oros, V.O. Elias, M.P. Fraser, W.F. Rogge, and G.R. Cass, Levoglucosan, a tracer for cellulose in biomass burning and atmospheric particles, *Atmospheric Environment, 33,* 173-182, 1999.

Stelson, A.W., Urban Aerosol Refractive-Index Prediction by Partial Molar Refraction Approach, *Environmental Science & Technology, 24* (11), 1676-1679, 1990.

Tang, I.N., Chemical and size effects of hygroscopic aerosols on light scattering coefficients, *Journal of Geophysical Research-Atmospheres, 101* (D14), 19245-19250, 1996.

Tegen, I., A. Lacis, and I. Fung, The Influences of Mineral Aerosols from Disturbed Soils on Climate Forcing, *Nature, 380,* 419-422, 1996.

Turpin, B.J., and H.J. Lim, Species contributions to PM2.5 mass concentrations: Revisiting common assumptions for estimating organic mass, *Aerosol Science and Technology*, *35* (1), 602-610, 2001.

Twomey, S., Comparison of Constrained Linear Inversion and an Iterative Nonlinear Algorithm Applied to the Indirect Estimation of Particle Size Distributions, *JOurnal of Comput. Phys.*, *18*, 188-200, 1975.

Wandinger, U., D. Muller, C. Bockmann, D. Althausen, V. Matthias, J. Bosenberg, V. Weiss, M. Fiebig, M. Wendisch, A. Stohl, and A. Ansmann, Optical and microphysical characterization of biomass-burning and industrial-pollution aerosols from multiwavelength lidar and aircraft measurements, *Journal of Geophysical Research-Atmospheres*, *107* (D21), 2002.

Ward, D.E., W.M. Hao, R.A. Susott, R.E. Babbitt, R.W. Shea, J.B. Kauffman, and C.O. Justice, Effect of fuel composition on combustion efficiency and emission factors for African savanna ecosystems, *Journal of Geophysical Research-Atmospheres*, *101* (D19), 23569-23576, 1996.

Watson, J.G., Visibility: Science and regulation, *Journal of the Air & Waste Management Association*, *52* (6), 628-713, 2002.

White, W.H., E.S. Macias, J.D. Kahl, P.J. Samson, J.V. Molenar, and W.C. Malm, On the Potential of Regional-Scale Emissions Zoning as an Air-Quality Management Tool for the Grand-Canyon, *Atmospheric Environment*, *28* (5), 1035-1045, 1994.

Whiteman, C., *Mountain Meteorology: Fundamentals and Applications*, Oxford University Press, New York, 2000.

Wiedensohler, A., An Approximation of the Bipolar Charge-Distribution for Particles in the Sub-Micron Size Range, *Journal of Aerosol Science*, *19* (3), 387-389, 1988.

Winklmayr, W., H.-C. Wang, and W. John, Adaptation of the Twomey algorithm to the inversion of cascade impactor data, *Aerosol Sci. & Technol.*, *13*, 322-331, 1990.

Wotawa, G., and M. Trainer, The influence of Canadian forest fires on pollutant concentrations in the United States, *Science*, *288* (5464), 324-328, 2000.

Yamasoe, M.A., Y.J. Kaufman, O. Dubovik, L.A. Remer, B.N. Holben, and P. Artaxo, Retrieval of the real part of the refractive index of smoke particles from Sun/sky measurements during SCAR-B, *Journal of Geophysical Research-Atmospheres*, *103* (D24), 31893-31902, 1998.

Zhang, X.Q., B.J. Turpin, P.H. McMurry, S.V. Hering, and M.R. Stolzenburg, Mie Theory Evaluation of Species Contributions to 1990 Wintertime Visibility Reduction in the Grand-Canyon, *Journal of the Air & Waste Management Association*, *44* (2), 153-162, 1994.

APPENDIX A. THEORETICAL LOSS CALCULATIONS

Loss calculations were performed for the instruments to account for particle losses in the sampling lines and were based on those performed by *Hand* [2001] for a similar sampling setup. Losses due to diffusion, gravity, bends, and Perma Pure dryers were included. All calculations were performed for instrument channel midpoint diameters, which were converted to an aerodynamic diameter assuming a density of 1.5 g cm^{-3}. Optical particle counter diameters were converted from optical to geometric diameter assuming a refractive index of m = 1.58 before being converted to aerodynamic diameters (ρ = 1.5 g cm^{-3}).

A number of parameters used in the loss calculations did not depend on tubing configuration and are described here. Air density, ρ_{air} (kg m^{-3}) was calculated for the Yosemite National Park site elevation using Equation A.1:

$$\rho_{air} = \frac{P}{1013.25} \frac{MW_{air}}{0.08206 \cdot T} \tag{A.1}$$

where P was the ambient pressure (833 hPa), T was the temperature at which measurements were performed (298 K) and MW_{air} was the molecular weight of air (29 g mol^{-1}). The momentum transfer occurring during molecular collisions is given by the dynamic viscosity (kg m s^{-1}) [*Allen and Raabe*, 1985]

$$\eta = \frac{\eta_{23}}{10} \frac{T_r + S}{T + S} \left(\frac{T}{T_r} \right)^{\frac{3}{2}} \tag{A.2}$$

109

The Sutherland interpolation constant is given by S (110.4) and e_{23} and T_r are reference

viscosity (1.83245×10^{-4}) and temperature (296.15 K). The mean free path, λ, a measure

of the mean distance a molecule travels before colliding with another molecule, was

given by [Allen and Raabe, 1985]

$$\lambda = \lambda_0 \frac{T}{T_r} \frac{760}{P_{mmHg}} \frac{1 + \dfrac{S}{T_r}}{1 + \dfrac{S}{T}}$$

(A.3)

where λ_0 was the reference mean free path (0.0673 μm) and P_{mmHg} is the pressure in units

of mmHg. The mean free path was in units of meters.

Stokes law describes the behavior of particles in a fluid stream and is a very

important parameter in loss correction calculations. It is a solution to the Navier-Stokes

equations assuming inertial forces are negligible compared to viscous forces. It is also

assumed that the fluid is incompressible, there are no walls or other particles nearby,

motion is constant, the particle is a rigid sphere and the fluid velocity at the particle's

surface is zero. The last assumption breaks down for very small particles because of 'slip'

at the surface of the particle as the diameter approaches the mean free path of the gas. As

a result Stokes law must be corrected using the Cunningham correction factor (C_c) for

particles less than 1 μm in diameter [Hinds, 1982]. The dimensionless Cunningham

correction factor is given by

$$C_c = 1 + \frac{2}{P_{cmHg} D_p} \left[6.32 + 2.01 \cdot \exp\left(-0.1095 \cdot P_{cmHg} D_p \right) \right]$$

(A.4)

where P_{cmHg} is the pressure in cmHg and D_p is particle diameter in μm.

110

Particle diffusion, characterized by the diffusion coeffienct, D (m^2 s^{-1}), describes the movement of particles from areas of higher concentration to areas of lower concentration and is similar to molecular diffusion [Hinds, 1982]:

$$D = \frac{kTC_c}{3\pi\eta D_p}$$
(A.5)

The Boltzman constant is given as k (1.38×10^{-23} J K^{-1}), diameter has units of meters and viscosity, η, was calculated in Equation A.2. The Schmidt number, Sc, is a dimensionless parameter used to describe the relationship between convective mass transfer and the diffusion of particles [Baron and Willeke, 2001]. It is given as the ratio of the kinematic viscosity to the diffusion coefficient:

$$Sc = \frac{\eta}{\rho D}$$
(A.6)

The settling velocity of a particle is described by Equation A.7 in units of m s^{-1} where diameter is in units of meters, g is the gravitational constant (9.81 m s^{-2}) and ρ_p is the particle density (g cm^{-3}).

$$v_{set} = \frac{\rho_p D_p^2 g C_c}{18\eta}$$
(A.7)

The remaining parameters depended on the setup of the sampling lines and were computed for the specific tubing configuration for each instrument. Losses in the sampling lines due to diffusion of the particle to the tube walls were determined using Equation A.8 [Baron and Willeke, 2001]

$$\eta_{diff} = \exp(-\xi Sh)$$
(A.8)

where

$$\xi = \frac{\pi D L}{Q} \tag{A.9}$$

L is the length of the tubing segment in meters and Q is the sample flow rate in m^3 s^{-1}.

The Sherwood number (Sh) is a dimensionless mass transfer coefficient given by

$$Sh = 3.66 + \frac{0.0668 \frac{d_i}{L} Re \cdot Sc}{1 + 0.04 \left(\frac{d_i}{L} Re \cdot Sc \right)^{\frac{2}{3}}} \tag{A.10}$$

where d_i is the tubing inner diameter in meters and Re is the Reynolds number, which is the ratio of inertial forces to frictional forces of a gas [Baron and Willeke, 2001]:

$$Re = \frac{\rho_{air} v_{tube} d_i}{\eta} \tag{A.11}$$

where v_{tube} is the velocity in the tube (m s^{-1}).

Losses due to gravitational settling in the sampling lines was calculated using Equation A.12 [Baron and Willeke, 2001]

$$\eta_{grav} = 1 - \frac{2}{\pi} \left[2\kappa \sqrt{1 - \kappa^{\frac{2}{3}}} - \kappa^{\frac{1}{3}} \sqrt{1 - \kappa^{\frac{2}{3}}} + \arcsin\left(\kappa^{\frac{1}{3}} \right) \right] \tag{A.12}$$

where

$$\kappa = \frac{3}{4} \frac{v_{set} L}{d_i v_{tube}} \cos(\theta) \tag{A.13}$$

and θ (radians) is the angle of inclination with respect to horizontal. Losses in tubing bends were computed using Equation A.14 [Baron and Willeke, 2001]

$$\eta_{tube} = (1 - Stk \cdot \varphi)^n \tag{A.14}$$

where φ is the angle of the bend in radians, n is the number of bends and Stk is the dimensionless Stokes number, given by Equation A.15:

$$Stk = \frac{\rho_p D_p^2 C_c v_{tube}}{18\eta d_i}$$ (A.15)

with the diameter given in meters. Each component drawing off the five-way flow splitter was treated as a separate inlet with aspiration and transport losses. For subisokinetic inlet sampling, aspiration losses were calculated using Equation A.16 [*Baron and Willeke*, 2001]

$$\eta_{splitter,asp} = 1 + \left(\frac{U_0}{U} - 1\right)\left(1 - \frac{1}{1 + 3.77 Stk^{0.883}}\right)$$ (A.16)

where U_0 was the velocity in the main body of the splitter and U was the velocity within the tube branching off of the splitter main body. Transport losses in the inlet were computed using A.17 [*Baron and Willeke*, 2001]

$$\eta_{splitter,trans} = \frac{1 + \left(\frac{U_0}{U} - 1\right) \Big/ \left(1 + \frac{2.66}{Stk^{\frac{2}{3}}}\right)}{1 + \left(\frac{U_0}{U} + 1\right) \Big/ \left(1 + \frac{0.418}{Stk}\right)}$$ (A.17)

Equations A.18 and A.19 were used to determine aspiration and transport losses for superisokinetic sampling:

$$\eta_{splitter,asp} = 1 + \frac{\frac{U_0}{U} - 1}{1 + \frac{0.506\sqrt{\frac{U_0}{U}}}{Stk}}$$ (A.18)

$$\eta_{splitter,trans} = \exp\left(-75 I_v^2\right)$$ (A.19)

where

$$I_v = 0.09\left(Stk\frac{U - U_0}{U_0}\right)^{0.3}$$ (A.20)

Losses in the Perma Pure drying system were estimated from the results of tests conducted to determine Perma Pure losses during BRAVO:

$$\eta_{PP} = -0.1261 \cdot \log^2(D_p) + 0.6276 \cdot \log(D_p) + 0.1579 \qquad (A.20)$$

Losses in the DMA due to diffusion were calculated using Equation A.21:

$$\eta_{DMA} = 0.82\exp(-11.5\beta) + 0.10\exp(-70.0\beta) + 0.03\exp(-180.0\beta) + 0.02\exp(-340.0\beta)$$

$$(A.21)$$

with

$$\beta = \frac{600 L_{eff} D}{Q_{DMA}} \qquad (A.22)$$

where L_{eff} is the effective length (13 m), Q_{DMA} is the polydisperse flow rate (0.3 LPM). Losses in the condensation particle counter (CPC) were calculated using values given in *Hand* [2001] from the Seattle Workshop, August 1995 using

$$\eta_{CPC} = 1 - \frac{1.15}{1 + \exp\left(\dfrac{D_p - 11.3}{2.1}\right)} \qquad (A.23)$$

with diameter given in nanometers.

Results of loss calculations for the ambient LASAIR 1003 optical particle counter are shown in Figure A.1. The losses from each component of the total losses for various sampling components are also given. There are only small losses for smaller diameter particles in the OPC due to diffusional losses in the sampling lines. There were no sudden bends in the OPC sampling line and gravitational losses were minimized by avoiding horizontal tube positioning and keeping the total sampling length short. Loss calculations for the dried DMA are given in Figure A.2. Losses for the DMA sampling system were higher due to loss of particles in the Perma Pure drying system and losses within the

DMA/CPC system. All losses prior to the five-way flow splitter are identical for both instruments as they shared the same sampling line.

LASAIR 1003 Losses
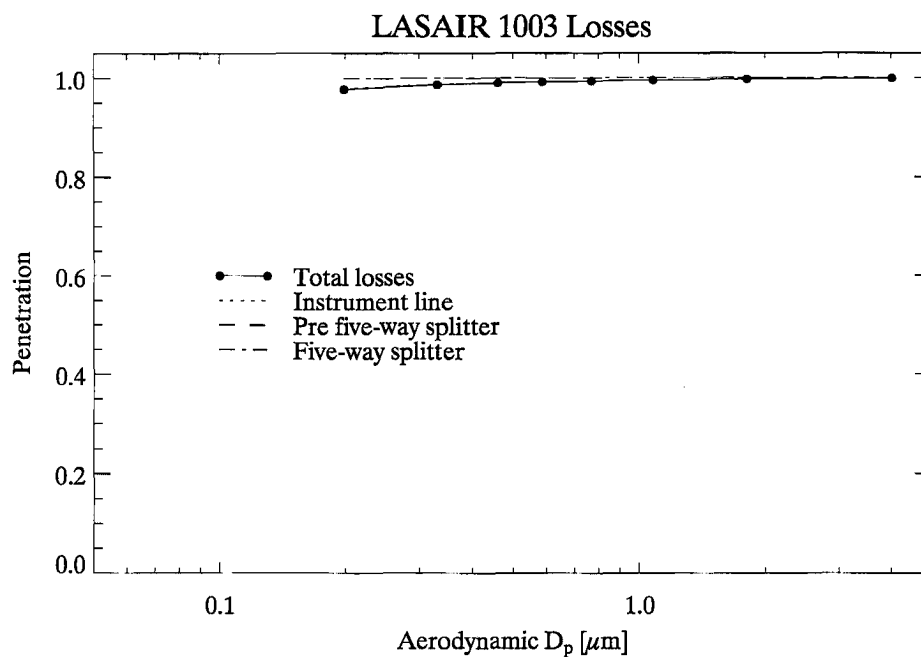
Figure A.1 Particle penetration efficiencies for the ambient OPC (LASAIR 1003) as a function of aerodynamic diameter. Contributions from each major component of the sampling system are also shown.

DMA Losses
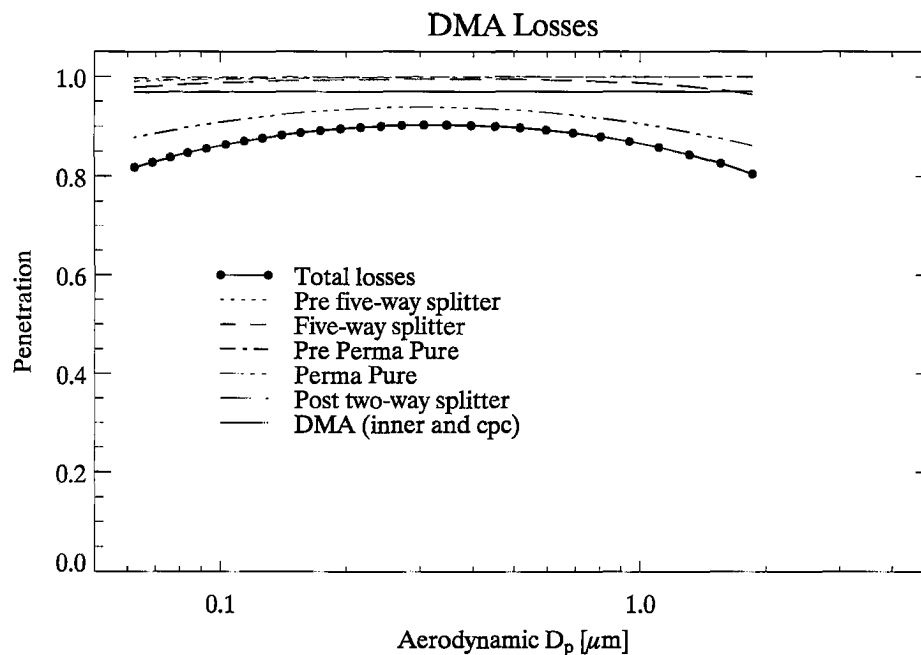
Figure A.2 Particle penetration efficiencies for the dried DMA as a function of aerodynamic diameter. Contributions from each major component of the sampling system are also shown.

APPENDIX B. UNCERTAINTY CALCULATIONS

Experimental uncertainty calculations were performed for aerosol size parameters

and light scattering coefficients using the method of error propagation described by

Bevington and Robinson [1992] [*Hand*, 2001]. Number concentration, N, is calculated by

Equation B.1:

$$N = \frac{c}{Qt} \qquad (B.1)$$

where c is the raw counts measured by the instrument in time t and Q is the instrument

flow rate. Assuming negligible uncertainty in sample time, the uncertainty in N is given

by Equation B.2.

$$\delta N = \sqrt{\left(\frac{\partial N}{\partial c}\right)^2 + \left(\frac{\partial N}{\partial Q}\right)^2 + \left(\frac{\partial N}{\partial L}\right)^2 + \left(\frac{\partial N}{\partial N_{avg}}\right)^2} \qquad (B.2)$$

The first term in Equation B.2 is the uncertainty in N due to uncertainty in the counts

determined by Poisson statistics:

$$\frac{\partial N}{\partial c} = \frac{\delta c}{Qt} \qquad (B.3)$$

where $\delta c = \sqrt{c}$. The second term is the uncertainty in N caused by uncertainty in Q,

given by Equation B.4

$$\frac{\partial N}{\partial Q} = \frac{-c}{Q^2 t} \delta Q \qquad (B.4)$$

with δQ representing the standard deviation in the flow measurements. The third and

fourth terms in B.2 represent uncertainty in N due to uncertainty in the loss corrections

and from averaging the distributions together respectively, both of which are negligible compared to the first two terms and will be dropped from further calculations. Substituting and rewriting gives Equation B.5 for uncertainty in N in instrument channel i:

$$\delta N_i = \sqrt{\frac{N_i}{Qt_i} + \frac{N_i^2}{Q^2}(\delta Q)^2} \qquad (B.5)$$

Uncertainty in volume concentration can also be calculated in a similar manner. The volume concentration in a given bin, V_i, with midpoint diameter $D_{p,i}$ is given by Equation B.6

$$V_i = \frac{\pi}{6} D_p^3 N_i \qquad (B.6)$$

and its uncertainty by Equation B.7

$$\delta V = \sqrt{\left(\frac{\partial V_i}{\partial D_{p,i}}\right)^2 + \left(\frac{\partial V_i}{\partial N_i}\right)^2} \qquad (B.7)$$

The first term is the uncertainty in V due to uncertainty in diameter:

$$\frac{\partial V_i}{\partial D_{p,i}} = \frac{\pi}{2} D_{p,i}^2 N_i \delta D_{p,i} \qquad (B.8)$$

The second term is the uncertainty in V due to uncertainty in number (Equation B.5):

$$\frac{\partial V_i}{\partial N_i} = \frac{\pi}{6} D_{p,i}^3 \delta N_i \qquad (B.9)$$

Substituting in Equation B.8 and B.9 gives the uncertainty in volume concentration as:

$$\delta V_i = \sqrt{\left(\frac{\pi}{6} D_{p,i}^2 N_i\right)^2 (\delta D_{p,i})^2 + \left(\frac{\pi}{6} D_{p,i}^3\right)^2 (\delta N_i)^2} \qquad (B.10)$$

The uncertainty in diameter will depend on the technique used to make the measurement. The uncertainty in diameter measured by the DMA will depend on the uncertainties in the voltage applied to the collector rod (V_{DMA}) and the shape factor (χ) of the particles sampled. *Hand* [2001] showed that for the DMA configuration used in BRAVO and YACS the uncertainty in voltage had a negligible effect on the uncertainty of the diameter. The uncertainty in the diameter measured by the OPC depends on refractive index. As there is no theoretical relationship between instrument response and diameter for the instrument used during BRAVO and YACS, empirically derived equations are used instead. A second order polynomial determined by instrument calibrations is used to relate geometric and optical diameters in Equation B.11.

$$D_{p,i} = \frac{D_{opt,i}}{a_i m^2 + b_i m + c_i}$$

(B.11)

The polynomial coefficients *a, b,* and *c*, taken from *Hand* [2001], are different for each bin and are given in Table B.1. The optical diameter is determined by the manufacturer calibration. Taking the derivative of Equation B.11 allows for the quantification of the effects of refractive index on each bin. The derivative of B.11 will increase for higher refractive indices due to the shape of the polynomials [*Hand*, 2001]. An uncertainty in refractive index of δm = 0.005 results in a 0.003 μm uncertainty in diameter [*Hand*, 2001]. Higher refractive indices result in smaller geometric diameters.

Uncertainties in volume mean diameters were computed using Equation B.12.

$$D_{gv} = \exp\left(\frac{\sum V_i \ln D_{pm,i}}{\sum V_i}\right)$$

(B.12)

which *Hand* [2001] rewrites as Equation B.13

$$D_{gv} = \exp(C_i)$$

(B.13)

where

$$C_i = \frac{\sum A_i}{\sum B_i}$$ (B.14)

and

$$A_i = V_i \ln D_{pm,i}$$

$$B_i = V_i$$

The uncertainties in the quantities A and B are

$$\partial A_i = \sqrt{\left(\ln D_{pm,i}\right)^2 (\delta V_i)^2 + \left(\frac{V_i}{D_{pm,i}}\right)^2 (\delta D_{pm,i})^2}$$ (B.15)

$$\partial B_i = \partial V_i$$ (B.16)

and uncertainty in volume concentrations and diameter were discussed earlier. The uncertainty in C was determined using Equation B.17

$$\partial C_i = \sqrt{\left(\frac{1}{B_i}\right)^2 (\delta A_i)^2 + \left(\frac{-A_i}{B_i}\right)^2 (\delta B_i)^2}$$ (B.17)

The uncertainty in the volume mean diameter is then given by Equation B.18

$$\partial D_{gv} = \exp(C)\partial C$$ (B.18)

Uncertainties for light scattering coefficients were calculated using Equation B.19 assuming uncertainties in the Mie scattering efficiency were negligible:

$$\partial b_{sp} = \sqrt{\left(\frac{3Q_{sp}}{2D_p}\right)^2 (\delta V)^2 + \left(\frac{-3Q_{sp}V}{2D_p^2}\right)^2 (\delta D_p)^2}$$ (B.19)

120

Table B.1 PMS LASAIR 1003 channel scaling polynomial coefficients for the scaling factor equation $f_D = am^2 + bm + c$ (from *Hand* [2001]).

Channel	a	b	c
1	19.637	-57.25	42.393
2	9.7348	-28.37	21.502
3	7.1322	-20.437	15.468
4	-2.1338	7.6673	-5.7949
5	2.8073	-7.0444	5.1074
6	9.6226	-27.662	20.661
7	1.5827	-4.1139	3.5417

APPENDIX C. CHEMICAL MEASUREMENTS

Aerosol composition measurements were conducted during the study to determine chemical species contributing to aerosol mass at the park. These data were used to calculate a number of parameters, including mass, index of refraction and density. Findings related to chemical composition will soon be published [*Lee et al.*, in progress; *Malm et al..*, in progress]. Results used for calculations in this work are listed here. As a number of species were measured using more than one technique, only data used in the calculations made for this work are presented. Data in Table C.1 are given directly as the 24-hour filter measurement or, in the case of data measured at higher time resolution, as averages of data points during that 24-hour filter sampling period.

Table C.1 PM$_{2.5}$ mass concentrations (μg m^{-3}) during YACS. IMPROVE data are used for organic carbon (OC) and soil concentrations. URG data are used for ionic concentrations. Elemental or black carbon (BC) concentrations are 24-hour averages of aethalometer data for each day.

Day of Year	BC	OC	Na$^+$	NH$_4^+$	K$^+$	Mg^{2+}	Ca^{2+}	Cl$^-$	NO$_3^-$	SO$_4^{2-}$	Soil
200	0.22	1.27	0.09	0.53	0.03	0.01	0.02	0.00	0.29	1.29	0.47
201	0.27	1.67	0.10	0.58	0.04	0.01	0.03	0.00	0.33	1.56	0.66
202	0.19	1.35	0.07	0.49	0.05	0.01	0.02	0.00	0.25	1.16	0.53
203	0.13	1.13	0.08	0.43	0.02	0.01	0.02	0.00	0.29	1.16	0.70
204	0.20	2.28	0.06	0.40	0.03	0.01	0.02	0.00	0.25	0.99	0.38
205	0.24	2.46	0.08	0.48	0.03	0.01	0.02	0.00	0.26	1.27	0.41
206	0.19	1.89	0.06	0.36	0.02	0.01	0.01	0.00	0.15	0.95	0.63
207	0.19	1.73	0.04	0.46	0.02	0.01	0.01	0.00	0.16	1.24	0.59
208	0.36	3.68	0.05	0.52	0.05	0.01	0.05	0.00	0.29	1.30	0.76
209	0.36	4.10	0.09	0.65	0.06	0.01	0.03	0.00	0.33	1.67	0.59
210	0.32	3.77	0.14	0.62	0.06	0.02	0.03	0.00	0.35	1.64	0.87
211	0.38	4.14	0.17	0.65	0.06	0.02	0.03	0.00	0.38	1.73	0.58
212	0.33	4.12	0.09	0.60	0.06	0.02	0.03	0.00	0.31	1.58	0.54
213	0.28	3.28	0.06	0.55	0.05	0.01	0.02	0.00	0.18	1.45	0.85
214	0.22	1.75	0.03	0.46	0.03	0.00	0.02	0.00	0.18	1.23	0.44
215	0.33	3.30	0.02	0.53	0.06	0.01	0.03	0.00	0.74	1.30	0.57
216	0.20	2.80	0.07	0.31	0.05	0.01	0.02	0.02	0.30	0.71	0.29
217	0.26	4.05	0.12	0.37	0.08	0.01	0.03	0.01	0.51	0.89	0.59
218	0.19	2.57	0.14	0.33	0.04	0.01	0.02	0.02	0.47	0.78	0.32
219	0.15	1.75	0.14	0.26	0.03	0.01	0.02	0.03	0.44	0.62	0.36
220	0.24	3.46	0.09	0.27	0.05	0.01	0.04	0.03	0.29	0.61	0.72
221	0.31	5.10	0.05	0.33	0.07	0.01	0.04	0.01	0.28	0.76	0.55
222	0.31	4.83	0.05	0.35	0.06	0.01	0.04	0.01	0.24	0.78	0.62
223	0.39	4.59	0.05	0.38	0.06	0.01	0.04	0.00	0.23	0.92	0.55
224	0.39	5.68	0.06	0.41	0.08	0.03	0.05	0.02	0.20	1.01	0.92
225	0.44	6.70	0.06	0.52	0.08	0.02	0.06	0.02	0.30	1.22	0.66
226	0.51	8.54	0.06	0.52	0.10	0.01	0.05	0.01	0.24	1.24	0.49
227	0.55	8.99	0.04	0.54	0.10	0.01	0.04	0.01	0.21	1.22	0.83
228	0.63	10.10	0.06	0.55	0.12	0.01	0.05	0.01	0.26	1.26	0.52
229	0.68	11.34	0.06	0.49	0.13	0.01	0.05	0.02	0.32	0.97	0.45
230	0.39	6.21	0.10	0.48	0.07	0.01	0.03	0.00	0.38	1.16	0.52
231	0.45	9.19	0.17	0.47	0.09	0.02	0.04	0.01	0.64	0.96	0.80
232	0.41	8.19	0.17	0.44	0.08	0.02	0.04	0.01	0.73	0.83	0.36
233	0.29	4.59	0.16	0.35	0.05	0.02	0.03	0.00	0.70	0.85	0.46
234	0.27	3.46	0.17	0.45	0.05	0.02	0.03	0.00	0.88	1.11	0.80
235	0.25	3.54	0.14	0.44	0.05	0.01	0.02	0.00	0.70	1.25	0.49
236	0.21	2.85	0.09	0.44	0.04	0.01	0.02	0.00	0.36	1.14	0.42
237	0.22	4.00	0.06	0.37	0.04	0.01	0.01	0.00	0.26	0.90	0.34
238	0.32	6.09	0.06	0.31	0.05	0.01	0.03	0.01	0.27	0.73	0.82
239	0.25	4.35	0.04	0.29	0.04	0.01	0.02	0.00	0.31	0.67	0.56
240	0.31	4.12	0.06	0.37	0.04	0.01	0.04	0.00	0.41	0.85	0.79
241	0.30	3.38	0.14	0.51	0.04	0.02	0.03	0.00	0.57	1.31	0.92
242	0.22	2.20	0.10	0.46	0.03	0.01	0.03	0.00	0.33	1.24	0.53
243	0.22	1.76	0.07	0.45	0.03	0.01	0.03	0.00	0.37	1.11	0.63
244	0.21	2.40	0.04	0.50	0.03	0.01	0.02	0.00	0.18	1.31	0.68
245	0.17	2.41	0.03	0.48	0.02	0.00	0.02	0.00	0.14	1.25	0.94
246	0.12	0.65	0.03	0.58	0.02	0.00	0.02	0.00	0.12	1.63	0.55
247	0.15	0.60	0.04	0.47	0.02	0.00	0.02	0.00	0.28	1.33	0.59